Application of Cross Polarisation Techniques to Dynamic Nuclear Polarisation Dissolution Experiments

by

Angel Joaquin Pérez Linde

Thesis submitted to the University of Nottingham for the degree of Doctor of Philosophy, November 2009.

Sir Peter Mansfield Magnetic Resonance Centre

The University of Nottingham

November 2009

Abstract

Dynamic Nuclear Polarisation (DNP) was suggested for the first time by Albert Overhauser in early 1950s. In DNP experiments the polarisation from electrons can be transferred to nuclei by irradiation of the electron resonance line. There are several possible mechanisms for polarisation transfer that involve DNP in solid state depending on the width of the electron line $\delta\omega_S$ in respect to the nuclear Larmor frequency ω_I.

In this thesis, the efficiency of TEMPO radical (2,2,6,6 tetramethilpiperidine, 1 oxyl) for DNP is demonstrated in combination with nuclear polarisation transfer techniques for dissolution experiments. New cryo-probes were developed for DNP and cross polarisation (CP) for operation temperatures as low as 1.5 K. Two of them were designed for dissolution experiments. Some published sequences of nuclear polarisation transfer were tested at low temperatures and compared. Novel sequences were implemented for efficient CP in organic samples doped with TEMPO to allow for a consecutive dissolution experiment. The combination of DNP with new CP sequences at low temperatures, achieved at least twice the ^{13}C polarisation obtained with DNP and in a substantially shorter time (between 5 to 10 minutes) in samples doped with TEMPO. The polarisation levels obtained in samples of [^{13}C-1] labelled Na acetate in a few minutes was comparable to the polarisation obtained with trityl radicals in a few hours.

In addition, another strategy was investigated by using brute force polarisation as a mechanism for achieving large levels of nuclear spin order. The problem presented by this method is the long relaxation time required to ob-

tain the thermal equilibrium polarisation.

By doping with lanthanides samples of [^{13}C-1] labelled Na acetate in 1:1 glycerol-water, it was possible to obtain thermal equilibrium for a ^{13}C spin system in less than one hour.

Contents

List of Tables

List of Figures

Scope of this thesis

This thesis has been divided into 7 chapters. In this thesis I intend to describe the process that leads to an improved DNP experiment for dissolution experiments. I also describe some findings in the application of brute force polarisation for dissolution experiments.

In the Introduction chapter some concepts about nuclear relaxation in solid state NMR and DNP are explained very briefly. Although not strictly correct at low spin temperatures, the theoretical explanation of these concepts are based on the explanation by D. Wolf, A. Abragam and M. Goldman. Some very brief remarks about the available hardware are added at the end of this chapter. The second chapter describes the hardware used for all DNP, CP and dissolution experiments, since the NMR probes had to be home-made. In the first section of this chapter some principles of hardware in NMR are explained. In the second section different probes are described and compared. The third chapter explores the possibility of using brute force polarisation with samples doped with lanthanide ions as a way to achieve large nuclear polarisations at low temperature (1.5 K) for dissolution experiments, instead of DNP. The fourth chapter shows some DNP experiments carried out at low temperature, for samples doped with trityl and samples doped with TEMPO, mainly for ^{13}C and ^{1}H polarisation enhancement. In the fifth chapter several techniques of nuclear polarisation transfer are used at temperatures close to 1.5 K. Two main type of techniques have been implemented. The first type corresponds to $\hat{I}_z \longrightarrow \hat{S}_{x-y}$ standard CP and Non-Zeeman CP sequences. The second type corresponds to $\hat{I}_z \longrightarrow \hat{S}_z$ sequences, like the published COMPOZER-

CP or the home-made DOIN-CP, the improved DOIN-CP or the variation of the COMPOZER-CP. In the chapter for dissolution it is demonstrated with experiments that the brute force polarisation can be used for dissolution experiments. Data for the application of DOIN-CP with DNP for dissolution experiments is presented and discussed here. In the last chapter an overall conclusion is presented.

Abbreviations

COMPOZER-CP	COMPOsite zero cross polarisation
CP	Cross Polarisation
DTPA	Diethylene triamine pentaacetic acid
DOIN-CP	DOuble Inversion Cross Polarisation
DNP	Dynamic Nuclear Polarisation
DQ	Double Quantum (transitions)
DMSO	DiMethyl SulfOxide
EPR	Electron Paramagnetic Resonance
FID	Free Induction Decay
HH	Hartmann Hahn
LODESR	Longitudinally Detected Electron Spin Resonance
NMR	Nuclear Magnetic Resonance
NZCP	Non Zeeman Cross Polarisation
OI	Oxford Instruments
PEDRI	Proton Electron Double Resonance Imaging
PEEK	polyetheretherketone, thermoplastic resin
PTFE	polytetrafluoroethylene
RF	Radiofrequency
SAP	Stand Alone Polariser
SE	Solid Effect
SNR	Signal-to-Noise Ratio
TEMPO	2,2,6,6-Tetramethylpiperidine-1-oxyl
TL	Transmission Line
WURST	Wideband Uniform Rate and Smooth Truncation
ZQ	Zero Quantum (transitions)

Acknowledgments

Thank God, the PhD is over! This project has been very complex in the sense that it involved a lot of hands-on work and also a lot of Physics. I was required to have experience in many techniques and this set a difficult test for me, in the years the project took place. The good thing is that I was not alone at any moment.
In the very first place I have to thank my family, who were there always for me. Thanks to my parents Manuel and Angela. This thesis is for them. I want to thank my two brothers Manuel and Rafael, and my sisters Carmen and Amalia. They always root for me.

I also need to thank my dear flatmates Pooja Jain, Kuldip Modha and Jens Ripcke. They were always nice, patient and helpful.

Then I have to think of the department. I thank Dr. Walter Köckenberger for his supervision, suggestions and efforts in this project. This project was very ambitious and the equipment was available for us most of the time. My DNP team was always helpful. Thanks, especially to Jim Leggett for all the work done. Also to Josef Granwehr, Christian, Anniek, Rafal and Waldek. Peter joined later, but just in time to correct a chapter of this thesis. Between the people in the workshop, I need to thank those I bothered especially: Ian Thexton, Jeff Smith and Alan Dorkes. From the electronic workshop I need to thank Paul Clark, who was always so attentive. In the School of Physics and Astronomy Building, I also bothered Bob Chettle and some more people from

the workshops to obtain good advice in relation to electronics, coil formers and more. From the academic staff I need to thank Professors Peter Morris, David Gadian (working with you was a helpful and great experience), Anthony Horsewill and Dr Paul Glover who gave me great advice, guidance and encouragement. And to Jorge Garibay who showed me some good tricks about cryoprobes and pulse programming. Also I want to mention my workmates Kuldeep Panesar, Mike Poole, Peter Wright, Arthur Magill, Aaron, Julia, Brett Haywood, Tom, Cesar, Rosa (thank you very much for all the computer advice, Cesar and Rosa), Elisa and Antonio, Samia and Lesley Martin since in one or other way, they contributed somehow to this project, although some of them may think they did not. My living here in Nottingham has been much easier thanks to the generosity of workmates like Olivier, Jo, Yana, Fang, Amani, and Andreas. I have many memories from the MR Centre, but one of them was that day I played music with my workmates Claire and Matt for another extra project. At many points during my time here, Andrew Peters and Mike Barlow solved some computer issues that arose. From Oxford Instruments molecular Biotools Ltd. I need to thank all the advice and encouragement they provided. Especially to Rob Slade and Gary Stables, and all the people involved in the dual centre magnet construction. I also want to thank the people from the high field ESR group at the University of St Andrews, especially Rob Hunter, who gave me very, very useful advice for this project, especially regarding the Inventor.

I also want to thank Paul Walker, Laura, Cressida and the rest of the people of my Thursday evening group, for their encouragement and sense of humour.

This work could not have been possible without the EPSRC grant. Thank you very much. I also thank professor David Gadian for the extension I received at the very end which made possible for me to work more in the last (but necessary) results.

AJ

Chapter 1

Introduction

In this chapter a general overview of nuclear magnetic resonance, nuclear relaxation and dynamic nuclear polarisation is presented. The phenomenological Bloch equations are first introduced, followed by the description of the main interactions between nuclei. The inclusion of the spin temperature theory permits the different terms in the Hamiltonian to be considered as separate thermal reservoirs or baths, in the high temperature approximation. Different concepts regarding relaxation in electrons and nuclei at low temperature (1.5 K) are explained before introducing dynamic nuclear polarisation. In this section two polarisation transfer mechanisms are mainly treated: the solid effect and thermal mixing. Each of these fields is very extensive and references are included for further information. Finally some general aspects of the instruments and the experimental are discussed.

1.1 The nuclear spin, the Bloch equations and signal processing

1.1.1 The nuclear spin

Spin angular momentum is an intrinsic property of elementary particles. The nuclear spin $\hat{I}$ in a nucleus results from the contribution of the nucleons spin

angular momentum. The spin $\hat{I}$ is associated with a nuclear magnetic moment $\hat{\mu}$:

$$\hat{\mu} = \gamma \hbar \hat{I} \tag{1.1}$$

where $\hbar$ is the Planck's constant divided by 2π and γ is the gyromagnetic ratio associated with the particular nuclear spin. In the presence of an external magnetic field $\vec{B}_0 = B_0 \vec{z}$ the magnetic moment precesses around an axis called the polarisation axis at the Larmor frequency [21]:

$$\omega_0 = \gamma B_0 \tag{1.2}$$

with units of rad/s. If the magnetic moment is aligned parallel with the magnetic field the spin presents the state of minimum energy whereas if antiparallel the state would be of maximum energy. In a sample with a large number of spin $\frac{1}{2}$ nuclei (of the order of the Avogadro´s number) in an external magnetic field $\vec{B}$, the polarisation axis for a single spin $\frac{1}{2}$ nucleus does not correspond to the external magnetic field axis, but to a partial random orientation with respect to it. It is partial because low energy orientations are more likely than those with high energy [21]. Magnetic fluctuations close to nuclei lead to an anisotropic distribution of nuclear spins aligned with the magnetic field called thermal equilibrium. This thermal equilibrium means that there is a net magnetisation aligned with $\vec{B}_0$, that builds up exponentially with a time constant T_1 (known as the longitudinal relaxation time) as soon as an external magnetic field is applied to a demagnetised sample [14], [21]. This relaxation time may vary between milliseconds and days depending on the sample and sample environment ($\vec{B}_0$ strength and temperature)[21].

It is possible to tilt the magnetisation by applying a radiofrequency pulse with a precise strength, phase and duration at the Larmor frequency. The magnetisation left in this state is called transversal magnetisation. It is better seen in a frame rotating with the same nuclear Larmor frequency. For example, if this longitudinal magnetisation is rotated 90º about an axis $\vec{y}$ perpendicular

to the magnetic field the transversal magnetisation is initially left, in this rotating frame, pointing along the $\vec{x}$ axis as shown in figure 1.1.

The transversal magnetisation precesses around $\vec{B}_0$ and starts decaying since the precessing spins progressively loose coherence due to spin-spin interactions or other fluctuations. The decay is typically exponential with a time constant T_2 or T_2^* if $\vec{B}$ and radiofrequency inhomogeneities or other imperfections are taken into account. Phenomenologically this experiment can be described with the Bloch equations [21]:

$$\frac{d\vec{M}}{dt} = \vec{M} \times \vec{B} - \frac{M_x - M_x^{eq}}{T_2^*}\vec{i} - \frac{M_y - M_y^{eq}}{T_2^*}\vec{j} - \frac{M_z - M_z^{eq}}{T_1}\vec{k} \tag{1.3}$$

with a solution of

$$M_x(t) = [M_x(0)cos(\omega_0 t) + M_y(0)sin(\omega_0 t)]e^{\frac{-t}{T_2^*}} \tag{1.4}$$

$$M_y(t) = [-M_x(0)sin(\omega_0 t) + M_y(0)cos(\omega_0 t)]e^{\frac{-t}{T_2^*}} \tag{1.5}$$

$$M_z(t) = M_z^{eq} + [M_z(0) - M_z^{eq}]e^{\frac{-t}{T1}} \tag{1.6}$$

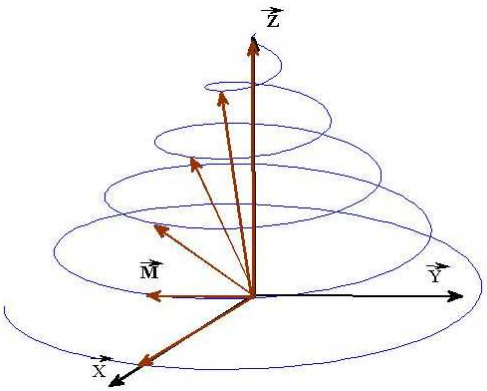

Figure 1.1: *View of the tilted magnetisation in the laboratory frame and the rotating frame. In the laboratory frame the magnetisation describes a spiral with a period correponding to the Larmor frequency. In the rotating frame, under RF irradiation at resonance the magnetisation precesses in the X-Z plane from* $\vec{Z}$ *to*$\vec{X}$.

By Lenz-Faraday law a bulk magnetisation oscillating with frequency ω_0 inside a coil will induce a voltage s that will decay with T_2^* as shown in equation 1.7. This signal is called free induction decay (FID) [21].

$$s = ae^{(i\Omega - \frac{1}{T_{2^*}})t} \tag{1.7}$$

where $\Omega = \omega_0 - \omega$ and $|a|$ is the maximum voltage.

The signal interpretation: NMR spectrum

The NMR signal is amplified by a factor determined by the gain and recorded by digitisation with a reference signal at the carrier frequency close if not equal to the Larmor frequency. The digitisation frequency must be at least twice of the registered signal (Nyquist criterion) otherwise aliasing would be present [30].

Fourier transform

Once the FID is obtained a Fourier transformation is made for spectral analysis. The mathematical expression for the Fourier transform $S(\omega)$ of a time dependent function s(t) is [21]:

$$S(\omega) = \int_0^\infty s(t)e^{-i\omega t}dt \tag{1.8}$$

Applying a Fourier transform to an FID passes it from the time domain to the spectrum in the frequency domain.

Zero filling, filter application and averaging were some of the techniques used to improve the spectrum.

Zero filling

Points suppression was needed in the data analysis of FIDs with initial ringdown or with excessive gain at the beginning of the decay. In this case the first data points were suppressed, and the rest of the FID was moved onto

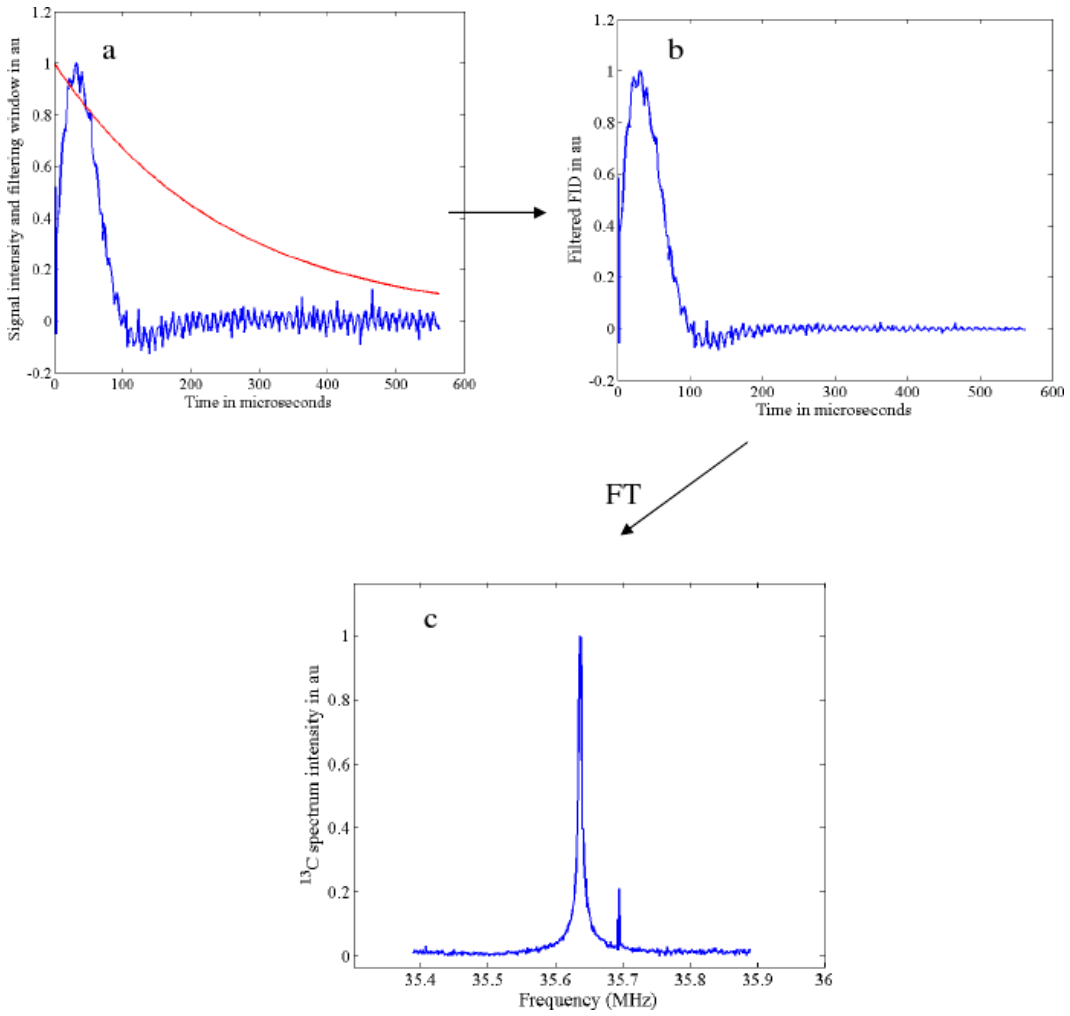

Figure 1.2: *A solid state ^{13}C FID is shown in figure 1.2(a) along with a decaying exponential curve corresponding to a 4 kHz filter. The convolution of both curves yields the filtered FID in figure 1.2(b). Figure 1.2(c) shows the Fourier transform of the filtered FID.*

these points. The remaining empty elements of the data vector were filled with zeros.

Filtering

Filtering was achieved by convolving the FID with an exponential decay envelope so the final noisy points in the tail of the FID were less important than the first ones which form the FID (figure 1.2). The price paid is a broader

spectrum, which, in the solid state, with such a large dipolar broadening, is not so significant provided the filter is not larger than this dipolar broadening [30].

Averaging

When signal-to-noise ratio (SNR) was a problem, it was necessary to take several acquisitions (n FIDs) and to average them since SNR increases with $\sqrt{n}$. For maximum sensitivity a full saturation pulse could be used (for instance, a 90^o pulse). If the T_1 was very long and depending on the number of required averages this process could take several hours or more, and then the stability of the equipment during this time was a factor to be taken into account in the experiment.

1.2 The spin Hamiltonian

For a more detailed description of relaxation processes it is necessary to explain the interactions between spins quantum-mechanically. A spin $\hat{I}$ in a magnetic field presents $2\hat{I}+1$ eigenstates which are associated with different positions with respect to the magnetic field. For a spin of $\hat{I}=\frac{1}{2}$ the possible states are $|+\rangle$ (parallel), $|-\rangle$ (antiparallel) or a linear combination of the two states ($|\psi\rangle = a\,|+\rangle + b\,|-\rangle$) [1], [2], [21]. This is the case for protons and ^{13}C. The evolution of the system follows the time dependent Schrödinger equation [21]:

$$\frac{d}{dt}|\psi_T(t)>= -i\hat{H}_T|\psi_T(t)> \tag{1.9}$$

where $\hat{H}_T$ is a hermitian operator associated to the total energy of the system (referred to as the Hamiltonian) and $|\psi_T(t)>$ is the time dependent wave function of the system. In NMR it is possible to limit the description of the wave functions to spin operators (spin Hamiltonian hypothesis)[21].

$$\frac{d}{dt}|\psi_{spin}(t)>\approx -i\hat{H}_{spin}|\psi_{spin}(t)> \tag{1.10}$$

where now $|\psi_{spin}(t) >$ refers to the state of the nuclear spins and $\hat{H}_{spin}$ involves only spin terms.

Spin angular momentum operators

The spin angular momentum operator $\hat{I}$ presents three components $\hat{I}_x$, $\hat{I}_y$ and $\hat{I}_z$ so $\hat{I}^2 = \hat{I}_x^2 + \hat{I}_y^2 + \hat{I}_z^2$ and $\hat{I}^2|I,m >= \hbar^2 I(I+1)|I,m >$, the latter describing the eigenfunctions of $\hat{I}^2$. The three components fulfill the following relationships:

$$[\hat{I}_i, \hat{I}_j] = i\hbar\hat{I}_k \tag{1.11}$$

where (i,j,k) is any of these combinations: (x,y,z), (y,z,x) or (z,x,y). For the z angular momentum component $\hat{I}_z|I,m >= m|I,m >$, where m can take a value -I, -I+1, ...,I-1, I.

The operators $\hat{I}_x$ and $\hat{I}_y$ may be combined to yield two other operators $\hat{I}_+$ and $\hat{I}_-$:

$$\hat{I}_+ = \hat{I}_x + i\hat{I}_y \tag{1.12}$$

$$\hat{I}_- = \hat{I}_x - i\hat{I}_y \tag{1.13}$$

For an isolated nuclear spin $\hat{I} = \frac{1}{2}$ the values of m are either $+\frac{1}{2}$ or $-\frac{1}{2}$. The operators $\hat{I}_+$ and $\hat{I}_-$ produce a change in m in the spin eigenvector as shown in equations :

$$\hat{I}_+|\frac{1}{2},-\frac{1}{2} >= \frac{1}{2}\hbar|\frac{1}{2},+\frac{1}{2} > \tag{1.14}$$

$$\hat{I}_-|\frac{1}{2},+\frac{1}{2} >= -\frac{1}{2}\hbar|\frac{1}{2},-\frac{1}{2} > \tag{1.15}$$

which translates into a change of orientation of the spin with respect to the magnetic field.

1.2.1 Spin interactions and Hamiltonians

Several interactions must be considered to study solid state NMR. Usually, the Hamiltonian for a single spin species isolated from the lattice under radiofrequency irradiation in a solid can be expressed as:

$$\hat{H} = \hat{H}_z + \hat{H}_{RF}(t) + \hat{H}_D + \hat{H}_C + \hat{H}_Q + \hat{H}_J \tag{1.16}$$

where $\hat{H}_z$ is the Zeeman Hamiltonian, $\hat{H}_{RF}(t)$ corresponds to the radiofrequency field, $\hat{H}_D$ is the dipolar Hamiltonian, $\hat{H}_C$ is the chemical shift, $\hat{H}_Q$ is the quadrupolar Hamiltonian and $\hat{H}_J$ is the J coupling Hamiltonian.

The Zeeman interaction

The Zeeman interaction is expressed as $\omega_0 \hat{I}_Z$ for spins $\frac{1}{2}$ where ω_0 is the Larmor frequency for the respective nuclei. It presents a large interaction in electrons (660 times the Zeeman interaction for protons) and far weaker interactions for nuclei with low gyromagnetic ratios like ^{13}C or ^{15}N. In a sample in a 3.35 T magnet, the Larmor frequency is 142.6 MHz for proton spins, 35.88MHz for ^{13}C spins, 14.45 MHz for ^{15}N and 94.0 GHz for electrons.

The chemical shift

This interaction is mainly intramolecular and it is due to the electron cloud that surrounds the nucleus. Nuclei experience a different magnetic field $\delta\vec{B}$ depending on the position in the molecule [21]. The chemical shift is tensorial and under the so called the secular approximation it may be considered scalar (one single component), being $\hat{H}_c = \delta\gamma\omega_0\hat{I}$. The strength of the chemical shift interaction for protons in glycerol at 3.35 T is usually less than 1 kHz.

J-coupling and quadrupolar coupling

The J-coupling is as an interaction mediated by an electron between two nuclear spins. It is also a tensorial interaction and it can be considered isotropic

in some liquids where the components of the tensor are averaged out. The expression in this last case is $\hat{H} = 2\pi J \hat{I}_z \hat{S}_z$. Its magnitude does not depend on the magnetic field and is typically a few Hz for ^{1}H-^{1}H coupling, and a few 100 Hz for a ^{13}C-^{1}H. The quadrupolar interaction appears for nuclei with spin $> 1/2$ and the interaction may range from a few kHz to a few MHz or more [21].

The dipolar coupling

Dipolar interactions occur when a small magnetic field produced by one spin interacts with another spin. The interaction between two spins i and j separated by a distance $\vec{r} = r\vec{u}_r$ can be expressed by equation 1.17 [21]:

$$\hat{H}_{DI,S} = b_{I,S}(\vec{I}\vec{S} - 3(\vec{I}\vec{u}_r)(\vec{S}\vec{u}_r)) \tag{1.17}$$

where $b_{I,S} = \frac{\mu_0}{4\pi}\frac{\gamma_I \gamma_S \hbar}{r_{IS}^3}$ [21]. In table 1.1 some calculated values are given for the dipolar strengths between various species of interest, for a range of concentrations.

Molar	Dist.(nm)	e-e(MHz)	e-^1H(MHz)	e-^{13}C(kHz)	^1H $-^1$ H(kHz)
110.0	0.247	3466.6	5.25	1313	7.96
7.6	0.602	239.52	0.36	90.7	0.55
6.8	0.624	215.77	0.33	81.7	0.49
2	0.940	63.03	0.096	23.9	0.14
1	1.184	31.51	0.048	11.94	0.072
0.095	2.59	3.00	0.0045	1.13	0.00687
0.024	4.10	0.76	0.00114	0.286	0.00174
0.015	4.80	0.47	0.000716	0.179	0.0011

Table 1.1: Dipolar interactions in frequency units for different spins in different concentrations (first column). The average distance (Dist.) is supposed for homogeneous distribution of spins of the same species. The dipolar strength corresponds to the distances shown in the second column. In this thesis, typical concentration of 95 mM were used in TEMPO radicals, 24 mM in lanthanides, 15 mM in trityl radical, 2 and 1 M in [^{13}C-1] Na acetate, 110 M with ^{1}H spins, and approximately 6.8 M and 7.6 M for glycerol in the mixtures of 1:1 glycerol-water.

Equation 1.17 may be expanded in terms following the Van-Vleck alphabet [14]:

$$\hat{H}_{DI,S} = \hat{A} + \hat{B} + \hat{C} + \hat{D} + \hat{E} + \hat{F} \tag{1.18}$$

where

$$\hat{A} = \hat{I}_z \hat{S}_z (1 - 3cos^2\theta) \tag{1.19}$$

$$\hat{B} = -\frac{1}{4}(1 - 3cos^2\theta)(\hat{I}_+ \hat{S}_- + \hat{I}_- \hat{S}_+) \tag{1.20}$$

$$\hat{C} = -\frac{3}{2} sin\theta cos\theta e^{-i\phi}(\hat{I}_z \hat{S}_+ + \hat{I}_+ \hat{S}_z) \tag{1.21}$$

$$\hat{D} = \hat{C}^+ = -\frac{3}{2} sin\theta cos\theta e^{i\phi}(\hat{I}_z \hat{S}_+ + \hat{I}_+ \hat{S}_z) \tag{1.22}$$

$$\hat{E} = -\frac{3}{4} sin^2\theta e^{-2i\phi}(\hat{I}_+ \hat{S}_+) \tag{1.23}$$

$$\hat{F} = -\frac{3}{4} sin^2\theta e^{2i\phi}(\hat{I}_- \hat{S}_-) \tag{1.24}$$

From these terms, $\hat{A}$ and $\hat{B}$ are secular (i.e. they commute with the Zeeman Hamiltonian) for the case of two like spins whereas for two unlike spins only $\hat{A}$ is secular. Secular interactions broaden the nuclear resonance line. Non secular interactions affect the Zeeman eigenstates slightly in high fields. This change in the energy levels may be treated with perturbation theory in high fields [14]. The term $\hat{B}$ contribute to energy conserving flip-flops and $\hat{E}$ and $\hat{F}$ are responsible for those interactions where two spins change orientation simultaneously.

As deduced from the previous expressions, the dipolar interaction is tensorial. It depends on the cube of the distance between spins and on the orientation of the internuclear axis with respect to the magnetic field as it is shown in figure 1.3.

The irradiation terms and the rotating frame

Under a non negligible radiofrequency magnetic field applied at the frequency of reference ω, the term to be added in the Hamiltonian involves a spin component perpendicular to the $\vec{z}$ component multiplied with a time dependent

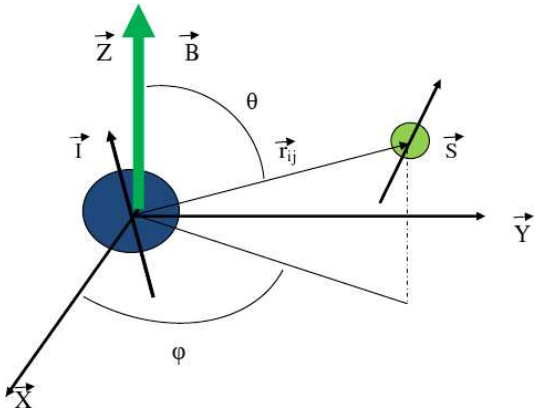

Figure 1.3: *Graphical dipolar interaction between two spins I and S spaced by* $\vec{r}$ *under a magnetic field* $\vec{B}$ *aligned with the* $\vec{Z}$ *direction and with spherical angular coordinates* θ *and* ϕ*.*

harmonic function: $\hat{H}_{RF} = -\frac{1}{2}B_1(cos(\omega t + \varphi)\hat{I}_x + sin(\omega t + \varphi)\hat{I}_y)$, where φ is the offset [21]. When this term is present the spin system may be expressed in the rotating frame by applying a transformation which averages out the non secular terms and therefore simplifies the Hamiltonian expression. This transformation removes the time dependence of the Hamiltonian in the laboratory frame. The transformation of $\hat{H} = \omega_0\hat{I}_z + \hat{A} + \hat{B} + \hat{C} + \hat{D} + \hat{E} + \hat{F} + \hat{H}_{RF}$ to the rotating frame is (after neglecting the non-secular terms) [14], [21]:

$$\hat{H}_{rot} = \hat{U}^+\hat{H}\hat{U} - \omega\hat{I}_z \tag{1.25}$$

$$= (\omega_0 - \omega)\hat{I}_z + \hat{A} + \hat{B} + \omega_{nut}(\hat{I}_x + \hat{I}_y); \tag{1.26}$$

where $\hat{U} = e^{-i\omega_0\hat{I}_z t}$ and the terms in $\hat{I}_Z$ is the effective Zeeman term.

The part of the Hamiltonian that remains after this transformation is the part that commutes with $\hat{I}_z$. In equation 1.26, the closer the irradiation frequency approaches the resonance condition, the smaller the effective Zeeman term becomes. At some point ($\omega \simeq \omega_0$) the dipolar terms would be comparable to the Zeeman term in the rotating frame. This is illustrated in figure 1.4.

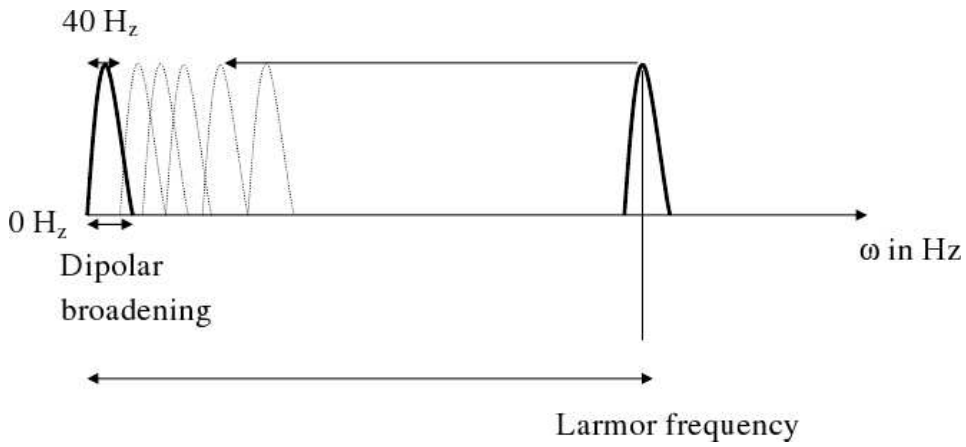

Figure 1.4: *When a radiofrequency magnetic field is applied the bulk magnetisation follows the effective magnetic field which is smaller the closer it is to the resonance frequency. When this effective magnetic field is small enough it is comparable to the NMR linewidth or in other words, with the dipole-dipole interaction strength.*

The dipolar strength is the main cause of line broadening. In the rotating frame the effective field may be comparable to this broadening.

1.2.2 The density matrix

Instead of a single spin usually there is a large number of spins in a sample. The number is comparable to Avogadro's number which is of the order of 10^{23}. The state of a system of N spins may be expressed by the eigenvector: $|\psi>=\sum_{r=1}^{r=N} c_r|r>$ where $c_r =< r|\psi >$, with a normalisation condition of $\sum_r |c_r|^2 = 1$.

According with the central limit theorem the average state may be known with a degree of accuracy [21]. The spin density matrix $\hat{\rho}$ is defined as:

$$\hat{\rho} = \overline{|\psi >< \psi|} = \frac{\sum_{i=1}^{N} |\psi >< \psi|}{N} \tag{1.27}$$

In the Boltzmann distribution, for a number of particles under a Hamiltonian

$\hat{H}$ at a temperature T, the density matrix may be expressed as:

$$\hat{\rho} = \frac{e^{-\frac{\hbar\hat{H}}{k_B T}}}{Tr(e^{-\frac{\hbar\hat{H}}{k_B T}})} \tag{1.28}$$

where k_B is the Boltzmann constant. In the matrix representation the diagonal terms yield the populations and the off-diagonal terms represent the coherences or partially aligned spins with a direction perpendicular to the magnetic field [21]. The net longitudinal polarisation for spin $I = \frac{1}{2}$ may be considered as the difference between lower energy population and the higher energy population. In this case of $I = \frac{1}{2}$ and for low temperatures, the polarisation is $P = tanh(\frac{\hbar\omega}{2k_B T})$ [3], [14], [21]. The expectation value for an operator $\hat{A}$ can be calculated with the density matrix as shown in equation 1.29:

$$< \hat{A} >= Tr\{\hat{\rho}\hat{A}\} = \sum_{r,s=1}^{N} < r|\hat{A}|s >< s|\hat{A}|r > \tag{1.29}$$

Density matrix evolution

The calculation of the density matrix at any time allows the determination of any observable operator, and therefore its calculation is implicit in the explanation of nuclear relaxation.

The evolution of this operator under the action of a Hamiltonian is given by the solution of the Liouville-von Neumann equation, in equation 1.30:

$$\frac{d\hat{\rho}(t)}{dt} = -i[\hat{H}(t), \hat{\rho}(t)] \tag{1.30}$$

With the initial condition of known $\hat{\rho}(t_0)$, a solution for the previous equation is given by equation 1.31 with the aid of a unitary operator $\hat{U}$ called a propagator:

$$\hat{\rho}(t) = \hat{U}(t, t_0)\hat{\rho}(t_0)\hat{U}(t, t_0)^{+} \tag{1.31}$$

For this to happen, the required propagator must satisfy equation 1.32:

$$\frac{d\hat{U}(t,t_0)}{dt} = -i\hat{H}(t)\hat{U}(t,t_0) \tag{1.32}$$

If the Hamiltonian is time-independent, the propagator expression may be easily deduced:

$$\hat{U}(t,t_0) = e^{-i\hat{H}(t-t_0)} \tag{1.33}$$

whereas if the Hamiltonian is time dependent, the propagator may be expressed in terms of the Dyson operator $\hat{T}$ [18], [26]:

$$\hat{U}(t,t_0) = \hat{T}e^{-i\int_{t_0}^{t}\hat{H}dt} \tag{1.34}$$

However an analytical expression for this propagator is difficult to find. The Average Hamiltonian Theory [18] may offer acceptable solutions for the cases where the Hamiltonian is periodic and the observations are stroboscopic and synchronised with the Hamiltonian period. In this case the propagator may be expressed with the Magnus expansion in equation 1.35 [26]:

$$\hat{U}(t,t_0) = e^{-i(\bar{H}^{(1)}+\bar{H}^{(2)}+\bar{H}^{(3)}+...)t} \tag{1.35}$$

With the Baker-Campbell-Hausdorff expression [26], $\bar{H}^{(1)}$ and $\bar{H}^{(2)}$ may be calculated as:

$$\bar{H}^{(1)} = \frac{1}{t}\int_{t_0}^{t}\hat{H}dt \tag{1.36}$$

$$\bar{H}^{(2)} = \frac{-i}{2*t}\int_{t_0}^{t}dt'\int_{t_0}^{t}[\hat{H}(t'),\hat{H}(t')]dt \tag{1.37}$$

The accuracy of this expansion depends on the convergency of the Hamiltonian norm with the time and on how many terms are chosen [12], [26].

Hard and soft pulses.

In solid state NMR hard pulses are used when it is not required to excite a selected spectral band. They can be made very short (a few microseconds, if not less) provided enough power can be delivered to the coil without problems. A short hard pulse affects a large bandwidth. The full width at half maximum is $\frac{1.21}{T}$ [8],where T is the irradiation time. Adiabatic inversion pulses belong to a particular family of adiabatic pulses. They differ from hard pulses in that the amplitude and reference frequency are modulated during the excitation [8]. In adiabatic inversion pulses the magnetisation rotates along the effective field axis from $+\vec{Z}$ to $-\vec{Z}$. The adiabatic inversion pulse WURST (wideband, uniform rate and smooth truncation) designed by Kupce *et al* [19] has been used to invert up to 80 kHz wide proton magnetisation at 1.5 K and 3.35 T in this project with a typical length of 1 ms and a maximum amplitude of 20 kHz.

An advantage of adiabatic pulses is the small amount of power required for experimental implementation. With a remotely tuned probe, less than 80 W was necessary for proton magnetisation inversion over a bandwidth of 80 kHz while more than 350 W were required with a hard pulse inverting the same bandwidth.

1.3 The electron spin

The electron paramagnetic resonance (EPR) spectrum is usually very complex, being composed of many lines that may be divided into subgroups of resonance lines corresponding to interactions with nuclei [2]. In cases where there is g-anisotropy the orientation of the spin with respect to the field will alter the resonance lines. The ground state of a paramagnetic centre may be considered as a group of electronic levels separated by a few wave numbers. A valid representation of the paramagnetic centre is obtained with the effective spin S, so the total number of levels are $2S + 1$. For a free atom the electronic

magnetic dipole moment can be expressed as $\vec{\mu} = -g_J \beta \vec{J}$ [2], [27] and with a Hamiltonian $\hat{H} = -\vec{\mu}\vec{B} = g_J \beta(\vec{B}\vec{S})$, where S is the effective spin of the electron, g_J is the Lande factor and β is the Bohr magneton. Specially in the case of electrons the Zeeman interaction depends on the angle that the main magnetic field makes with certain axes defined by the local symmetry of the magnetic surroundings. To take into account this anisotropy, the expression for the Hamiltonian can be written as [2]:

$$\hat{H} = \beta(\vec{B}\vec{\vec{g}}\vec{S}) \tag{1.38}$$

where $\vec{\vec{g}}$ is a tensor. The relaxation times T_1 and T_2 are much shorter than those for nuclei [3].

1.4 Introduction to longitudinal relaxation

A phenomenological description by Bloch was introduced in section 1.1.1, where the bulk magnetisation relaxes in the transverse plane with a spin-spin relaxation time T_2 and back to thermal equilibrium in the longitudinal direction with a spin-lattice relaxation time T_1. Microscopically it is necessary to account for any fluctuation in the surroundings that will alter the state of the spin [14], [35]. These fluctuations may be represented classically with a sum of spin operators $\hat{V}_\mu$ multiplied by a function of time $f_\mu(t)$ so $f_\mu(t)f^*_\nu(t) = \delta_{\mu\nu} f_\mu(t) f^*_\mu(t) = \delta_{\mu\nu} G_\mu(|t - t'|)$, where $G_\mu(t) = G_\mu(0)e^{-|t|/\tau_{c\mu}}$ is the autocorrelation function and in many experimental situations can be represented as an exponential that decays with the so called correlation time $\tau_{c\mu}$ corresponding to the fluctuation $\hat{V}_\mu f_\mu(t)$ [14].

By applying a strong magnetic field $\vec{B}_0 = B\vec{z}$ to a demagnetised sample of like spins, an energy exchange between the whole of spin system and the lattice may be detected by measuring the evolution of the bulk magnetisation $\hat{M}(t)$ towards its equilibrium value $\hat{M}_{eq}$. The spin system may be considered as a thermal bath with a characteristic temperature $T = T(t)$ given by the

Curie Law [35]:

$$\vec{M}(t) = \frac{CB_0}{T(t)}\vec{z} \tag{1.39}$$

Where C is a constant and $\frac{C}{T(t)}$ defines the magnetic susceptibility of the sample. The time dependence of the spin temperature $T(t)$ comes from the Van-Vleck assumption that extends the spin temperature to non-equilibrium state magnetisations [35]. In thermal equilibrium and at temperatures close to 1.5 K it is possible to expand the density matrix to first order so $\hat{\rho} \simeq A(1 - \frac{\hat{H}}{k_B T})$. This temperature is in principle the lattice temperature, but as it is associated to the spin order, it will represent the spin temperature. By reducing $A = 1$, and defining the inverse spin temperature by $\beta = \frac{1}{k_B T}$, the expression left is $\hat{\rho} = 1 - \beta\hat{H}$, where β turns out to be proportional to the spin polarisation. With this definition it is possible to describe relaxation times and lattice parameters. It also applies to the case when the Hamiltonian is given in the rotating frame (spin temperature in the rotating frame).

1.4.1 Relaxation for a nuclear spin species in the laboratory frame

In the case of a single spin species in the absence of an RF magnetic field and quadrupolar interactions in a rigid lattice (RL), the Hamiltonian $\hat{H}$ can be expressed as a Zeeman term with commuting and non commuting dipolar terms [14], [35]:

$$\hat{H} = \hat{H}_Z + \hat{H}_D^{RL} = \hat{H}_Z + \hat{H}_D^{\prime RL} + \hat{H}_D^{\prime\prime RL} \tag{1.40}$$

The relaxation to thermal equilibrium with the lattice is mediated through the dipolar terms. These dipolar terms may be separated in the rigid lattice (RL) in secular ($\hat{H}_D^{\prime RL}$) and non secular ($\hat{H}_D^{\prime\prime RL}$). The Hamiltonian corresponding to the (dipolar) interaction that relax the spin system can be expressed as fluctuations of the dipolar Hamiltonian in time regarding a Hamiltonian in

the rigid lattice $\hat{H}_{SL}$ [14], [35]:

$$\hat{H}_{SL} \equiv \hat{H}_D(t) - \hat{H}_D^{RL} \tag{1.41}$$

where $\hat{H}_D^{RL}$ is the dipolar term for the rigid lattice. These fluctuations are described with correlation functions. A correct treatment for the relaxation explanation must start from a complete Liouville von Neumann expression or master equation:

$$\frac{d\hat{\rho}}{dt} = -i[\hat{H}_0, \hat{\rho}] - \sum G_\mu(0) \int_0^\infty [\hat{V}_\mu, [\hat{V}_\mu(t), (\hat{\rho} - \hat{\rho}_L)]] e^{-\frac{t}{\tau_{c\mu}}} dt \tag{1.42}$$

where $\hat{V}_\mu(t) = e^{-i\hat{H}_Z t}\hat{V}_\mu e^{+i\hat{H}_Z t}$ and $\hat{\rho}_L = 1 - \beta_L \hat{H}_0$, where β_L is the inverse spin temperature of the lattice. In high field $\hat{H}_D = \hat{H}'_D + \hat{H}''_D$. The density matrix $\hat{\rho}$ may be separated in two matrices corresponding to diagonal terms ($\hat{\rho}_1$) and off diagonal term ($\hat{\rho}_2$): $\hat{\rho} = \hat{\rho}_1 + \hat{\rho}_2$ and $\hat{\rho}_1 = 1 - \alpha\hat{H}_Z - \beta\hat{H}'_D$. For high fields $\hat{\rho}_2 << \hat{\rho}_1$, which reflects that α and β (inverse spin temperatures of Zeeman and secular dipolar baths respectively) evolve independently with $\hat{H}_Z$ and $\hat{H}'_D$ constants of motion, [14], [33]. Multiplying 1.42 by $\hat{H}'_D$ and $\hat{H}_Z$ and taking the traces, it is possible to obtain the equations for the evolution of the average value of each of the two operators in 1.43 and 1.44 respectively:

$$\frac{d < \hat{H}'_D >}{dt} = Tr(-i[\hat{H}'_D, \hat{H}_0]\hat{\rho}_2) - \frac{1}{T_D}(< \hat{H}'_D > - < \hat{H}'_D >_L) \tag{1.43}$$

$$\frac{d < \hat{H}_Z >}{dt} = Tr(-i[\hat{H}_Z, \hat{H}_0]\hat{\rho}_2) - \frac{1}{T_{1Z}}(< \hat{H}_Z > - < \hat{H}_Z >_L) \tag{1.44}$$

where T_{1Z} and T_D are functions of the inverse of the terms in the integral and commutators [14]. In high fields the mixing between the Zeeman and dipolar baths can be neglected and the final equations for the spin lattice relaxation for both Zeeman and dipolar baths (with inverse spin temperatures α and β respectively) are:

$$\frac{d\beta}{dt} = -\frac{1}{T_D}(\beta - \beta_L) \tag{1.45}$$

$$\frac{d\alpha}{dt} = -\frac{1}{T_{1Z}}(\alpha - \beta_L) \tag{1.46}$$

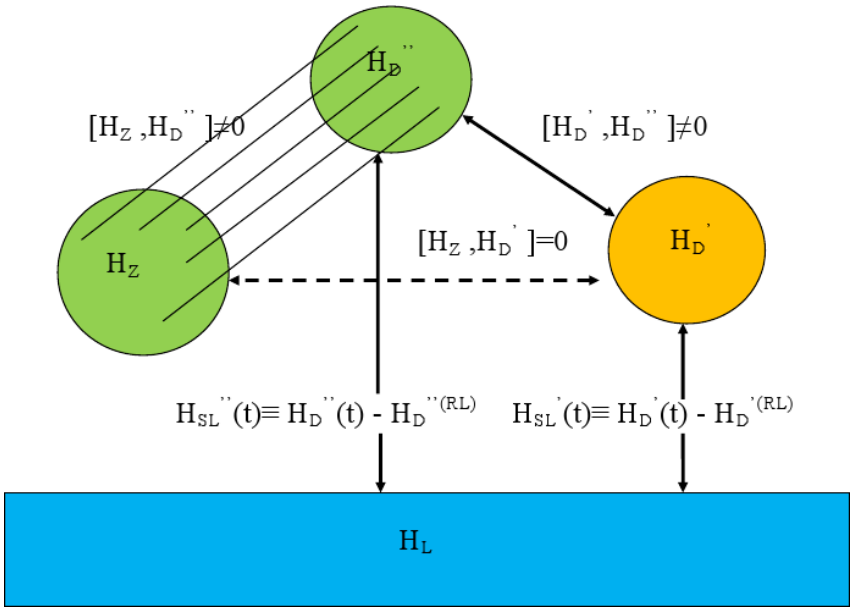

Figure 1.5: *Interactions between Zeeman and dipolar reservoirs. Since $\hat{H}_D$ does not commute with $\hat{H}''_D$, any change in this dipolar reservoir will be communicated to the Zeeman reservoir and vice versa. Communication between secular dipolar reservoir and Zeeman reservoir takes place through thermal mixing in low fields(dashed line). In high fields the thermal mixing is not important and Zeeman and secular dipolar reservoirs acquire different spin temperatures, although the secular reservoir is responsible for keeping a homogeneous inverse temperature in the Zeeman bath with energy conserving flip-flops (spectral diffusion).*

Although much slower with respect to the spin lattice interaction, it is possible to develop a mathematical expression for the heat exchange between α and β reservoirs at high field and in the laboratory frame. Starting from an expression for the Hamiltonian as $\hat{H}_{lab} = \hat{H}_Z + \hat{H}'_D + \hat{H}''_D$ the operator $\hat{U}$ is

defined as $\hat{U} = 1 - i\hat{R}$ so it can act on any operator $\hat{Q}$ as $\hat{U}\hat{Q}\hat{U}^{+} = \hat{Q}^{*}$ and $\hat{H}_Z + \hat{H}''_D = \hat{U}\hat{H}_Z\hat{U}^{+} = \hat{H}^{*}_Z = \hat{H}_Z - i[\hat{R}, \hat{H}_Z]$, where [14] $\hat{R}$ is:

$$\hat{R} = \frac{i(\hat{D} - \hat{C})}{\omega_0} + \frac{i(\hat{F} - \hat{E})}{2\omega_0} \tag{1.47}$$

so $\hat{H}'_D = \hat{H}'^{*}_D + i[\hat{R}, \hat{H}'^{*}_D]$ and the Hamiltonian for the system is $\hat{H}_{lab} = \hat{H}_0 + i[\hat{R}, \hat{H}'^{*}_D]$, $\hat{H}_0 = \hat{H}^{*}_Z + \hat{H}'_D{}^{*}$. The density matrix can be expressed as $\hat{\rho} = 1 - \alpha\hat{H}^{*}_Z - \beta\hat{H}'_D{}^{*} + \hat{\rho}_2$. The perturbation becomes $\hat{V} = i[\hat{R}, \hat{H}'^{*}_D]$. From these expressions, it can be shown that the evolution equations for α and β are given by a similar derivation as the Provotorov equations, developed later.

$$\frac{d\beta}{dt} = W\frac{\Delta^2}{D^2}(\alpha - \beta) \tag{1.48}$$

$$\frac{d\alpha}{dt} = -W(\alpha - \beta) \tag{1.49}$$

Where in this case $W = \frac{1}{Tr(\hat{I}^2_Z)}\int_0^\infty Tr([\hat{I}^{*}_Z, \hat{V}][\tilde{V}(t), \hat{I}^{*}_Z])dt$ being $\hat{I}^{*}_Z\omega_0 = \hat{H}^{*}_Z$ and $\tilde{V}(t) = e^{i\hat{H}_0 t}\hat{V}e^{-i\hat{H}_0 t}$, which would correspond to the $\hat{H}_{RL}(t)$. The dipolar interactions may be considered as a thermal bath, but since fluctuations in the non-commuting terms affect immediately the Zeeman term, they can be regarded as a thermal bath which is in close thermal contact with the Zeeman bath [14], [35]. On the other hand, the commuting dipolar term is not directly in contact with this Zeeman bath, but through the non-commuting dipolar bath, it causes thermal mixing in this case of identical spins. For unlike spins this is called cross relaxation τ_M.

If the characteristic time for the Zeeman bath to achieve equilibrium with the lattice is much shorter than the time required to achieve equilibrium with the dipolar secular bath, then both baths evolve independently and may achieve different spin temperatures [35]. These processes are illustrated in figure 1.5.

1.4.2 Electron longitudinal relaxation

The gyromagnetic ratio of the electron spin is 660 times greater than the ^{1}H spin. Electron paramagnetic resonance linewidths in solid state are typically from a few MHz broad to close to a GHz or more [2]. Along with the much smaller rest mass in comparison with nuclei (1800 times smaller, [21]), the electron can communicate the vibrational modes within the lattice (or phonon bath in the lattice) to the nuclear spins [3]. The three main longitudinal relaxation mechanisms are the direct process, the Raman process and the Orbach process [27]. The direct process involves a spin that flips from up to down with the accompanying emission or creation of a phonon of the same energy. This happens because of the vibrations that alter the distances and/or electric fields between electric dipoles. In the Raman process the phonon created has a higher energy and is scattered inelastically. Typically, at low temperatures (1.5 K or less) the direct process dominates over the Raman process [5].

Sometimes the splittings due to electric fields are smaller than the energy presented by some phonons. Then it is possible for an electron in the upper Zeeman level of the ground state to get to an excited state by the absorption of a phonon and return to a lower Zeeman level in the ground state in a process that is known as Orbach process [27].

The electron resonance linewidth may be broadened by hyperfine electron-electron interactions and g-factor anisotropy. When the line is not homogeneous, continuous wave irradiation produces a non uniform excitation (hole burning) [11], and it is incorrect to define a single spin temperature. The line should then be considered as being composed of many spin packets in communication with each other through cross relaxation [10]. When cross relaxation is much faster than the contact with the lattice, the electron line may then be considered homogeneous. This may be observed with large electron irradiation in high fields [10].

1.4.3 Relaxation in the rotating frame for a single spin species: the Provotorov equations

In the particular case of a system of like spins in high magnetic field and isolated from the lattice, there are distinct spin temperatures for the Zeeman and the secular dipolar bath. It is possible to consider the Zeeman and secular dipolar baths also in the rotating frame [14], [35].

For a small RF magnetic field applied to the spin system, it can be demonstrated that there is thermal mixing between the Zeeman and dipolar reservoirs [14], [35]. The mathematical description is included in this thesis for completeness sake. Readers are referred to Goldman *et al* for a wider explanation [14]. In the case of a single spin species, in the rotating frame (with $\Delta = \omega_0 - \omega$) the Hamiltonian can be expressed as $\hat{H} = \Delta\hat{I}_Z + \hat{H}'_D + \omega_1\hat{I}_x$, which in analogy with the expression for $\hat{H}_0$ it can be expressed as $\hat{H}_0 = \Delta\hat{I}_Z + \omega_1\hat{I}_x$, which is composed by two quasi-constants of motion and a perturbation component coming from an RF field ω_1 that mixes both of them. For the case of large RF irradiation (with similar magnitude to the local field) an equilibrium is reached in a time comparable to T_2. On the other hand, if the RF field is weak, then the system does not evolve significantly in a time T_2 [14]. In the rotating frame the expression for the density matrix in this second case is expressed as $\hat{\rho} = 1 - \alpha\Delta\hat{I}_Z - \beta\hat{H}'_D$, where α and β are the inverse spin temperatures of the Zeeman and dipolar terms. To find the evolution of this density matrix, it is necessary to solve the Liouville von Neumann equation in a reference frame rotating around $\hat{H}_0$ and considering the RF term as a perturbation. The Liouville equation is given without including the lattice, which may be added at the end. The former expression of the density matrix is transformed to a frame rotating with the operator $\hat{U}_2 = e^{i\hat{H}_0 t}$, so any operator $\hat{Q}$ would be represented as $\tilde{Q} = \hat{U}_2\hat{Q}\hat{U}_2^+$ with this transformation.

$$\frac{d\tilde{\rho}}{dt} = -i\omega_1\left[\tilde{I}_x, \tilde{\rho}\right] \tag{1.50}$$

By integration of this expression between 0 and a time t, the equation 1.50 becomes:

$$\tilde{\rho}(t) - \hat{\rho}(0) = -i\omega_1 \int_0^t [\tilde{I}_x(t'), \tilde{\rho}(t')]dt' \tag{1.51}$$

The density matrix is separated into two matrices, diagonal and off diagonal $\hat{\rho}(0) = \hat{\rho}(0)_1 + \hat{\rho}(0)_2$ in a similar fashion as is done with the density matrix for the equations of relaxation in the laboratory frame. The density matrix is then expanded to second order in the following equation:

$$\begin{aligned}\tilde{\rho}(t) - \hat{\rho}(0) = &- i\omega_1 \int_0^t [\tilde{I}_x(t'), \hat{\rho}_1(0)]dt' - \omega_1^2 \int_0^t dt' \int_0^{t'} [\tilde{I}_x(t'), [\tilde{I}_x(t''), \hat{\rho}_1(0)]]dt'' - \\ &- i\omega_1 \int_0^t [\tilde{I}_x(t'), \hat{\rho}_2(0)]dt' - \omega_1^2 \int_0^t dt' \int_0^{t'} [\tilde{I}_x(t'), [\tilde{I}_x(t''), \hat{\rho}_2(0)]]dt''\end{aligned} \tag{1.52}$$

The last two terms in equation 1.52 are neglected (see below). The first two terms are multiplied by an operator $\hat{Q}$ that commutes with $\hat{H}_0$ and $\hat{\rho}_1(0)$. It is worthwhile to note that $[\hat{Q}, \tilde{I}_x(t)] = \hat{U}_2[\hat{Q}, \hat{I}_x(t)]\hat{U}_2^+$ and that $Tr([\tilde{I}_x(t'), \hat{\rho}_1(0)]\hat{Q}) = Tr(\tilde{I}_x(t')[\hat{\rho}_1(0), \hat{Q}]) = 0$. A substitution $\tau = t' - t''$ applied before taking the traces results in:

$$Tr[\hat{Q}, \tilde{\rho}(t) - \hat{\rho}(0)]_1 = -\omega_1^2 \int_0^t (t - \tau) Tr[\hat{Q}, \tilde{I}_x(\tau)][\hat{I}_x, \hat{\rho}_1(0)]d\tau \tag{1.53}$$

It is possible to use $Tr([\hat{I}_x, \hat{\rho}_1(0)][\hat{Q}, \tilde{\rho}(\tau)]) = Tr(\hat{I}_x[\hat{\rho}_1(0), [\hat{Q}, \tilde{\rho}(\tau)]])$. Due to the fact that $[\hat{\rho}_1(0), \hat{Q}] = 0 \Rightarrow [\hat{\rho}_1(0), [\hat{Q}, \tilde{I}_x(\tau)]] = [\hat{Q}, [\hat{\rho}_1(0), \tilde{I}(\tau)]]$ so the equation 1.53 can be expressed as:

$$Tr[\hat{Q}, \tilde{\rho}(t) - \hat{\rho}(0)]_1 = -\omega_1^2 \int_0^t (t - \tau) Tr[\hat{Q}, \hat{I}_x][\tilde{I}_x(\tau), \hat{\rho}_1(0)]d\tau \tag{1.54}$$

The previous integral goes to zero in a short time ($\approx T_2$) [14]. Since the evolution of the system is very slow, it is possible to choose $t >> \tau$, so $\tau \leq T_2$. In this way, it is reasonable to approximate $\int_0^t Tr(...)d\tau \cong t \int_0^\infty Tr(...)d\tau$. The approximation that $\hat{\rho}_2(0) << \hat{\rho}_1(0)$ allows the contribution of the $\hat{\rho}_2(0)$ terms

to be neglected. The final equation is:

$$\frac{dTr(\hat{Q}\tilde{\rho})}{dt} = -\omega_1^2 \int_0^\infty Tr([\hat{Q}, \hat{I}_x][\tilde{I}_x(\tau), \hat{\rho}_1(0)])d\tau \tag{1.55}$$

By making $\hat{Q} = \hat{I}_z$, and considering the expression of the density matrix at the beginning the equation 1.55 is:

$$\begin{aligned} Tr(\hat{I}_Z^2)\frac{d\alpha}{dt} = -\omega_1^2(\alpha - \beta) \int_0^\infty Tr([\hat{I}_z, \hat{I}_x][\tilde{I}_x(\tau), \hat{I}_z(0)])d\tau - \\ -\omega_1^2 \frac{\beta}{\Delta} \int_0^\infty Tr([\hat{I}_z, \hat{I}_x][\tilde{I}_x(\tau), \hat{H}_0])d\tau \end{aligned} \tag{1.56}$$

The last integral is equal to zero. The first integral can be evaluated from $[\tilde{I}_x(\tau), \hat{H}_0] = i\frac{d\tilde{I}(\tau)}{d\tau}$. By integrating between t and ∞: $Tr(i[\hat{I}_Z, \hat{I}_x]\tilde{I}_x(\infty)) - Tr(i[\hat{I}_Z, \hat{I}_x]\hat{I}_x)$. The term in infinity would go to zero since it becomes the free decay signal after a long time $t >> T_2$ [14]. The second term as well goes to zero.

To evaluate the first term in the equation 1.56 a new expansion is needed in $\tilde{I}_x = \hat{I}_x(\tau)cos(\Delta\tau) - \hat{I}_y(\tau)sin(\Delta\tau)$, with $\hat{I}_x(\tau) = e^{+i\hat{H}'_D\tau}\hat{I}_x e^{-i\hat{H}'_D\tau}$ and $\hat{I}_y(\tau) = e^{+i\hat{H}'_D\tau}\hat{I}_y e^{-i\hat{H}'_D\tau}$.

It is necessary to note that

$$Tr(\hat{I}_y\hat{I}_x(\tau)) = 0; \tag{1.57}$$

Since $Tr(\hat{I}_x\hat{I}_x(\tau))cos(\Delta\tau)d\tau$ is an even function, it is possible to express the previous equation 1.56 as:

$$\frac{1}{\pi Tr(\hat{I}_x^2)} \int_0^\infty Tr(\hat{I}_x\hat{I}_x(\tau))cos(\Delta\tau)d\tau = \frac{1}{2\pi Tr(\hat{I}_x^2)} \int_0^\infty Tr(\hat{I}_x\hat{I}_x(\tau))e^{i\Delta\tau}d\tau = g(\Delta) \tag{1.58}$$

In this case $g(\Delta)$ corresponds to the absorption signal at low radio frequency field [14]. It is normalised so $\int_{-\infty}^{\infty} g(\Delta)d\Delta = 1$. The final result of this mathematical development is:

$$\frac{d\alpha}{dt} = -\pi\omega_1^2 g(\Delta)(\alpha - \beta) \tag{1.59}$$

To find the expression for β it is necessary to realise that $Tr(\hat{H}_0(\tilde{\rho}(t) - \hat{\rho}(0))) \cong 0$. Then:

$$\frac{d(\hat{H}_0\tilde{\rho})}{dt} = -\Delta^2\frac{d\alpha}{dt} - D^2\frac{d\beta}{dt} \cong 0 \tag{1.60}$$

so

$$\frac{d\beta}{dt} = \frac{-\Delta^2}{D^2}\frac{d\alpha}{dt} \tag{1.61}$$

Then it is possible to arrive to the Provotorov equations 1.59 and 1.61 that reflect an evolution of the system that depends on the difference between the inverse spin temperature of Zeeman and dipolar baths in the rotating frame, and under a small RF magnetic field.

$$\frac{d\beta}{dt} = W\frac{\Delta^2}{D^2}(\alpha - \beta) \tag{1.62}$$

$$\frac{d\alpha}{dt} = -W(\alpha - \beta) \tag{1.63}$$

where $W(\Delta) = \pi\omega_1^2 g(\Delta)$, $\Delta = \omega_0 - \omega$, and $D = \gamma H'_L$, the frequency for the local field. The inverse spin temperatures vary exponentially towards thermal equilibrium. The main assumption in this part of the Provotorov theory was to consider a spin temperature for the dipolar bath in the rotating frame. By applying a small RF field to a system in equilibrium, it is possible to cool the dipolar reservoir by pumping heat to the Zeeman reservoir in the rotating frame.

1.4.4 Cross relaxation in the laboratory frame

If a system formed by two spin species I and S is isolated from the lattice, the spin relaxation depends only on dipolar interactions, and the case becomes more complicated than for a simple spin species. The Hamiltonian $\hat{H}$ for this new system is (neglecting quadrupolar interactions) [35]:

$$\hat{H} = \hat{H}_{ZI} + \hat{H}_{ZS} + \hat{H}^{RL}_{DIS} + \hat{H}^{RL}_{DII} + \hat{H}^{RL}_{DSS} \tag{1.64}$$

where the terms in Z denote Zeeman, D dipolar and RL rigid lattice. The terms in DIS correspond to the dipolar interaction between spins I and S (both I and S are nuclear spins), and DII and DSS terms correspond to homonuclear dipolar interactions for spins I and S respectively. In a semiclassical view, the spin lattice dipolar fluctuations can be considered as [35]:

$$\hat{H} \equiv \hat{H}_{DII}(t) - \hat{H}^{RL}_{DII} + \hat{H}_{DIS}(t) - \hat{H}^{RL}_{DIS} + \hat{H}_{DSS}(t) - \hat{H}^{RL}_{DSS} \tag{1.65}$$

The interactions between the different thermal reservoirs are depicted in figure 1.6 for two spin species in low fields. Following the previous notation the secular dipolar Hamiltonian is noted with $\hat{H}'_D$ and the non secular with $\hat{H}''_D$. The fluctuations are described with the corresponding correlation functions. Again $\hat{H}_{ZI}$ is in strong thermal contact with $\hat{H}''_{DII}$, and $\hat{H}_{ZS}$ with $\hat{H}''_{DSS}$, but in this situation there is thermal contact between both Zeeman reservoirs through the heteronuclear non secular dipolar reservoir. All of these dipolar baths are in thermal contact with the lattice [14], [35]. Three thermal mixing rates compete now with a cross relaxation time, corresponding to the three secular dipolar reservoirs being mixed with the non secular reservoirs and a process of cross relaxation between the Zeeman reservoir through the non secular dipolar reservoir [35]. If the magnetic field increases, the thermal mixing mechanisms become less and less efficient, as in the case of a single spin species until the point where the Zeeman baths are isolated from their respective secular dipole reservoirs. Then the secular dipolar terms for the corresponding reservoirs become constants of motion along with the Zeeman terms.

The cross relaxation process becomes more efficient when there is more probability of energy conserving processes, like zero quantum (ZQ) transitions in the case of two very similar Larmor frequencies ($\omega_I = \omega_S$), or two flips

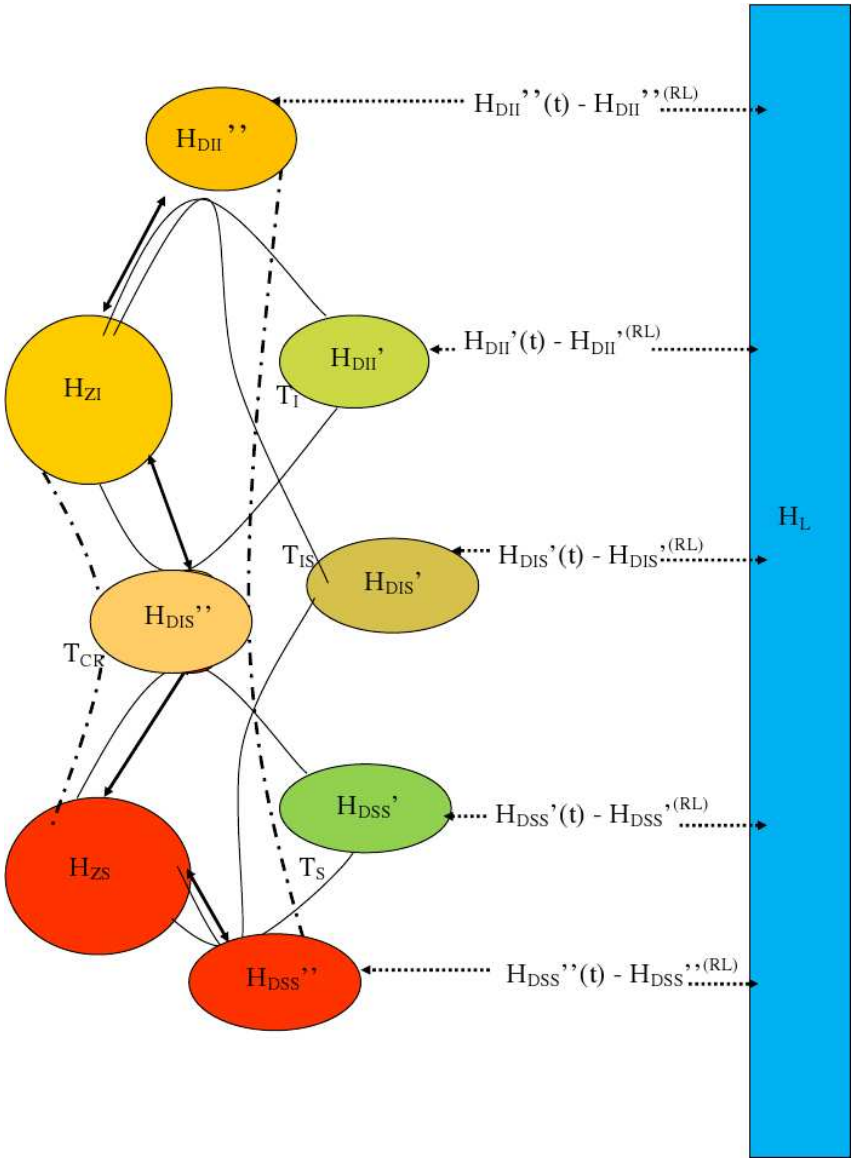

Figure 1.6: *Interactions between a Zeeman and dipolar reservoirs for two spin species. Like for the single spin species, $\hat{H}_{ZI}$ is in close thermal contact with $\hat{H}''_{DII}$, and $\hat{H}_{ZS}$ with $\hat{H}''_{DSS}$. In this case there are three secular dipolar reservoirs $\hat{H}'_{DII}$, $\hat{H}'_{DIS}$ and $\hat{H}'_{DSS}$ with three characteristic times T_I, T_S and T_{IS}. Another non secular dipolar reservoir $\hat{H}''_{DIS}$ is considered, responsible for mutual flip-flops and cross relaxation with a characteristic time T_{CR}, after Wolf, et al [35].*

and one flop, in the case of $\omega_I = 2\omega_S$ [14], [35]. In this case of only two spin species with similar Larmor frequencies these ZQ transitions do not conserve the Zeeman energy of the system. The difference in energy to enable such

transition must be supplied by dipolar baths, which may lead to different spin temperatures. For the case of two spin species with the same gyromagnetic ratio, a Hamiltonian could be written as:

$$\hat{H}_{lab} = \omega_I \hat{I}_Z + \omega_S \hat{S}_Z + \hat{H}_D \tag{1.66}$$

In a first approximation only the dipolar term $\hat{B}$ is considered relevant in the non secular dipolar baths in this treatment of cross relaxation. The Hamiltonian becomes then:

$$\hat{H}_{lab} = \omega_I \hat{I}_Z + \omega_S \hat{S}_Z + \hat{H}'_D + \hat{B} \tag{1.67}$$

where $\hat{B}$ is the corresponding part of the flip-flops in formula 1.18. Two constants of motion ($\hat{P}$ and $\hat{Q}$) are now introduced in the Hamiltonian in equation 1.67 with $\hat{P} = \hat{I}_Z + \hat{S}_Z$. Following [14] $\hat{Q}$ is defined as an orthogonal operator $\hat{Q} = \hat{H}_{lab} - \frac{\hat{P}Tr(\hat{H}_{lab}\hat{P})}{Tr(\hat{P}^2)}$, with $Tr(\hat{P}\hat{Q}) = 0$. In this way:

$$\hat{Q} = \omega_I \hat{I}_Z + \omega_S \hat{S}_Z - (\hat{I}_Z + \hat{S}_Z)\frac{\omega_I Tr(\hat{I}_Z^2) + \omega_S Tr(\hat{S}_Z^2)}{Tr(\hat{I}_Z^2) + Tr(\hat{S}_Z^2)} + \hat{H}'_D + \hat{B} \tag{1.68}$$

$$\hat{Q} = (C_S \Delta \hat{I}_Z - C_I \Delta \hat{S}_Z) + \hat{H}'_D + \hat{B} \tag{1.69}$$

with $\Delta = \omega_I - \omega_S$. C_I and C_S are the heat capacities according to Goldman [14]. With the definitions of $Tr(\hat{I}_Z^2) + Tr(\hat{S}_Z^2) = N$ (N is the total number of spins), $Tr(\hat{I}_Z^2) = C_I N$ and $Tr(\hat{S}_Z^2) = (1 - C_I)N = C_S$, the resultant Hamiltonian is

$$\hat{H}_{lab} = (C_I \omega_I + C_S \omega_S)\hat{P} + \hat{Q} \tag{1.70}$$

There is no thermal contact between the operators $\hat{P}$ and $\hat{Q}$ and in this way the cross relaxation depends only on the evolution of $\hat{Q}$. In high field, $\Delta^2 Tr((C_S \hat{I}_Z - C_I \hat{S}_Z)^2) >> Tr(\hat{B}^2)$.

The density matrix can be decomposed in two different ways, by considering the constants of motion $(C_S \hat{I}_Z - C_I \hat{S}_Z)$, $\hat{H}'_D$ and $\hat{P}$, or $\hat{I}_Z$, $\hat{S}_Z$ and $\hat{H}'_D$. In the

first case the density matrix is

$$\hat{\rho} = 1 - \alpha\Delta(C_S\hat{I}_Z - C_I\hat{S}_Z) - \beta\hat{H}'_D - \delta(C_I\omega_I + C_S\omega_S)\hat{P} + \hat{\rho}_2 \tag{1.71}$$

and in the second case:

$$\hat{\rho} = 1 - \alpha_I\omega_I\hat{I}_Z - \alpha_S\omega_S\hat{S}_Z - \beta\hat{H}'_D + \hat{\rho}_2 \tag{1.72}$$

Relating equations 1.72 and 1.71:

$$\alpha_I\omega_I = \delta(C_I\omega_I + C_S\omega_S) + \alpha\Delta C_S \tag{1.73}$$

$$\alpha_S\omega_S = \delta(C_I\omega_I + C_S\omega_S) - \alpha\Delta C_I \tag{1.74}$$

By derivation of the former expressions and using 1.62 and 1.63, it is possible to obtain the following equations corresponding to the cross relaxation between two spin species through a dipolar reservoir:

$$\frac{d\alpha_I}{dt} = -\frac{C_S}{\omega_I}W(\alpha_I\omega_I - \alpha_S\omega_S - \Delta\beta) \tag{1.75}$$

$$\frac{d\alpha_S}{dt} = -\frac{C_I}{\omega_S}W(\alpha_I\omega_I - \alpha_S\omega_S - \Delta\beta) \tag{1.76}$$

$$\frac{d\beta}{dt} = -\frac{\Delta}{D'^2}W(\alpha_I\omega_I - \alpha_S\omega_S - \Delta\beta) \tag{1.77}$$

where is in this case $W = \frac{1}{C_I C_S N}\int_0^\infty Tr(\hat{B}(e^{i\hat{H}'_{DIS}t}\hat{B}e^{-i\hat{H}'_{DIS}t}))\cos\Delta t dt$ [14].

1.4.5 Relaxation by paramagnetic impurities

Dipolar interactions between unpaired electrons and nuclei in a solid sample becomes the main source of nuclear relaxation at low temperatures (1.5 K) [3], [9], [14]. Nuclear relaxation is produced by random fluctuations of the local field caused by the electrons and experienced by the surrounding nuclei. For low concentrations the correlation time of these fluctuations can be considered to be T_{1e} [3], [5].

A particular case to be mentioned is the situation when the electron bandwidth is narrow in comparison with the nuclear Larmor frequency. The electron-

nuclear spin system would lead to a system of four energy levels, as shown in figure 1.7. Because of the strong mixing between Zeeman and non secular dipolar terms S_zI_+ and S_zI_- there is a mixture of eigenstates on each of the a, b, c and d states as shown in figure 1.7. Electron-nuclear spin flip-flop and flip-flip transitions are then slightly allowed.

Relaxation in high field happens then in a two spin energy conserving process. Because of interactions with the phonon modes of the lattice and interaction with other spins an electron spin flips and a nuclear spin becomes aligned with the magnetic field. The electron spin flips back to the orientation parallel with the magnetic field before it interacts again with another nucleus since the T_{1e} is much faster than the nuclear T_1. The rate of change of polarisation of both electron and nuclear spins could be expressed in differential equations obtained by detailed balance [3], [6]. For larger concentrations of paramagnetic impurities the dipolar interactions between electron themselves become more important and the correlation time of the electron-nuclear interactions may be considered to be T_{2e}, [3], [5]. Once the electron relaxes the surrounding nuclei, the spin order is carried further away from the paramagnetic centre with energy conserving dipolar interactions between nuclei (spin diffusion) [29].

If the electron linewidth is greater than the nuclear Larmor frequency a process involving three (two electron and one nuclear) spins or more takes place [3]. In this case different energy transitions may lead to relaxation. A thermal model may be used to describe this process in high field for homogeneous EPR lines [3], [13], [15]. The electron secular dipole-dipole reservoir establishes contact with the nuclear spin Zeeman bath. They both relax with a characteristic $T_{I,SS}$ to a common spin temperature [3]. The heat capacity of the nuclear Zeeman bath is far greater than the electron secular dipole one because of the relatively large number of nuclei with respect to the number of nuclei of unpaired electrons, and because the electron dipolar bath refers to the short range interactions [3], [6].

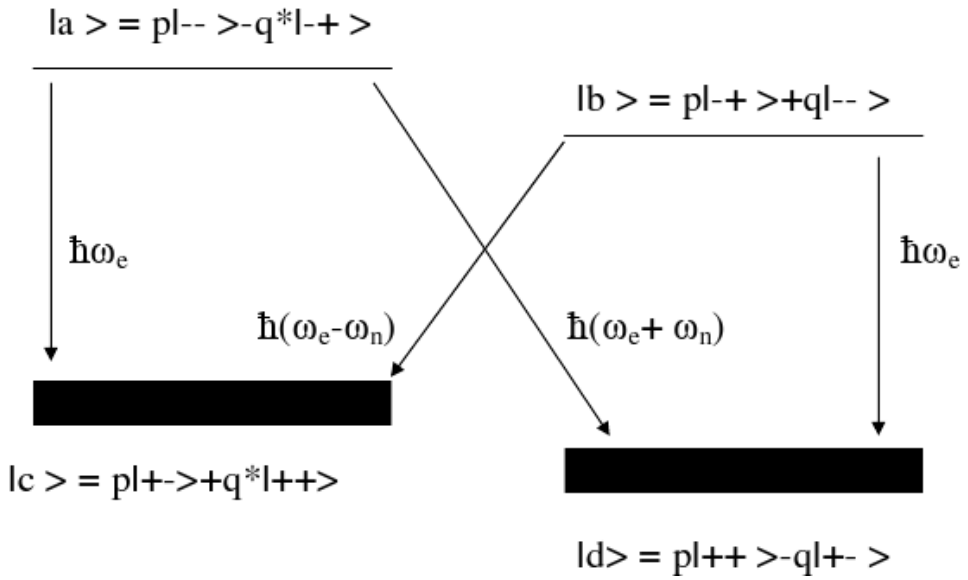

Figure 1.7: *Energy levels of an electron-nuclear pair $|S, I\rangle$ coupled with dipolar interactions. The terms p and q are derived from first order perturbation theory applied to a two spin system for non secular dipolar terms, being $p>>q$.*

The spin diffusion barrier

Those nuclear spins which are too close to the electron spin (closer than the so called spin diffusion barrier b) experience a large magnetic gradient that shifts their nuclear Larmor frequency so they do not contribute to the observed nuclear magnetisation, although they may contribute to the relaxation process [14], [29]. These nuclei that do not contribute to the nuclear resonance line have been considered in a separate Zeeman reservoir, which in some approximation may be in close thermal contact with the electron dipole-dipole interactions[16]. The spin diffusion barrier has been defined as the distance from the electron where the dipolar interaction between electron and nuclei becomes the same magnitude as the nuclear linewidth. Taking into account the non linear behavior of this gradient, the expression to evaluate it is [5]:

$$\Delta\omega_I = \frac{\mu_0}{4\pi}\gamma_I\gamma_S\hbar\frac{1}{b^3}\big(1 - \frac{1}{(1+\frac{a}{b})^3}\big) \tag{1.78}$$

where a is the average distance between the same species of nuclei. The value for b may be calculated by a numerical method. For the case of fast spin diffusion between carbon spins and also strong thermal contact between the electron dipolar bath and the nuclear Zeeman reservoir, the expression for nuclear longitudinal relaxation in a solid doped with paramagnetic impurities is given by 1.79 [5]:

$$\frac{1}{T_{1I}} = (\frac{\mu_0}{4\pi})^2\frac{8\pi}{5}\frac{S(S+1)}{3}\frac{N_S\gamma_I^2\gamma_S^2\hbar^2}{b^3}\frac{T_{2e}}{1+(\omega_I T_{2e})^2}(1-P_0^2) \tag{1.79}$$

where N_S is the concentration of paramagnetic impurities.

1.4.6 Dynamic Nuclear Polarisation at low temperatures

In Dynamic Nuclear Polarisation (DNP) of samples doped with free radicals the higher population levels in unpaired electrons are used to hyperpolarise surrounding nuclei. It was demonstrated in section 1.4.3 with the Provotorov equations that a Zeeman bath and a dipolar bath of the same spin species enter into thermal contact with off resonance irradiation. It was shown also that in a sample doped with paramagnetic centres the nuclei were in contact with the electron secular dipolar bath. By off resonance irradiation on the electron resonance line it is possible to cool the electron secular dipolar bath, and with it, the nuclear Zeeman baths in a DNP process. If this line is homogeneous, then the magnetisation is saturated by the irradiation and the electron dipolar interactions may be considered as a thermal bath. If this line is inhomogeneous, then only some part of the line is saturated so the irradiation burns a hole in the line and the polarisation transfer to nuclei depends on the line gradient seen in that hole. In this (latest) case the electron resonance line must be treated like a large group of electron packets in communication with each other

through cross relaxation, each one of them forming a single electron Zeeman bath [10]. If cross relaxation is faster than spin lattice relaxation, it is possible to consider again a homogeneous line. The process is made more effective at low temperatures (1.5 K) where the electron Boltzmann population reaches more that 90% [3]. Depending on the electron resonance linewidth several polarisation transfer pathways may take place. If the electron linewidth is smaller than the nuclear Larmor frequency then the main DNP mechanism is called the solid effect. If not, then thermal mixing or the cross effect may gain importance over the solid effect [3], [13], [14].

The solid effect

For this project the electron irradiation took place in a non resonant cavity with a maximum power of 200 mW which translated into a low irradiation field B_{1e} condition [5].

Two main approaches have been used to explain the solid effect. Due to non secular dipolar interactions the eigenstates for an electron coupled with a nucleus with spin $\frac{1}{2}$ (the case that will be treated from now onwards) are mixed, therefore zero quantum transitions (ZQ or flip-flops) ($|\omega_S| - |\omega_I|$) and double quantum transitions (DQ or flip-flips) ($|\omega_S| - |\omega_I|$) transitions become allowed (S denotes electron spin and I, nuclear spin) [3], [34]. Under off resonance irradiation on the electrons their transitions are excited, at an appropriate frequency. The main consideration in the solid effect is that due to such a narrow electron resonance bandwidth the DQ transitions are not excited at the same time that ZQ are [3], [14], [34]. For the explanation of this effect it is possible to consider relaxation rate equations for differences in populations in the energy levels, including the transition probabilities for these flip-flops [3], but a thermodynamical description is also possible. This thermodynamical description depends on the interaction between electrons in the electron resonance line.

Following the thermodynamical description by Goldman [14] in the case of

a homogeneous electron resonance line in high field, which is the typical case in the solid effect, the main target is to transform a Hamiltonian that involves one nuclear spin and one electron spin coupled with dipolar interactions $\hat{H}_D$, under RF irradiation at the frequency ω:

$$\hat{H}_0 = \omega_I \hat{I}_Z + \omega_S \hat{S}_Z + \hat{H}_D - 2B_1(\gamma_I \hat{I}_x + \gamma_S \hat{S}_x)cos(\omega t) \tag{1.80}$$

into a Hamiltonian in the rotating frame of the type:

$$\hat{H} = \omega_I \hat{I}_Z + \Delta \hat{S}_Z + \hat{H}'_D + \hat{V} \tag{1.81}$$

where now $\Delta = \omega_S - \omega \sim \omega_I$, $\hat{V}$ involves a non secular dipolar term which is time independent and corresponds either to flip-flops or flip-flips, and $\hat{H}'_D$ refers to the heteronuclear secular dipolar term of the dipolar coupling. Since ω_I is close to Δ and there is a coupling term $\hat{V}$, a cross relaxation between $\hat{I}_Z$ and $\hat{S}_Z$ takes place.

Formally, expression 1.81 corresponds to the case of cross relaxation in the laboratory frame for two spin species with close Larmor frequencies in analogy with equation 1.67. It is necessary to obtain a flip-flop term for the perturbation $\hat{V}$. This may be accomplished with some mathematical transformations. A unitary operator defined as $\hat{U}_1 = 1 - i\hat{R}$, with $\hat{R}$ as a small hermitian operator, is used to transform the previous Hamiltonian. In this way:

$$-i[\hat{R}, (\omega_I \hat{I}_Z + \omega_S \hat{S}_Z)] = \hat{H}''_D \tag{1.82}$$

so $\hat{H}'^*_D = \hat{U}_1 \hat{H}'_D \hat{U}_1^+$ and $\hat{H}_0 = \omega_I \hat{I}^*_Z + \omega_S \hat{S}^*_Z + \hat{H}'^*_D - 2B_1(\gamma_I \hat{I}_x + \gamma_S \hat{S}_x)cos(\omega t)$. It is more convenient to use another representation with a canonical transformation $\hat{H} = \hat{U}_1^+ \hat{H}_0 \hat{U}_1$ so:

$$\begin{aligned}\hat{H}_0 = \omega_I \hat{I}_Z + \omega_S \hat{S}_Z + \hat{H}'_D - 2B_1(\gamma_I \hat{I}_x + \gamma_S \hat{S}_x)cos(\omega t) - \\ - 2B_1 i[\hat{R}, (\gamma_I \hat{I}_x + \gamma_S \hat{S}_x)]cos(\omega t)\end{aligned} \tag{1.83}$$

Those terms which allow for transitions close to either ω_S or ω_I are dis-

regarded (the fourth one). Then, the operator $\hat{R}$ is developed in terms of non secular dipolar Hamiltonian, leaving only those in $\hat{I}_+\hat{S}_Z$, $\hat{I}_Z\hat{S}_+$, $\hat{I}_-\hat{S}_Z$ and $\hat{I}_Z\hat{S}_-$ (which comes from the restriction of the narrow electron resonance line). Further algebra and simplification ($\gamma_S >> \gamma_I$) [14] leads to the perturbation term:

$$\hat{V} \simeq -\frac{1}{2}\frac{B_1\gamma_S}{B_0\gamma_I}\sum_{i,j}(C_{i,j}\hat{I}^i_+S^j_- + C^*_{i,j}\hat{I}^i_-S^j_+) \tag{1.84}$$

in the case of irradiation inducing ZQ transitions or

$$\hat{V}' \simeq -\frac{1}{2}\frac{B_1\gamma_S}{B_0\gamma_I}\sum_{i,j}(C_{i,j}\hat{I}^i_+S^j_+ + C^*_{i,j}\hat{I}^i_-S^j_-) \tag{1.85}$$

in the case of DQ transitions. With a transformation to the rotating frame by the unitary operator $\hat{U}_r = e^{i(\omega\hat{S}_Z t)}$ the final Hamiltonian is $\hat{H} = \omega_I\hat{I}_Z + \Delta\hat{S}_Z + \hat{H}'_D + \hat{V}$ with $\Delta = \omega_s - \omega$. In this way, the nuclear Larmor frequency is close to Δ and cross relaxation happens between $\hat{I}_Z$ and $\hat{S}_Z$.

The density matrix associated with the resulting Hamiltonian in the quasi-equilibrium form can be decomposed in diagonal terms and non diagonal terms and expressed using inverse spin temperatures in the high temperature limit as [14]:

$$\hat{\rho} = 1 - \alpha_I\omega_I\hat{I}_Z - \alpha_S\Delta\hat{S}_Z - \beta\hat{H}'_D + \hat{\rho}_{nonsecular} \tag{1.86}$$

using the modified Provotorov equations for cross relaxation 1.75, 1.76 and 1.77, the differential equations 1.87, 1.88 and 1.89 are obtained. These latter equations would relate the inverse Zeeman temperatures α_I, α_S for the Zeeman nuclear and electron baths respectively and β for the electron dipolar bath [14]. The last terms in 1.87, 1.88 and 1.89 are added afterwards and they include the contribution of spin lattice relaxation.

$$\frac{d\alpha_I}{dt} = \frac{-C_S}{\omega_I} W_{\pm}(\alpha_I\omega_I \pm \alpha_S\Delta - \beta\Gamma) - \frac{1}{T_I}(\alpha_I - \beta_L) \tag{1.87}$$

$$\frac{d\alpha_S}{dt} = \frac{-C_I}{\Delta} W_{\pm}(\alpha_I\omega_I \pm \alpha_S\Delta - \beta\Gamma) - \frac{1}{T_S}(\alpha_S - \alpha_L) \tag{1.88}$$

$$\frac{d\beta}{dt} = \frac{\Gamma}{D^2} W_{\pm}(\alpha_I\omega_I \pm \alpha_S\Delta - \beta\Gamma) - \frac{1}{T_D}(\beta - \beta_L) \tag{1.89}$$

In these equations $\Gamma = \omega_I - \Delta = \omega_I - \omega_S + \omega$, $C_I = \frac{N_I}{N_I+N_S}$, $C_S = \frac{N_S}{N_I+N_S}$ (N_I and N_S are the number of spins I and S), $D^2 = \frac{Tr(\dot{H'_D})}{N_I N_S(Tr(\hat{I}^2)+Tr(\hat{S}^2))}$ is the local frequency and the probability $W_{\pm}$ can be approximated as a Gaussian lineshape (the index + in W_+ denotes the ZQ and -, DQ transitions). The relaxation times for nuclear Zeeman, electron Zeeman and the dipole thermal bath are T_I, T_S and T_D respectively. The pattern of enhancement obtained depending on irradiation frequency can be obtained by equalising to zero the expressions 1.87, 1.88 and 1.89 (in the quasi-equilibrium state); and representing then in figure 1.8.

The mixing between the electron dipolar reservoir and the nuclear Zeeman reservoir lead to a positive or negative enhancement depending on the electron irradiation frequency. In figure 1.8 a simulation shows the enhancement obtained from a sample of protons doped with a 18.5 MHz linewidth paramagnetic centre in a field of 3.35 T.

Thermal mixing

When the electron resonance linewidth is broader than the nuclear Larmor frequency other polarisation transfer mechanisms take place, such as Thermal Mixing (TM) or the Cross Effect (CE), when the energy required for a flip-flop between two electron spins is equal to the energy required to flip a nuclear spin with the magnetic field [10]. Two cases can be considered. If the line is homogeneous then it is possible to assume a spin temperature for the electronic secular dipolar reservoir in the laboratory frame and high field [3]. When

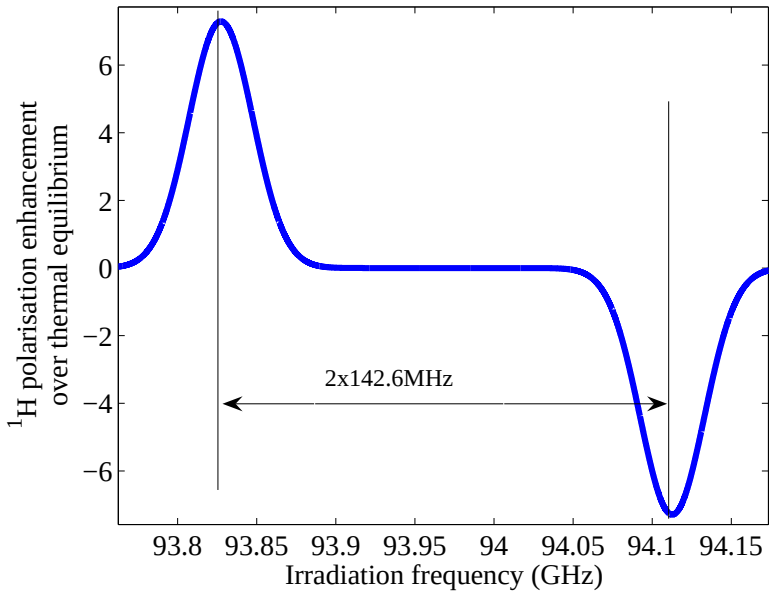

Figure 1.8: *Solid state enhancement versus EPR irradiation simulation for a system of proton spins doped with 0.015 mM pf paramagnetic centres that exhibit a electron resonance Gaussian shaped with a linewidth of 18.5 MHz in a magnetic field of 3.35 T (the frequency D was set to this value also). C_I and C_S were set to 1 and 0.002 respectively. The relaxation times T_I, T_S and T_D were set to 3720, 1 and 0.01 s respectively. Both peaks are antisymmetric and placed at a frequency of $\omega_e \pm \omega_I$, so the distance between them is $2 \times \omega_I$.*

applying a RF field a single spin temperature of this dipolar reservoir in the rotating frame may be assumed, which would create thermal contact between the electronic Zeeman and the dipolar baths, cooling the latter one. In the other case where the line is non homogeneous due to g-anisotropy and hyperfine interactions, and cross relaxation between electron spin packets is faster than spin lattice, the cross effect (CE) plays an important role [13]. In any case TM and CE rely on a three spin process when two spins flip so the energy gap corresponds to the Larmor frequency of a nuclear spin that flips with them. In the particular case of a broad electron line with fast spectral diffusion the process for DNP becomes more complex since several interactions must be

taken into account: TM, SE, relaxation due to non secular terms in the $\hat{H}_{IS}$ dipolar reservoir with probability U and the evolution to a common value of the inverse spin temperatures α_S and β. The differential equations presented by Goldman [14] are:

$$\frac{d\alpha_I}{dt} = -[C_S(W_+ + W_-) + U + \frac{1}{T_I}]\alpha_I + C_S\frac{\Delta}{\omega_I}(W_+ - W_-)(\alpha_S - \beta) + \\ + [C_S(W_+ + W_-) + U]\beta + \frac{1}{T_I}\beta_L \tag{1.90}$$

$$\frac{d\alpha_S}{dt} = -W_0(\alpha_S - \beta) - \frac{1}{T_S}(\alpha_S - \beta_L\frac{\omega_S}{\Delta}) \tag{1.91}$$

$$\frac{d\beta}{dt} = W_0\frac{\Delta^2}{C_I D^2}(\alpha_S - \beta) - \frac{1}{T_D}(\beta - \beta_L) \tag{1.92}$$

where in this case the probability distribution for W_+ or W_- are bell shaped curves and far smaller than W_0 that corresponds to allowed transitions. The last term added at the end of each equation refers to the spin lattice of the respective thermal reservoir. By equalising the previous equations 1.90, 1.91 and 1.92 to zero and solving for the nuclear inverse spin temperature the expression for polarisation in equilibrium is obtained. The characteristic pattern is anti-symmetric, with two peaks at a difference of frequencies equivalent to the electron resonance line bandwidth.

The interaction between two electron spins and a nuclear spin so that $|\omega_{1S} - \omega_{2S}| = \omega_I$ is made possible by tethering two free radicals together so the average distance between both free electrons produces an electron g-anisotropy interaction of the order of the nuclear frequency [31].

By setting the derivatives in equations of the unresolved solid effect from the model by Goldman to zero and solving for the three inverse spin temperatures the DNP enhancement spectrum can be obtained. An example is given in figure 1.9. In this spin temperature model the linear approximation for the density matrix must be valid, so for very low temperatures (of the order of millikelvins) it only gives a qualitative description.

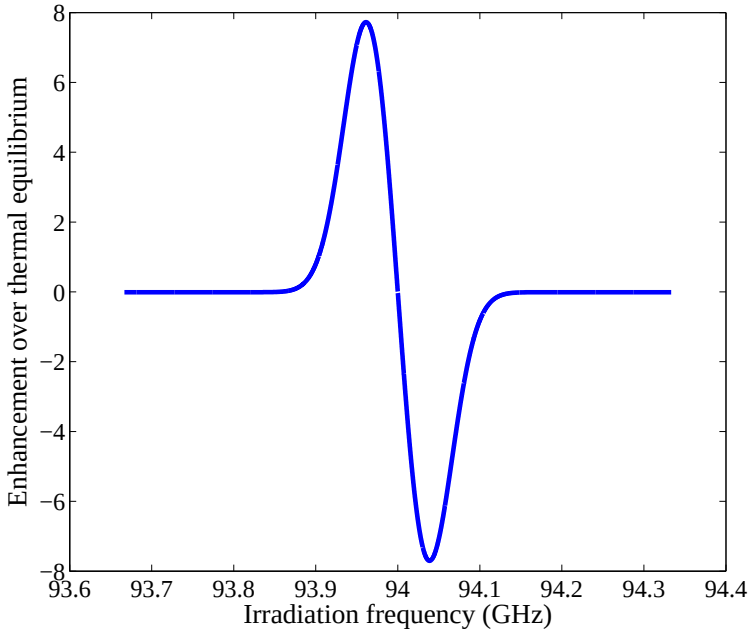

Figure 1.9: *DNP enhancement spectrum for thermal mixing in a sample doped with paramagnetic centres. C_S and C_I were 0.015 and 1 respectively. The relaxation times T_I, T_S and T_D were set to 10000, 1 and 0.1 respectively. The probabilities W and U had a maximum value of 0.002 and 0.01 s^{-1}. W had a Gaussian lineshape with 30 MHz linewidth (D was also set to 30 MHz). The NMR frequency corresponded to the Larmor frequency of ^{13}C in a 3.35 T magnet.*

Dynamic Cooling

Dynamic cooling has been presented as a form of DNP where the interactions between electrons must be taken into account for a correct description of the DNP process. The electron dipolar-dipolar reservoir cools the nuclear Zeeman bath whilst being cooled itself by the electron Zeeman reservoir [6]. The mathematical expressions to include this concept need the inclusion of a differential equation for the variation of inverse spin temperature for the electron dipolar reservoir.

1.5 Description of Hardware: polariser, 9.4 T magnet and the new dual centre magnet

The main target of hyperpolarisation techniques in this project was the dissolution experiment. In this experiment it was demonstrated that little spin order was lost when the sample was dissolved and passed to another magnet in a time that is short in comparison with the T_1 of the spin species at a higher temperature [4].

A brief description of the magnets used in this project is provided to illustrate the experiments: a standard Bruker 9.4 T, used with a high resolution double resonance probe for a 5 mm glass sample tube was used for making NMR measurements, and the home built stand-alone polariser employed a 3.35 T magnet supplied by Oxford Instruments (OI, Abingdon) [4] (figure 1.10,2). The polariser has a cylindrical cavity at the end of the variable temperature insert (VTI). This VTI is inserted into the polariser. The central hole has a 15 mm diameter making it possible to load the sample into the microwave cavity (figure 1.10,3) using a PTFE tube. A sample in a sample cup is placed at the bottom of the PTFE tube, which is kept at the centre of the cavity, where the lowest temperatures of 1.5 K can be achieved (figure 1.10, 3)(figure 1.11). A waveguide into the polariser parallel to the VTI guides the microwave irradiation to the sample.

The dissolution experiment was performed with a dissolution device. It was comprised of a pressure cooker for boiling the solvent and PTFE capillaries contained in a stainless steel tube. These two tubes were used to guide the solvent from the pressure cooker to the sample cup in the polariser. The dissolved sample passed within one of the tubes to a 5 mm tube inside the 9.4 T magnet using helium gas for pneumatic shuttling. Any solid state NMR probe built during this project was designed to fit into the VTI inner space. Changes to the dissolution device along with the description of two probes for DNP, cross polarisation (CP) and dissolution experiments will be described in

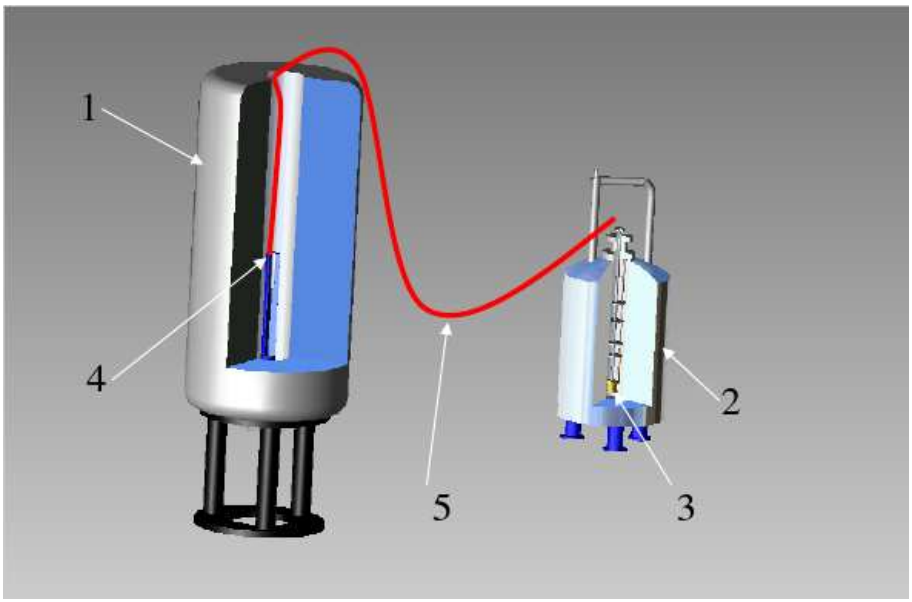

Figure 1.10: *A Bruker 9.4 T magnet (1) with an Oxford Instruments stand alone polariser (2). In solid state experiments the sample was kept at temperatures close to 1.5 K (3). In dissolution experiments the sample was dissolved and passed to the high resolution probe (4) in the 9.4 T Bruker magnet with PTFE tubes (5).*

following chapters.

The dissolution process and transfer between polariser and high field magnet took several seconds. Therefore a new system was designed, combining a 3.35 T polariser and a high resolution 9.4 T magnet in a dual centre magnet, as shown in figure 1.12. In this case the sample was polarised in the top magnet at 3.35 T. The cryostat took several hours to cool down to 1.4 K. The sample was fitted at the end of the irradiation cavity which in this case was attached to a corrugated waveguide of 2 meters long. A 7 mm diameter NMR saddle coil was attached to the irradiation cavity. This saddle coil was made double resonant for ^{1}H and ^{13}C. The 2 mm diameter semirigid cables used were placed in parallel to the waveguide. For the dissolution process, the waveguide descended automatically until it made contact with a specially designed dissolution dock. The dissolved sample was injected into the 5 mm NMR sample tube, in an overall time of less than 0.8 s.

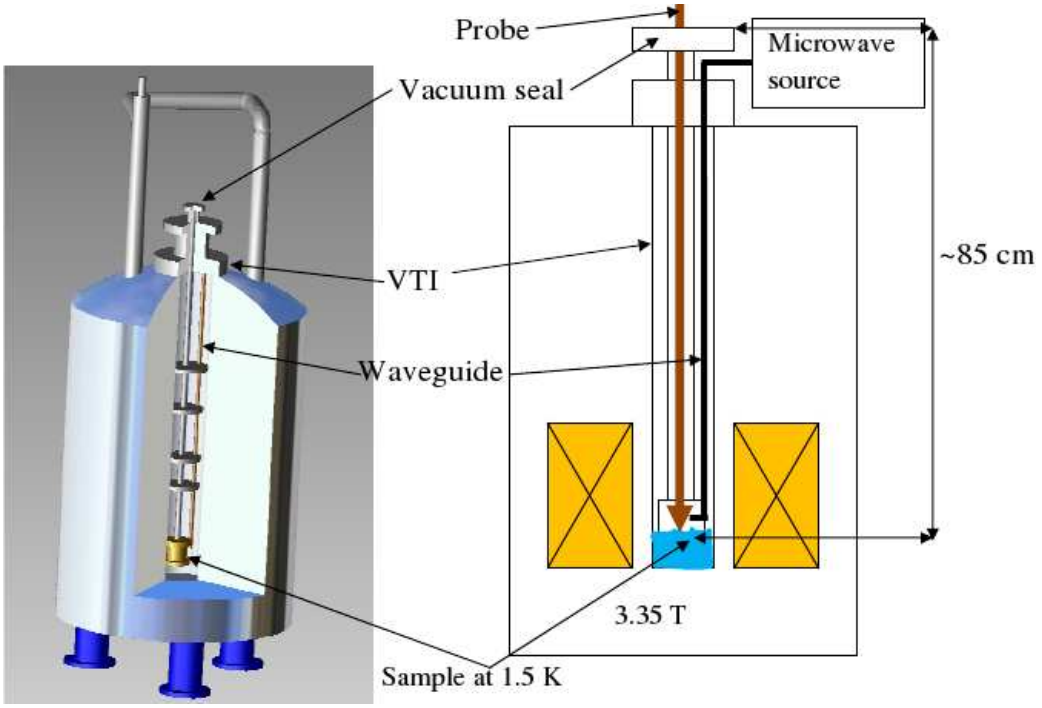

Figure 1.11: *Closer view of the stand alone polariser. A scheme on the right illustrates that the waveguide is parallel to the VTI. It leads the irradiation from the microwave source (Elva source, Saint Petersburg, Russia) to the microwave cavity, where the minimum temperatures are reached. The bottom of the variable transfer insert (VTI) reaches temperatures as low as 1.5 K and the top is at room temperature. A picture on the left shows a 3-D scheme of the SAP.*

1.6 Other techniques of DNP and applications

Hyperpolarisation techniques have been used for elementary particle scattering [6]. Studies of biological metabolic compounds in the solid state have been presented by a group at MIT [7], [24]. By dissolving a sample doped with free radicals after DNP at low temperatures and passing it to a higher magnetic field enhancement over 10000 times in SNR has been obtained [4]. This makes possible in liquid state the study of very low concentration molecules with low gyromagnetic ratios like ^{13}C and ^{15}N. Also, it enables studies of metabolism in vivo by injecting a hyperpolarised sample into animal and humans [32] and ^{13}C imaging [20].

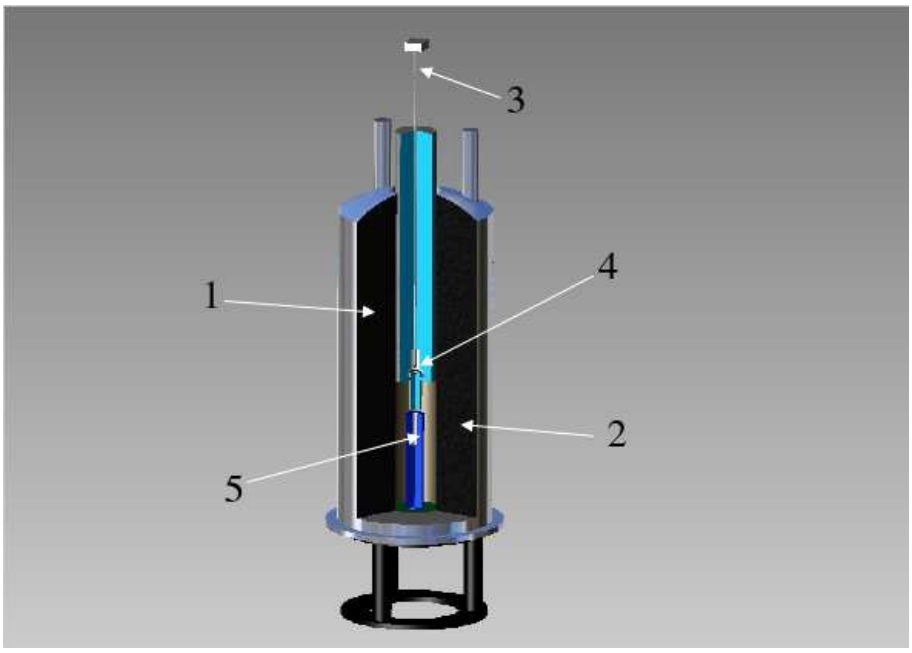

Figure 1.12: *In the new device the 3.35 T magnet (1) is above the 9.4 T (2) magnet. A 2 m long corrugated waveguide (3) leads the irradiation to the sample at 1.5 K (4). A solid state NMR probe was fixed in parallel to the waveguide. The coil surrounded the sample holder. At the moment of dissolution the waveguide dropped a few centimeters until it reached the dissolution dock. The dissolved sample then descends by gravity to less than a second into the high resolution probe (5).*

Another DNP mechanism is the Overhauser effect (OE), which can be used to transfer electron magnetisation to nuclei at room temperature. A technique that uses the OE is field cycled proton electron double resonance imaging (FC-PEDRI) for imaging and also for spectroscopy purposes, in vivo and in vitro. In this technique the magnetic field is cycled so the main magnetic field is lowered for electron resonance DNP irradiation (at frequencies as low as 120 MHz) and set to 59 [22] or 450 mT [23] for proton signal acquisition. This is a powerful technique for free radical imaging in samples and small animals, although the gain in SNR is far less than the one obtained with dissolution experiments after DNP on samples at low temperature. With a maximum absolute enhancement of 660 for OE, it is possible to average and increase the SNR. One disadvantage of DNP is the level of radiofrequency irradiation,

which is necessary for polarisation and heats the sample. With this technique it is possible to measure parameters such as pH or drug delivery in animals [23], [28].

Other techniques have been used to hyperpolarise nuclei apart from Dynamic Nuclear Polarisation. Optical pumping uses laser light as a way to excite nuclear transitions [25]. After hydrogenation with parahydrogen it is possible to transfer the spin order to nearby ^{13}C nuclei with some field manipulations. In this way it is possible to achieve hyperpolarised samples to be used for *in vitro* or *in vivo* imaging [17].

Bibliography

[1] A. Abragam. *The Principles of Nuclear Magnetism*. Oxford at the Clarendon Press, 1961.

[2] A. Abragam and B. Bleaney. *Electron Paramagnetic Resonance of Transition Ions*. Oxford University Press, London, 1970.

[3] A. Abragam and M. Goldman. Principles of dynamic nuclear polarisation. *Rep. Prog. Phys.*, 41, 1978.

[4] J. H. Ardenkjaer-Larsen, B. Fridlund, A. Gram, G. Hansson, L. Hansson, M. H. Lerche, R. Servin, M. Thaning, and K. Golman. Increase in signal-to-noise ratio of $>$ 10000 times in liquid-state NMR. *Proc. Nat. Acad. Sci. US*, 100:18, 2003.

[5] J. H. Ardenkjaer-Larsen, S. Macholl, and H. Johannesson. Dynamic nuclear polarisation with trityls at 1.2 K. *Appl. Magn. Reson.*, 34:509–522, 2008.

[6] V. A. Atsarkin. Dynamic polarization of nuclei in solid dielectrics. *Usp. Fiz. Nauk*, 126:3–39, 1978.

[7] Vikram Singh Bajaj. *Dynamic Nuclear Polarization in Biomolecular Solid State NMR: Methods and Applications in Peptides and Membrane Proteins*. PhD thesis, Massachustts Institute of Technology, 2007.

[8] M. A. Bernstein, K. F. King, and X. J. Zhou. *Handbook of MRI Pulse Sequences*. Elsevier academic press (Oxford), 2004.

[9] N. Bloemberger. On the interaction of nuclear spins in a crystalline lattice. *Physica*, XV:3–4, 1949.

[10] C. T. Farrar, D. A. Hall, G. J. Gerfen, S. J. Inati, and R. G. Griffin. Mechanism of dynamic nuclear polarization in high magnetic fields. *J. Chem. Phys.*, 114:11, 2001.

[11] E. Fukushima and S. B.W. Roeder. *Experimental pulse NMR: A Nuts and Bolts Approach.* Perseus Books Publishing Cambridge, Massachusetts, 1981.

[12] B.C. Gerstein and C. R. Dybowski. *Transient Techniques in NMR of Solids: An Introduction to Theory and Practice.* Academic Press, Inc (London), 1985.

[13] S. T. Goertz. The dynamic nuclear polarization process. *Nuc. Instr. Met. Phys. Res. A*, 526:28–42, 2004.

[14] M. Goldman. *Spin Temperature and nuclear magnetic resonance in solids.* Oxford at the Clarendon Press (London), 1970.

[15] M. Goldman. Overview of spin temperature, thermal mixing and dynamic nuclear polarisation. *Appl. Magn. Reson.*, 34:219–226, 2008.

[16] M. Goldman, S. F. J. Cox, and V. Bouffard. Coupling between nuclear Zeeman and electronic spin-spin interactiosn in dielectric solids. *J. Phys. C. Solid State Phys.*, 7, 1974.

[17] M. Goldman, H. Johannesson, O. Axelsson, and M. Karlsson. Hyperpolarization of ^{13}C through order transfer from parahydrogen: A new contrast agent for MRI. *Mag. Res. Imag.*, 23:153–157, 2005.

[18] R. Kimmich. *NMR Tomography diffusometry relaxometry.* Springer-Verlag Berlin Heilderberg, 1997.

[19] E. Kupce and R. Freeman. Optimized adiabatic pulses for wideband spin inversion. *J. Mag. Res. A*, 118:299–303, 1996.

[20] P. E. Z. Larson, A. B. Kerr, A. P. Chen, M. S. Lusting, M. L. Zierhut, S. Hu, C. H. Cunningham, J. M. Pauly, J. Kurhanewicz, and D. B. Vigneron. Multiband excitation pulses for hyperpolarized ^{13}C dynamic chemical shift imaging. *J. Mag. Res.*, 194:121–127, 2008.

[21] Malcolm H. Levitt. *Spin dynamics: basics of Nuclear Magnetic Resonance*. John Wiley and Sons, Chichester, West Sussex, 2001.

[22] D. J. Lurie, M. A. Foster, D. Yeungy, and J. M. S. Hutchison. Design, construction and use of a large-sample field-cycled PEDRI imager. *Phys. Med. Biol. 43 (1998) 18771886.*, 43:18771886., 1998.

[23] D. J. Lurie and K. Mader. Monitoring drug delivery processes by EPR and related techniques-principles and applications. *Adv. Dru. Del. Rev.*, 57:1171–90, 2005.

[24] T. Maly, G. T. Debelouchina, V. S. Bajaj, K. N. Hu, C. G. Joo ANDM. L. Mak-Jurkauskas, J. R. Sirigiri, P. C. A. van del Wel, J. Herzfeld, R. J. Temkin, and R. Griffin. Dynamic nuclear polarisation at high magnetic fields. *J. Chem. Phys.*, 128:052211, 2008.

[25] H. H. McAdams. Dynamic nuclear polarization of liquid helium three by optical pumping. *Phys. Rev.*, 170:1, 1968.

[26] Ildefonso Marin Montesinos. *New Recoupling Techniques in Solid-State NMR*. PhD thesis, University of Southampton, 2007.

[27] George E. Pake. *Paramagnetic Resonance*. W. A. Benjamin, Inc., Publishers (New York), 1962.

[28] D. I. Potapenkoa, M. A. Foster, D. J. Lurieb, I. A. Kirilyukc, J. M.S. Hutchison, I. A. Grigorevc, E. G. Bagryanskayaa, and V. V. Khramtsov.

Real-time monitoring of drug-induced changes in the stomach acidity of living rats using improved ph-sensitive nitroxides and low-field EPR techniques. *J. Mag. Res.*, 182:1–11, 2006.

[29] C. Ramanathan. Dynamic nuclear polarization and spin diffusion in nonconducting solids. *Appl. Magn. Reson.*, 34:409–421, 2008.

[30] D.N. Rutledge. *Signal treatment and signal analysis in NMR.* Elsevier (Amsterdan), 1996.

[31] C. Song, K.Hu, C. Joo, T. Swager, and R.G. Griffin. Totapol: a biradical polarizing agent for dynamic nuclear polarization experiments in aqueous media. *J. Amer. Chem. Soc.*, 128:11385–11390, 2006.

[32] D. M. Spielman, D. Mayer, Y-F. Yen, J. Tropp, R. E. Hurd, and A. Pfefferbaum. In vivo measurement of ethanol metabolism in the rat liver using magnetic resonance spectroscopy of hyperpolarized [1-^{13}C] pyruvate. *Mag. Res. Med.*, 62:307–313, 2009.

[33] J. D. Walls and Y-Y Lin. Constants of motion in NMR spectroscopy. *Sol. Stat. Nuc. Mag. Res.*, 29:22–29, 2006.

[34] W. T. Wenckebach. The solid effect. *Appl. Magn. Reson.*, 34:227–235, 2008.

[35] D. Wolf. *Spin temperature and nuclear spin relaxation in matter: basic principles and applications.* Oxford University Press (Oxford), 1979.

Chapter 2

Hardware

This chapter provides a summary of the hardware components that have been designed, built and used to carry out nuclear magnetic resonance (NMR), dynamic nuclear polarisation (DNP) and Cross Polarisation (CP) experiments in solid state at a temperature of 1.5 K and a field strength of 3.35 T. The chapter is divided in two main sections. The first section deals with the analogue electronic parts and concepts used to build the probes. In the second section several probes are described. All of them were built on the bench and tested at 3.35 T and 1.5 K unless indicated. The purpose of this section is to summarise the performance of the radiofrequency (RF) probes used in this project.

2.1 RF circuit components

2.1.1 Biot and Savart Law

A moving electric charge produces a magnetic field according to formula 2.1 [20]:

$$\mathrm{d}\vec{B} = \frac{\mu_0}{4\pi}\frac{I\mathrm{d}\vec{l}\times\vec{r}}{r^2} \tag{2.1}$$

where the electric charge is $I\mathrm{d}\vec{l}$ and the magnetic permeability of free space $\mu_0 = 4\pi 10^{-7}$ Hm^{-1}. The magnetic field decreases with the square of the

distance and is perpendicular to the current element $d\vec{l}$. It is measured in Tesla in the International System (SI). In magnetic resonance the spins are excited by an RF magnetic field perpendicular to the main magnetic field.

2.1.2 Magnetic flux and Lenz-Faraday law

The magnetic flux Φ_m refers to the RF magnetic field per area unit [20]:

$$\Phi_m = \vec{B}\vec{A} = BA\cos(\Theta) \tag{2.2}$$

where $\vec{B}$ is the magnetic field and $\vec{A}$ is the area. The magnetic flux is measured in Webers (Wb) in SI units. According to the law of Lenz-Faraday a change of magnetic flux Φ_m inside a wire loop (in a receiver coil, for instance) will produce a voltage ξ at the two terminals of this loop: $\xi = -\frac{\mathrm{d}}{\mathrm{d}t}\Phi_m$. Following the principle of reciprocity a good transmitter coil acts also as a good receiver [11], [20].

2.1.3 Inductor

The inductance L in a circuit relates the current I in this circuit with the magnetic flux Φ_m, according to formula 2.3:

$$\Phi_m = LI \tag{2.3}$$

The inductance depends on the geometry of the circuit. The inductance is measured in Henries (H) in SI units. It is usually difficult to obtain an analytical expression for the inductance [20], but for simple cases it is possible. For a solenoid with a pitch that equals the diameter of the wire the inductance L is: $L = \dfrac{\Phi_m}{I} = \mu_0 n^2 Al$, where n is the number of turns per unit length and Al is the volume (with A the cross section and l the length) [20]. For complicated shapes like shimming coils it is more practical to run numerical simulations instead of finding analytical formulae, although the most direct method is to

measure it experimentally.

The inductance of a conductor depends also on the proximity of other conductors. If two circuits are too close, the current of the first circuit I_1 will change the magnetic flux in the second Φ_2 [20]:

$$\Phi_2 = L_2 I_2 + M_{12} I_1$$

where M_{12} is the mutual inductance and L_2 and I_2 are the inductance and current in the second circuit respectively.

The skin effect

The skin effect predicts that a radiofrequency current uses only that part of the section of the conductor which is closer to the surface. The skin depth is defined as a characteristic depth from the conductor surface where the current drops to $\frac{1}{e}$ of its surface value [20]. A mathematical expression for the skin depth λ_{Sdepth} is:

$$\lambda_{Sdepth} = \sqrt{\frac{2\rho}{\omega\mu}}$$

An approach to increase the Q factor of a coil is reducing the width of the conductor so the full cross section is being used by the electric current [8]. However, in this project the coils were used at low temperatures at which the skin depth is very small (micrometres or smaller), so this type of method was impractical. The main method to obtain a high Q factor for the coil was by increasing the number of turns and by lowering the temperature. In this work only normal copper wire and silver plated copper wire were used to build the coils. At room temperature for copper (electrical resistivity of $1.75 \bullet 10^{-8}\ \Omega/m$) and 0.1 MHz, the skin depth amounts to 0.2 mm. At lower temperatures and higher frequencies the resistivity may decrease by a few orders of magnitude.

Resistance and impedance presented by an inductor

An inductor made of wire of diameter d and resistivity ρ at a frequency ω has a resistance per length R according to the following formula [20]:

$$R = \frac{1}{\pi d}\sqrt{\frac{\omega\rho\mu}{2}}$$

where μ is the magnetic permeability of the wire. The resistivity ρ depends on the temperature. The impedance Z of an inductor at the frequency ω is [20]:

$$Z = R + \mathrm{i}\omega L \tag{2.4}$$

and it is measured in ohms (Ω) in SI units ($\mathrm{i}=\sqrt{-1}$). For example, the measured value for a saddle coil inductor with 8 mm length and 4.5 mm inner diameter (ID), made of 0.4 mm diameter silver plated wire, was 1.3 + 45.4i Ω with an inductance of 50.1 nH for 142.6 MHz and 0.30+10i Ω with an inductance of 45 nH for 36 MHz. The inductor may be represented by a parasitic model shown in figure 2.1:

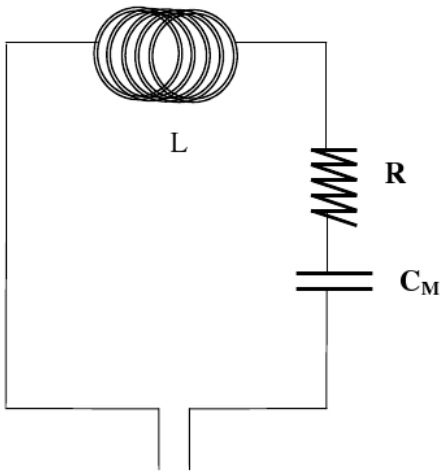

Figure 2.1: *A series RLC circuit. The capacitance C_M is in parallel with the inductor L and a resistance R. When the reactance is zero, the circuit is said to be resonating. It corresponds also to the parasitic model of a real inductor. The capacitance C_M corresponds to the stray capacitance presented by the same inductor. In resonant conditions the inductor is said to be self-resonant.*

An inductor becomes self-resonant when the imaginary part of the complex impedance in the circuit vanishes. This happens at a certain frequency. In most cases in solid state NMR the working frequency must be lower than this self-resonant frequency [17].

The Q factor

The Q factor of the coil can be defined as $Q = \frac{\omega L}{R}$. It yields information of the performance and losses in a coil. A high Q factor implies low losses, whereas a low Q factor implies a large resistance.

2.1.4 RF coil geometry

There are several kinds of inductors, but in the present study mainly the solenoid coil and the saddle coil were considered. Some attempts with the Helmholtz coil yielded, if not important results in this thesis, at least some alternatives.

The solenoid

The B_1 field generated by the solenoid coil (figure 2.2, left) was estimated in changing axially by less than 10% in the middle third of the volume enclosed [9]. The radial homogeneity can be improved by leaving a small space between two wire loops (for example, a pitch of the diameter of the wire). Using flat ribbon further improves the radial homogeneity. An optimised NMR solenoid design was presented by Privalov et al [15] that increased the number of turns at the extremes of the solenoid. In DNP experiments it was necessary to allow microwaves coming from a waveguide to reach the sample, so the spacing between the turns had to be equal to the wavelength (at a magnetic field of 3.35 T it becomes $\lambda \sim 3$ mm). In this work normal and flattened wire spaced by the same distance as the wire section diameter or maximum diameter was used.

Figure 2.2: *A solenoid coil (left), a saddle coil (middle) and a Helmholtz coil (right). The three of them yield a homogeneous magnetic field in the center with a direction represented by an arrow.*

The saddle coil

A saddle coil (figure 2.2, middle) can be considered as two square loops crushed against a cylindrical former in such a way that the currents in the loops flow in the same direction. Therefore, the magnetic field is transverse to the axial axis of the metallic structure. The coil allowed radiation through the wings and access to the sample region from above and below. The saddle coil was chosen for these reasons for DNP and dissolution experiments.

There are several kind of saddle coils [11], [18]. The optimal design predicts best B_1 homogeneity in the center when the four parallel wires that make up the structure are spaced 60-120-60-120 degrees, and the length of the coil is twice the internal diameter [11]. Other models of saddle coils have more turns per wing or a different set of angles for the parallel wires [18]. Another version designed by [12] demonstrated a higher Q factor by using thin copper foil instead of wires. In this work normal copper wire of 0.150 mm, 0.300 mm and silver plated copper wire of 0.600 mm were used as a good compromise of stability and flexibility in bending the wires.

The Helmholtz coil

The Helmholtz coil has two wings separated by a gap with the width equal to the radius [20]. The magnetic field is aligned with the axial axis (figure 2.2, right). For DNP it was an alternative since it allowed irradiation of mi-

crowaves through this space where the sample was allocated. However, for the dimensions of the sample and wire used for the wings, some part of the sample was shielded from the microwaves with just two or three turns per wing in the coil. The Helmholtz coil was only used in quadrature with a solenoid in a test double resonance probe.

2.1.5 The filling factor

For the RF coils it was crucial to increase the magnetic flux in the sample, in particular in pulsed solid state where large B_1 fields are required. To obtain strong B_1 fields, a strategy was to reduce the size of the coil itself. Another strategy for a given sample volume was to reduce the volume of the inductor surrounding the sample. The filling factor relates the magnetic field in the sample with the magnetic field within the coil. The signal-to-noise ratio (SNR) is directly proportional to the filling factor. The filling factor η [8] can be calculated using formula 2.5:

$$\eta = \frac{\int_{Sample} B_1^2 \mathrm{d}V}{\int_{Coil-volume} B_1^2 \mathrm{d}V} \tag{2.5}$$

Rigid wire was used whenever it was possible. Otherwise a coil former was needed. The coil former then had to be as thin as possible to minimise the distance between sample and coil. In this work thin wire (of either 0.150 or 0.300 mm) was bent on coil formers of several probes. Macor and PTFE were the best choices as proton free materials. A typical distance between 0.25 mm and 0.5 mm was left between coil and sample cup with an appropriate coil former.

2.1.6 Capacitors

A capacitor stores energy as electric charge [20]. A typical example consists of two parallel conductors separated by a dielectric. If between both conductors a voltage V is applied, a charge Q_C is stored. The capacity relates Q_C and

V: $C = \frac{Q_C}{V}$ and it is measured in Farads in SI units. $C = \frac{\epsilon_0 A}{s}$ with ϵ_0 the dielectric constant, s the distance between the conductors and A the plate area. A capacitor can be modelled as a capacitance with a resistance in series [22]. Since it is composed of two conductors a parasitic inductance is present, which becomes more relevant at higher frequencies. A more complete model may be represented in figure 2.3. There are several criteria that determine the choice

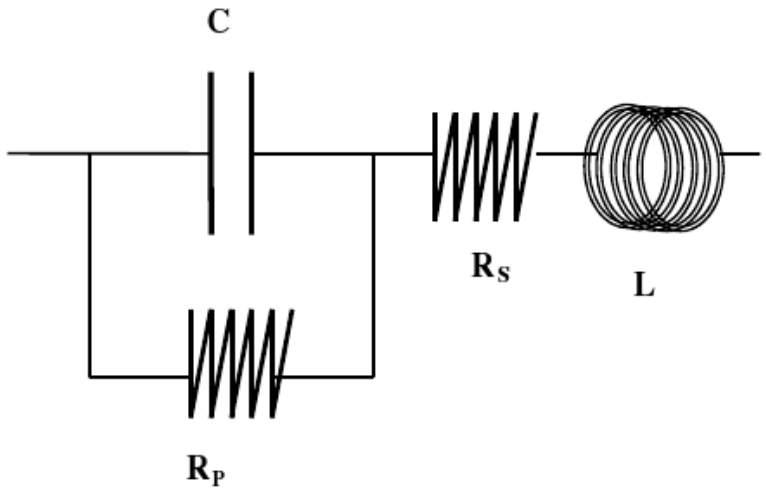

Figure 2.3: *The metallic plates of a chip capacitor present an inductance in series with the capacitance itself.*

of a capacitor for solid state NMR experiments. An obvious one is whether it is magnetic or not. The chosen dielectric plays a role since it is necessary to have a high breakdown voltage. But probably more important is the thickness of the dielectric in the capacitor, or in other words, the conductors of both sides of the capacitor should be as far away as possible from each other. It is also important that the intrinsic resistance of the capacitor is low. This resistance is described by the coefficient called tangent of losses (tanδ). The Q factor of a capacitor is $Q = \frac{1}{tan\delta}$. Some typical dielectric values are presented in table 2.1:

In this project non-magnetic ceramic american technical ceramics (ATC)

Dielectric	tan δ	dielectric constant
PTFE	0.0002	2.0-2.2
Kel-F	0.001	2.5
PEK	0.003	3.4
Epoxy	0.03	3.6
$SrTiO_3$	0.002	330
$BaTiO_3$	0.03	1200
NPO	0.002	30
ATC100	0.00007	15
Kapton	0.0015	3.1
Sapphire	0.0002	9.9

Table 2.1: Tangent of losses and dielectric constant for several capacitors [6].

chip capacitors showed acceptable performance under liquid Helium conditions. However, since they were not specified for temperatures of 1.5 K, it was expected that the capacitor would break at some point.

A possibility is the use of non-magnetic trimmer capacitors for cryogenic environments. They are offered by several companies. At the time of writing Voltronics offers a wide range of non magnetic trimmer capacitors suitable for cryogenic environments. The dielectric material includes PTFE, glass and sapphire. To obtain the right tuning range it was necessary at some point to connect a trimmer capacitor with a chip capacitor in parallel in liquid helium. The capacitor shaft was rotated remotely with a rod.

The importance of the thickness of the dielectric can be appreciated in table 2.2 with some typical values.

Thickness in mm	V for $\epsilon < 30$ (V)	V for $\epsilon < 10$(V)
0.1	500	1000
0.5	1200	2200
3.0	3000	5400

Table 2.2: Typical values for breakdown voltages in capacitors.

For more details it may be useful to see [6] and [22].

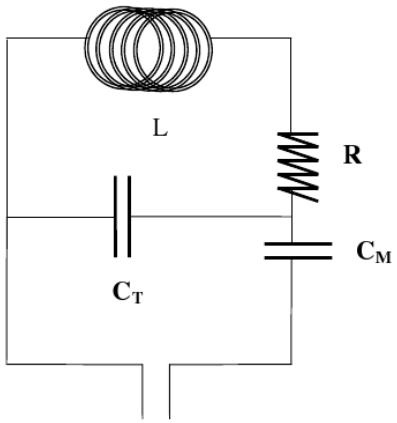

Figure 2.4: *An inductor L in parallel with a capacitor C_T for tuning. It is matched with another capacitor C_M*

2.1.7 Resonant circuits

Two main kinds of resonant circuits were used for this thesis. The series resonant coil corresponds to figure 2.1. The series capacitor removes the reactance in the circuit, leaving usually a small resistance. This circuit has been used for remote tuning. The second type of resonant circuit has the capacitance C_T parallel to the RF coil.

The signal voltage is increased by the Q factor of the coil and the noise voltage would also be increased by the same factor [4]. To tune and match the tuning capacitor resonates the coil impedance, increasing the real and imaginary impedance (figure 2.5). The remaining reactance is removed with the matching capacitor in series C_M in figure 2.4. The real part of the final impedance should match the preamplifier output impedance. The advantage of having a resonant circuit of this kind lies in the increased B_1 field which is necessary for pulsed experiments in solid state NMR. To obtain high B_1 fields it is necessary to use high Q components to maximise the power that arrives and dissipates in the coil.

Better performance can be generated with balanced matching schemes (one matching capacitor at each side of the tuning capacitor instead of a single one

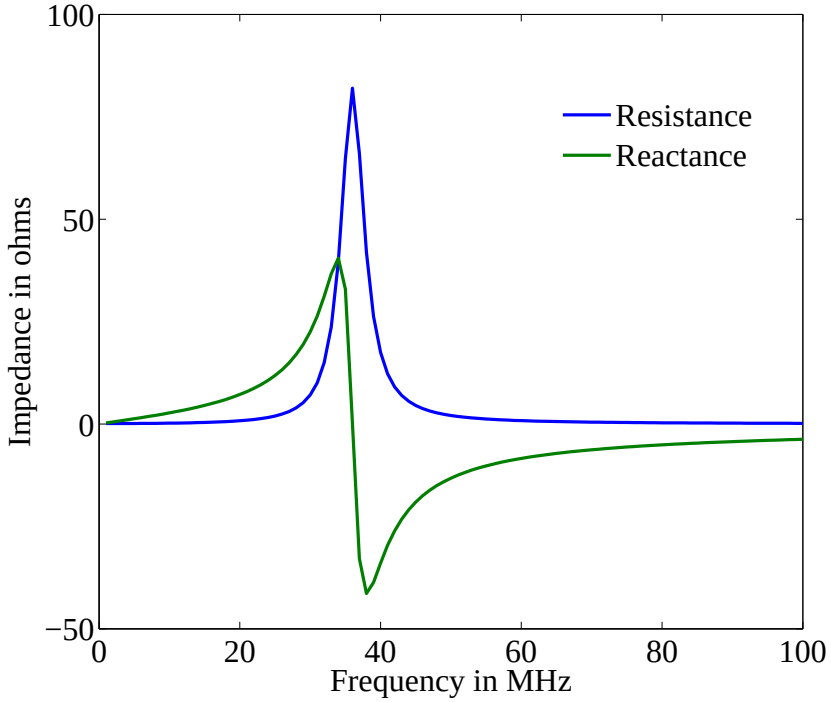

Figure 2.5: *Resistance and reactance of a capacitor of 488 pF that resonates a parallel inductor of 40 nF with a resistance of 0.1 Ω at 36 MHz. With the right tuning the impedance would be equal to 50 Ω some positive reactance. A matching capacitor would remove this reactance.*

as in figure 2.4), but in this project it was not considered necessary.

2.1.8 Ring-down times and resistors

A large Q factor in a resonant circuit may not be desirable since the presence of transient effects or ring-down may hide the free induction decay (FID) or part of it [10]. One option to decrease the necessary deadtime to avoid these transient effects is to place a resistor in series with the coil. A resistor would partially match the characteristic impedance of the transmission line, but then most of the power would be dissipated in the resistor and not on the NMR coil. A resistor decreases the overall Q factor of the circuit where it is present. A lower Q factor also makes the circuit more tolerant against impedance changes due to lowering temperature. For a resistor close to the sample coil it is

necessarily required to be non-magnetic. In this work 1 Ω thin film resistors from Farnell were used with some probes in liquid helium environments.

2.1.9 The transmission line theory

A transmission line is a system of two parallel conductors (in the $\vec{z}$ direction) that transport electromagnetic energy. In a transmission line the mode of transmission of energy is the transverse electromagnetic mode (TEM) that is characterised by having only transverse (perpendicular to the transmission line) magnetic and electric field ($E_z = B_z = 0$) [16].

The circuital model

A transmission line may be considered as a quadrupole in the circuital model with an inductor L, resistances R_S and R_C and a capacitor C according to figure 2.6. The equations that govern this quadrupole (figure 2.6) are obtained by applying the Kirchoff laws to this circuit for instantaneous currents and voltages per unit length:

$$\frac{\partial V}{\partial z} = -(R + \mathrm{i}\omega L)I$$
$$\frac{\partial I}{\partial z} = -(G + \mathrm{i}\omega C)V$$

These differential equations have solutions of the type:

$$V(z) = V_0^+ e^{-\gamma z} + V_0^- e^{+\gamma z} \tag{2.6}$$

$$I(z) = [I_0^+ e^{-\gamma z} + I_0^- e^{+\gamma z}] \tag{2.7}$$

where γ is in this case the propagation constant and is given by:

$$\gamma = \alpha + \mathrm{i}\beta = \sqrt{(R + \mathrm{i}\omega L)(G + \mathrm{i}\omega C)} \tag{2.8}$$

and the characteristic impedance Z_0 is given by:

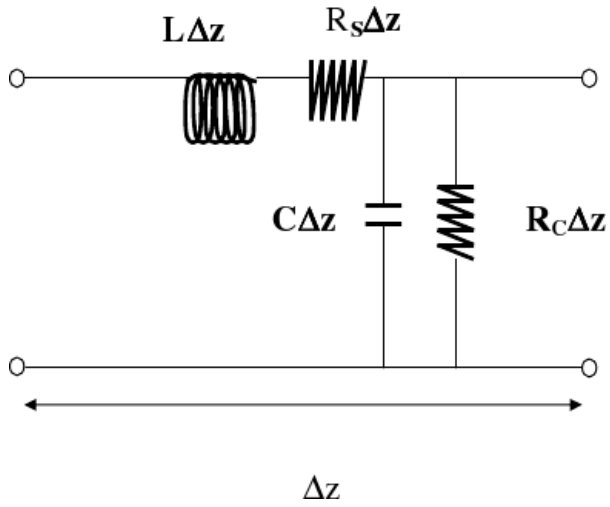

Figure 2.6: *Characteristic model of a finite transmission line described by lumped elements. The transmission line can be represented by an inductor L in series with a resistance R_S per unit length and a capacitor C with another resistance R_C in parallel per unit length.*

$$Z_0 = \sqrt{\frac{R + \mathrm{i}\omega L}{G + \mathrm{i}\omega C}} \tag{2.9}$$

The solution for these equations consists of a wave that travels in both directions. In the high frequency regime, the conditions $R << L\omega$ and $G << C\omega$ are fulfilled. When these two conditions are fulfilled, in a line with losses, the propagation constant γ may be expressed as

$$\gamma \simeq \mathrm{i}\omega\sqrt{LC} + \frac{1}{2}(R\sqrt{\frac{L}{C}} + G\sqrt{\frac{L}{C}}) = (\alpha + \mathrm{i}\beta) \tag{2.10}$$

where α and β are given in m^{-1}. In the limit of low losses ($\alpha \simeq 0$) the characteristic impedance of the transmission line is:

$$Z_0 = \sqrt{\frac{L}{C}} \tag{2.11}$$

The expression for L and C in a transmission line may be obtained experimentally by measuring the capacitance per unit length and the characteristic impedance of the line. The analytical expressions of L and C depend on the

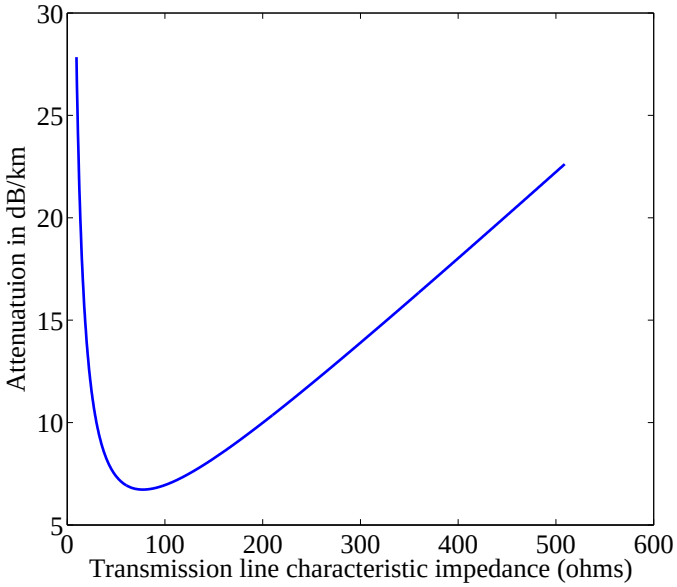

Figure 2.7: *Dependence of the attenuation in a coaxial cable with the characteristic impedance.*

geometry of the line and on the material it is made of. For a coaxial cable of inner and outer diameter a and b respectively, the expression of the capacitance and inductance per length unit [20] are:

$$C = \frac{2\pi\varepsilon_r\varepsilon_0}{\ln\frac{b}{a}} \tag{2.12}$$

$$L = \frac{\mu_0}{2\pi}\ln(\frac{b}{a}) \tag{2.13}$$

where ε_r is the relative dielectric constant of the medium. Most of the cables have a characteristic impedance of 50 Ω or 75 Ω. In a home-made transmission line it is possible to choose the dimensions of the inner and outer conductors at will to adapt the probe to the circumstances. The α attenuation constant changes with the characteristic impedance of the cable as shown in figure 2.7.

In this figure it is shown that large losses come with very low or very high Z_0, which is for the cases where the inner and outer conductors have almost the same diameter, or when the inner diameter tends to zero, respectively. For

most of the practical cases, where Z_0 was greater than 15 Ω, the losses were too little to be considered of importance in this case, since the length of the cable was at most 2 or 3 metres. For the cables used in probes for the stand alone polariser, this length was even shorter (not more than 1.2 metres).

The losses in a cable that finishes in a load equal to the characteristic impedance represent less than 0.5 dB in most of the cases. These losses are indeed important, but insignificant in comparison with the losses due to reflected power at a mismatched load, which at some points may be as large as 20 dB or even more. This figure provides valuable information about constraints on designing cables for a probe with limited space.

Finite transmission lines

From equations 2.6 and 2.7 it is possible to find the expression of the impedance presented by a finite transmission line at one side when there is a load impedance at the other side. For reference purposes, if the impedance which is at one extreme corresponds to the characteristic impedance of the transmission line, the impedance at the other side remains the same. If not, then the impedance seen at the load will be transformed along the transmission line. The expression of $V(z)$ is divided by $I(z)$ (from equations 2.6 and 2.7). Inserting $z = l$ and $z' = (l - z)$ it is possible to join both equations to substitute the voltages of forwarding and reflecting wave as the voltage and current at the beginning of the transmission line (with a load at the end Z_L). With some algebraic simplification the final equation for the impedance $Z(z')$ is:

$$Z(z\prime) = Z_0 \frac{Z_L + Z_0 \tanh(\gamma z\prime)}{Z_0 + Z_L \tanh(\gamma z\prime)} \tag{2.14}$$

The impedance at the beginning of the transmission line has a periodic behavior with the length of the cable and the frequency. This behaviour could be exploited to achieve a single resonance probe with large tuning range, by adjusting the dimensions and materials of the transmission line [13]. Now some cases of interest are analysed:

Case of low losses ($\alpha = 0$) For low loss transmission lines with an impedance Z_L at one extreme and length l, the impedance at the output is given by an approximation of equation 2.14:

$$Z(\beta l) = Z_0 \frac{Z_L + \mathrm{i} Z_0 tg(\beta l)}{Z_0 + \mathrm{i} Z_L tg(\beta l)} \tag{2.15}$$

Open circuit When the load is close to infinite the transformation at the other side becomes $Z = \mathrm{i}X_i$. This reactance may be positive or negative and having any value from $-\infty$ to $+\infty$ depending on the cable length and on frequency. A frequently used example is a piece of transmission line with a length of less than $\frac{\lambda}{4}$, which behaves as a capacitor.

Short circuit For a short circuit presented at the load point the transformed impedance is also reactive and it becomes $Z = -\mathrm{i}X_i$. As an example in the case of λ, $\beta << 1$ then the transmission line output behaves as an inductor.

$\frac{\lambda}{4}$ **transmission lines** In a transmission line where the electrical length $l = \lambda \frac{2n+1}{4}$ $(n = 0,1,2...)$ then the impedance becomes

$$Z = \frac{Z_0^2}{Z_L}$$

$\frac{\lambda}{2}$ **transmission lines** In a transmission line where the electrical length $l = \frac{n\lambda}{2}$ with (n = 0,1,2,...) the final impedance is the same as the load impedance:

$$Z = Z_L$$

The reflection coefficient It is defined as [14]:

$$\rho = \frac{\mid Z_L - Z_0 \mid}{\mid Z_L + Z_0 \mid}$$

It is used to measure how much power arrives at the load. It ranges from 0 (no reflection) to 1 (pure reflected power) but not in a linear scale. For example a reflection coefficient of 0.8 may still yield substantial power to the load [14].

Standing Wave Ratio In a transmission line which does not finish in the characteristic impedance there will be a reflected wave that will be superposed with the incoming wave. The resultant is a standing wave. The Standing Wave Ratio (SWR) is defined in the formula for lossless transmission lines as:

$$\mathrm{SWR} = \frac{1 + |\rho|}{1 - |\rho|}$$

It is possible to relate the reflection coefficient to the SWR:

$$|\rho| = \frac{\mathrm{SWR} - 1}{\mathrm{SWR} + 1}$$

2.1.10 Transferred power

Two main points for power reflection become important in a transmission line of length L_{TL} connected to a voltage source V_g at one side and to a mismatched impedance Z_{load} at the other side. The problem is represented in figure 2.8.

In figure 2.8 the scheme of a probe loaded with an input impedance $\mathrm{Z_{load}}$ presents two main points (a and b) where reflection may take place: at the entrance of the probe and at the load itself. For this scheme the power delivered to Z_i is:

$$P_i = \frac{|V_g|^2}{2} \frac{R_i}{((R_g + R_i)^2 + (X_g + X_i)^2)} \tag{2.16}$$

If the impedance $\mathrm{Z_{load}}$ corresponds to the characteristic impedance of the line Z_0 or R_0 ($\mathrm{Z_{load}} = Z_0 = R_0$) equation 2.16 becomes:

$$P_i = |V_g| \frac{R_0}{(R_g + R_0)} \tag{2.17}$$

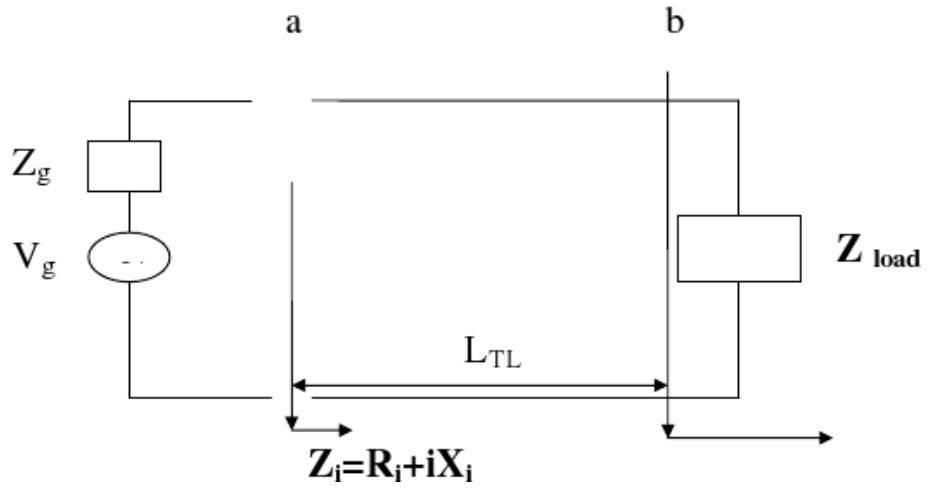

Figure 2.8: *Scheme of a transmission line loaded with an impedance Z_{load} in b which is transformed along the length l of the transmission line to a new impedance Z_i in a point a where it can be tuned and matched to the impedance Z_g of the source V_g or preamplifier. In the case in which the impedance Z_{load} is the same as the characteristic impedance of the transmission line R_0 there will not be any reflection at b. If this impedance corresponds to the impedance of the generator there is not reflection at a either and there is no need to use a tuning and matching network at a.*

It is clear that in the case in which the impedances presented by the preamplifier and generator are the same, only half of the power arrives to the load in the probe. A common situation ocurring in remote tuning is when the impedance at the output of the transmission line is tuned and matched to the source impedance $Z_i = Z_g$, but Z_{load} is not matched to the characteristic impedance of the transmission line, which will lead to power losses because of standing waves in the line and, if the power is high enough, it may even damage the source or preamplifier.

The condition of maximum power delivered to the load is obtained by differentiation of the expression for the power and equallising to zero.

$$\frac{\partial P_i}{\partial Ri_i} = 0 - -- > R_i = R_g$$

$$\frac{\partial P_i}{\partial Xi_i} = 0 - -- > X_i = -X_g \tag{2.18}$$

We obtain that the condition of maximum is loading the transmission line with the complex conjugate of the impedance of the power source $Z_i = Z^*$.

2.1.11 The B_1 field

To obtain the highest RF magnetic field B_1 in the sample coil the efficiency of the probe must be optimised. On the other hand the probes designed in this project were the result of compromise decisions taken and optimisation which yielded these results. For example, in the NMR coil, it has been shown by Hoult and Richards *et al* [11] that the solenoid yields stronger B_1 (from two to three times shorter pulses) in the centre of the coil than the saddle shaped coil having the same radius. It was seen that the B_1 presented a linear dependence with the SNR that scales with $\omega^{\frac{7}{4}}$. In this project the solenoid was used for NMR and diagnostic purposes since NMR parameters were optimised with this geometry. Saddle coils were used for DNP purposes since they allowed irradiation through the wings and sample access from top and bottom.

For mismatched probes it was important to improve the efficiency of the probe at delivering power to the bottom end of the transmission line. A general expression for this efficiency η has been shown by Kodibagkar et al [14] for a probe with a transmission line of length L and attenuation coefficient α:

$$\eta = \frac{e^{2\alpha L}(1-\rho^2)}{e^{4\alpha L} - \rho^2} \tag{2.19}$$

This shows how much power arrives to the load at the end of the line. If the reflection coefficient ρ approaches 0, the power is entirely passed to the circuit. Then the efficiency at the coil becomes the most important. Stringer *et al* [19] provided a relationship between efficiency in a circuit and the B_1:

$$\eta = \frac{\pi \xi f B_1^2 V_C}{\mu_0 Q_S P} \tag{2.20}$$

where V_C is the volume of the coil, P is the incident power, Q_S is the Q factor

of the coil, f is the frequency in Hz and ξ is:

$$\xi = \frac{\frac{1}{2\mu_0}\int_{\text{all space}} dV \vec{B}\vec{B}}{B_{\text{max}}^2 V_C}$$

which has given a value typically close to 1 [19].

Experimentally B_1 was measured in two different ways. In hyperpolarisation experiments the nuclear magnetisation becomes so large that a small flip angle yields enough SNR. If the build-up time or relaxation time (depending on whether there is microwave irradiation or not) is long enough (of the order of 15 minutes or more), then a pulse train of the same flip angle θ repeated n times in just a few seconds would leave a magnetisation magnitude M in $\text{Mcos}^n(\theta)$ smaller. By adequate fitting to this function it would yield enough precision in measuring the value of this tilting angle and, therefore, the 90^o pulse and B_1. Another experimental method relies on waiting until the magnetisation reaches thermal equilibrium and then applying a pulse. By increasing the pulse length a sinusoidal plot is obtained versus pulse length time. The first minimum after the first maximum is assigned the value of 180^o. In case the T_1 is very long, there is no need to reach thermal equilibrium provided enough time (and always the same time) is left between saturation and signal acquisition for sufficient SNR.

2.1.12 The Smith chart

The Smith chart is a graphical tool that helps in the calculations of the transmission lines. It represents the impedances normalised to an impedance that usually is 50 Ω:

$$z_L = \frac{Re(Z_L)}{Z_0} + \text{i}\frac{Im(Z_L)}{Z_0}$$

In this plot the values for the resistance or real part of the impedance are represented by the circles, the right point corresponding to infinity and the left point to zero, while the reactance or imaginary part of the impedance is rep-

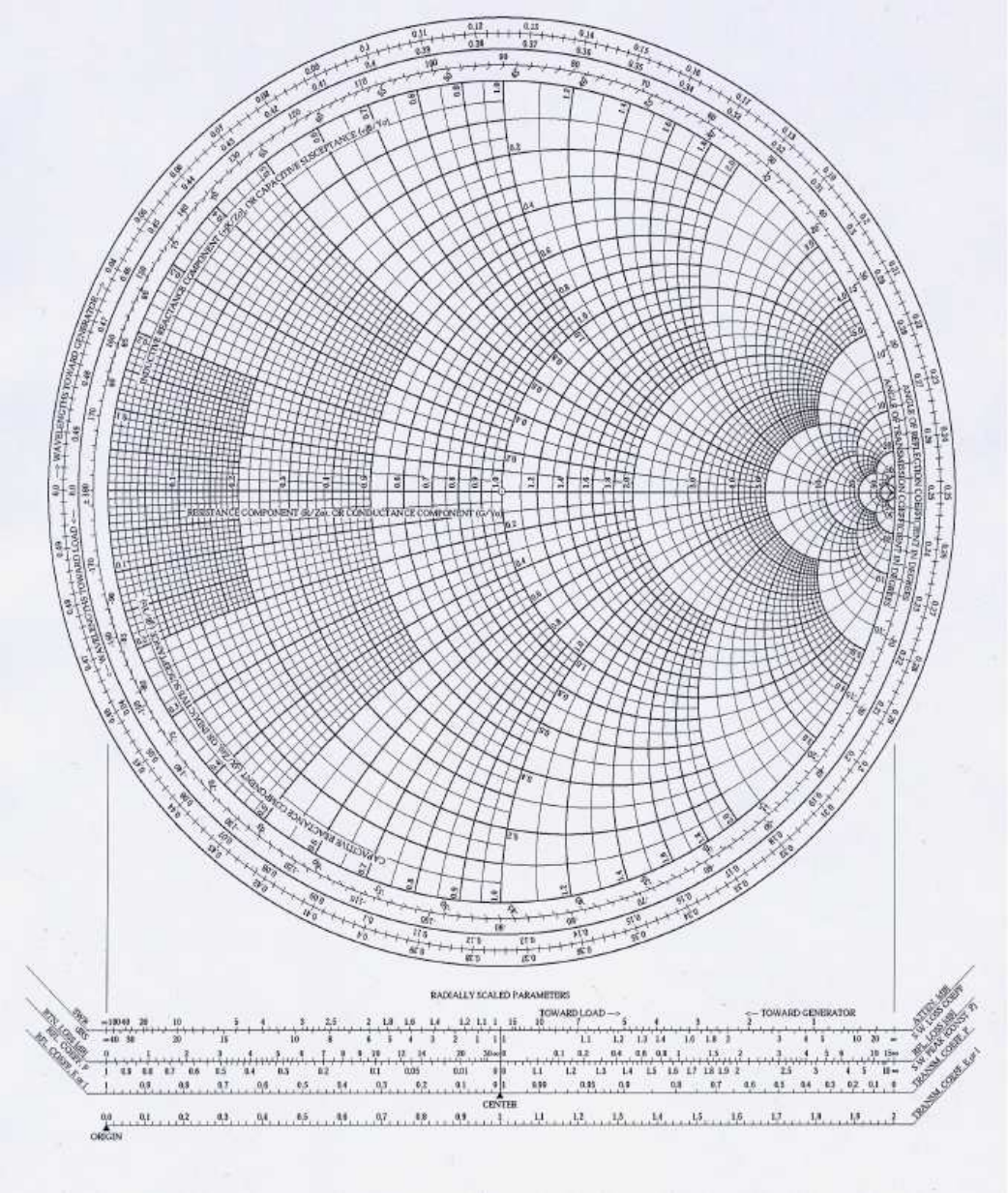

Figure 2.9: *Smith chart [21].*

resented by the arcs. In this way, changes in reactance only would correspond to a movement following one of these circles, while changes in resistance only would correspond to a movement following one of these arcs. Application of equation 2.14 is equivalent to saying that the representation of the impedance seen at the output of a mismatched low loss transmission line would pass by

the same point in the Smith Chart every $\frac{\lambda}{2}$ for a given wavelength.

The reflection coefficient corresponds to the distance from the centre of the chart (point of 50 Ω + 0i in a standard 50 Ω Smith chart) to the impedance point and the phase angle indicates the electrical distance to the closest voltage node. In case of having a pure reactance the impedance point would be placed at the outside of the chart: for an inductor it would be placed in the superior half of the chart, while for a capacitor it would be in the inferior half.

In case of having a $\frac{\lambda}{2}$ low loss transmission line, the impedance at one side of the transmission line would be the same as at the other side, having the same representation in the Smith chart. In case of having a $\frac{\lambda}{4}$ low loss transmission line, the representation of the output impedance in the Smith chart would be the symmetric point of the representation of the input impedance regarding the centre of the chart. These transformations are illustrated in figure 2.10 for an input impedance of a shortcircuit.

2.2 Radiofrequency probes

2.2.1 Remote and local tuning

In a tough environment of liquid helium for RF circuitry it was difficult (but not impossible) to set a trimmer capacitor and to rotate its shaft to tune a circuit. At the design stage two choices could be made. In a remotely tuned probe design there is a transmission line between the sample coil and the tuning and matching network. In a locally tuned probe the tuning and matching circuit is placed immediately after the sample coil. In this second case the maximum power transfer is achieved, and the main mechanism of losses depends on how low the Q factor of the circuit is and then on resistances of cables and soldering points (less than 1 dB in general for cable and soldering losses). In remote tuning designs the main problem to be considered is the reflection at the junction with the coil which, depending on the cases, may yield 10, 20, ...50 dB losses or more. Since impedances are transformed by low

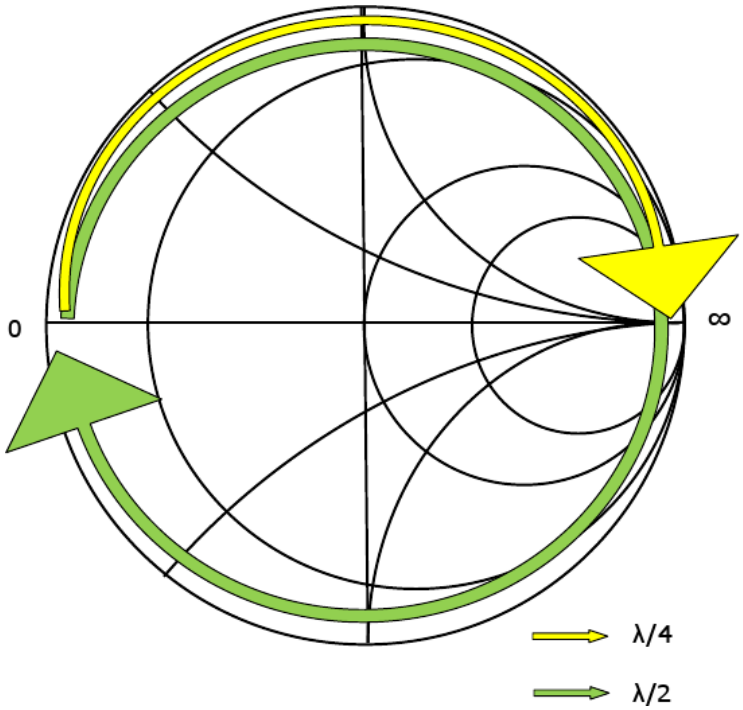

Figure 2.10: *Smith chart. Points of short circuit and open circuit are marked with 0 and ∞ respectively. The circumference in the right hemisphere that reaches the centre of the chart (point of 50 Ω + 0j) corresponds to the impedances with resistance of 50 Ω. The green arrow marks the transformation for a $\frac{\lambda}{2}$ and the yellow marks the transformation of a $\frac{\lambda}{4}$* for a termination of a short circuit (both arrows start from the same impedance point that corresponds with 0 + 0j or short circuit).

losses transmission lines in mismatched cables according to 2.15, and the ratio between the imaginary part and the real part of the impedance Z $\frac{Im(Z)}{Re(Z)}$ is not preserved, a Q factor measured at the output of the line does not yield any useful information [17].

2.2.2 Single resonance radiofrequency probes

Remote tuning involves a reflection at the coil, producing in some cases a large standing wave. It has been demonstrated that the largest diameter for the cable presented the minimum losses [13], [17]. In this project there was a maximum allowed space (15 mm) for this diameter, so some compromises were taken. The

selection of the sample coil was also a compromise in the sense that the small resistance offered by the wire of the coil matched the natural resistance of the transmission line. More turns of the wire would offer more resistance, but also it would shield the sample from irradiation coming from an external waveguide for dynamic nuclear polarisation experiments. Once the coil was chosen, it was matched with a series capacitor removing the imaginary part of the impedance (or most of it). The transmission line would transform the impedance to somewhere in the top part in the Smith chart (physically outside the magnet) where it was possible to tune and match it with a tuning and matching box. The main advantages of this design were the apparent simplicity and robustness and that the trimmer capacitors were placed at room temperature and pressure (they could even be magnetic). The main disadvantage was the lower efficiency since much of the power was reflected at the end of the transmission line.

The transmission line impedance transformation according to equation 2.15 exhibits a periodic behavior with length and frequency so a single parallel capacitor may resonate several at very distant frequencies. In the example of figure 2.11 a comparison is shown of two graphs: one of them corresponds to the experimental representation of voltage attenuation in a transmission line finished in a series resonant circuit NMR coil-capacitor. It was connected to two trimmer capacitors in parallel-series arrangement and these to the network analyser. The other graph corresponds to the negative value of the simulated real impedance $-\mid Z_{\mathrm{real}}(\beta l) \mid$ (equation 2.15) for the same circuit characteristics, with two tuning peaks that would correspond to the experimental points of maximum power transference. In this figure these two peaks are close to 40 MHz and 150 MHz which may tune to ^{13}C or ^{1}H frequencies at 3.35 T (35.88 MHz and 142.6 MHz respectively).

Single frequency remotely tuned and locally tuned probes

Some single resonance probes were designed with remote and local tuning yielding different performances. The results for single resonance remote and

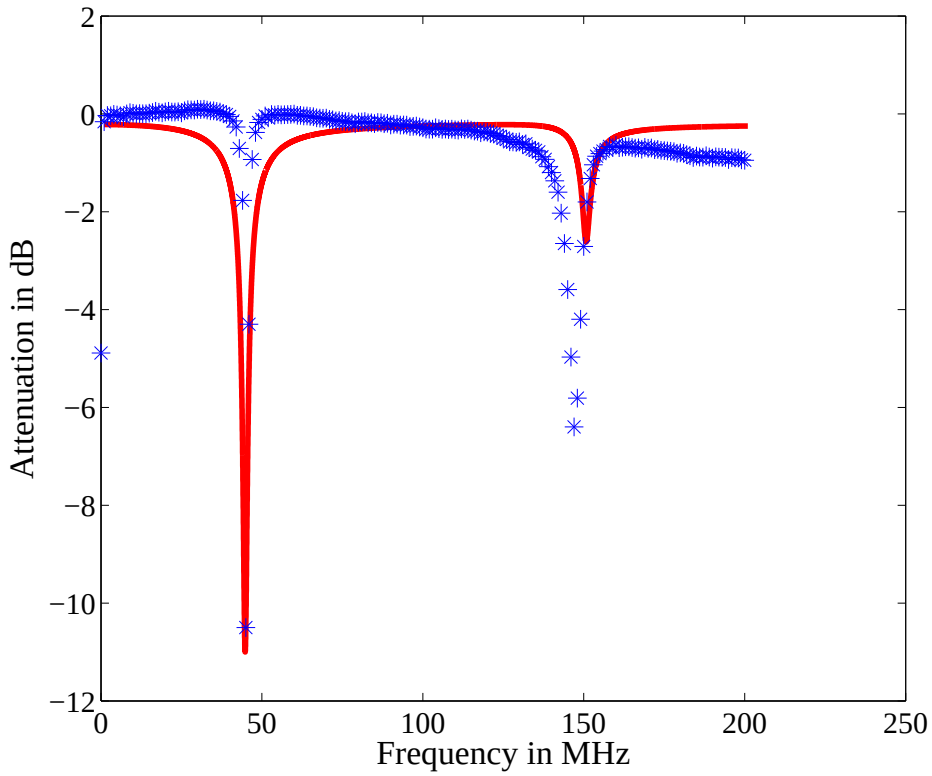

Figure 2.11: *Experimental values (stars) of voltage attenuation in dB for a circuit of type shown in figure 2.12. A comparative plot of the simulation (continuous line) of impedance* $-\mid Z(\beta l) \mid$ *in a.u. is shown with experimental data. The series fixed value capacitor for partial match* C_S *was 67 pF. The value for the sample coil (a saddle coil of silver plated copper of 0.6 mm diameter) was 70 nH. The cable was made of stainless steel 6 mm OD for the outer conductor and beryllium copper 1 mm OD for the inner conductor, 1 m long. At the other side two trimmer capacitors were placed in parallel series (in this plot parallel, 25 pF and series 15 pF).*

local tuning are shown for three different frequencies.

^{1}H probe

A remotely tuned probe for ^{1}H spins was implemented with a coil of 8 turns of enameled copper of 0.300 mm diameter around a 5.5 mm diameter cylindrical coil former of macor (1.5 mm pitch or space between turns), leaving an internal diameter of 4 mm. It was partially matched with a capacitance of 6.9 pF (ceramic capacitors of 4.7 + 2.2 pF in parallel) in series with the NMR coil. The transmission line was formed by two stainless steel tubes of 12 mm OD and 6 mm ID concentrically separated by PTFE spacers leaving a characteristic impedance of 41.5 Ω. At the top a bush clamped a hermetic SMA connector, where a tuning and matching box was connected. For a 90^{o} flip angle pulse of 5 μs 15 W was required.

^{13}C probe

A remotely tuned probe for ^{13}C was implemented with enamelled copper of 0.5 mm diameter in a 16-turn solenoid. It was held by a polyethylene coil former of 5 mm OD leaving a space for a sample cup of 4 mm. The wire enamel stopped the turns from touching themselves. It was attached to a 1.04 m long cable of 2.2 mm stainless steel outer conductor and 0.6 mm steel inner conductor with PTFE as a dielectric. The sample coil was matched with a series capacitor. The impedance at the other side allowed a transformation to 50 Ω with two trimmer capacitors in parallel-series arrangement. For a 90^{o} flip angle pulse of 16 μs 15 W was required. Two drawings of this probe are shown in figure 2.12.

^{15}N probe

For frequencies as low as 15 MHz (which was the case for the ^{15}N probe, remote tuning showed to be very inefficient (90^{o} of more than 500 μs). A single frequency locally tuned probe for ^{15}N was implemented by attaching a circuit in clad board in parallel-series with a coil of 4 turns of 0.300 mm thick enamelled copper wire on a frame of polyethylene, leaving an inner diameter of

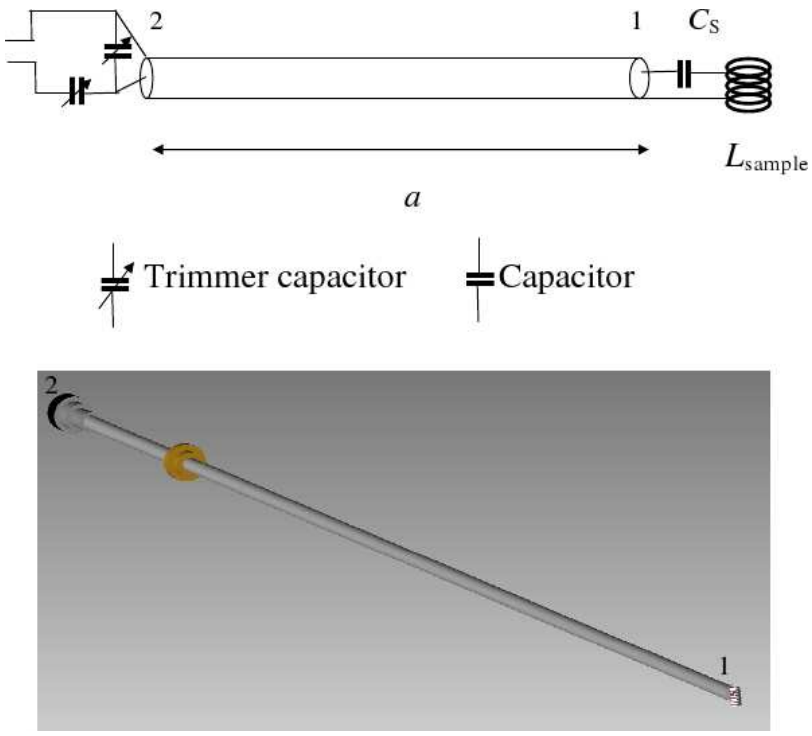

Figure 2.12: *Single resonance, remote tuned cryo-probe for* ^{13}C*. The coil inductance L is partially matched with the capacitor in series* C_S*. A 2.2 mm outer diameter of steel and 0.5 mm inner diameter of the same material was used as transmission line. Along a transmission line length a = 1.04 m the impedance was transformed by the transmission line until the point of contact (2) with the tuning and matching trimmer capacitors in parallel-series arrangement. The top figure shows a diagram and the bottom figure shows a 3D picture of the probe.*

4 mm. The transmission line used was 2.2 mm (outer diameter, OD) stainless steel, 0.6 mm (ID) stainless steel and 0.92 m long. The dielectric of this cable was PTFE. The circuit was implemented with non magnetic Ferroperm and ATC ceramic capacitors of fixed value. They were set in parallel series arrangement until the condition of resonance was obtained on the bench at room temperature. A thin film resistor of 1 Ω was in series with the sample coil. The Q factor presented by the circuit was 5 and the 90^o pulse was 8 μs for 300 W. In this probe there was a compromise between efficiency and ring-down times, since in this case the ring-down was close to 7 μs with the resistor and 80 μs if the circuit was implemented without it.

2.2.3 Double resonance RF probes

There are several strategies to solve the problem of double resonance NMR at liquid helium temperatures. From these only a few are described if not referenced, and fewer were implemented and tested at 1.5 K and 3.35 T. Some of these models of double resonance probes take advantage of the properties of the transmission lines [1], [2], [5]. From all the models the McKay probe was chosen as an elegant design of remotely tuned double resonance probe.

The McKay probe

The McKay probe design [1] is based on the properties of a lossless transmission line terminated by a mismatched load. This mismatched load is a coil with a capacitor in series that partially matches the lower frequency.

This elegant design presented two major advantages. It was relatively easy to build and the impedances could be tuned and matched remotely with non magnetic trimmer capacitors outside the magnet at room temperature. The fact that the cable in remote tuning belonged to the resonant structure translated in a source of losses. This problem has been tackled with large cable diameters (two to five cm in outer diameter) in the literature [13], [17]. For the present project a McKay probe was designed and built according to the space requirements for diagnostic purposes.

According to equation 2.14 the impedance at the bottom of the probe for the proton frequency (corresponding to a saddle coil, figures 2.14 and 2.13, 1) was transformed along the structure of the line passing through one or several points of minimum impedance where the branch for ^{13}C was connected (figures 2.14 and 2.13, 2). The impedance transformation depended on electrical length and on frequency. Selecting the maximum frequency to be used (usually protons) another cable could be plugged to one of these points without interfering significantly with the first frequency. Both channels continued from this common point through their respective cables until the impedance became tunable and matchable with two trimmer capacitors in parallel-series on each

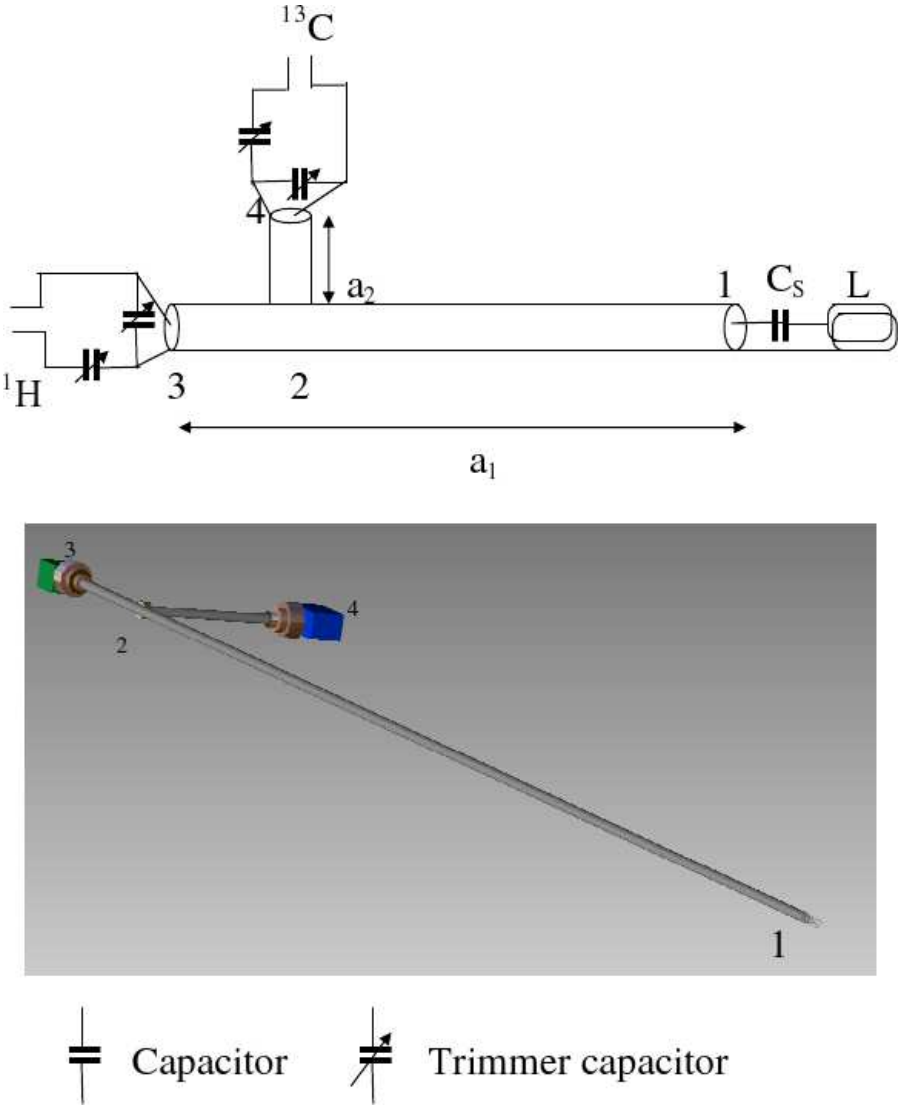

Figure 2.13: *Illustration of a McKay double resonance probe adapted for a stand alone polariser. In the scheme (top figure) the distance a_1 represents 1 m and the distance a_2 represented 15 cm. The input impedances for ^1H and ^{13}C at 1 were transformed until 3 and 4 respectively, and then tuned and matched with two trimmer capacitors. The branch for ^{13}C was connected at the point 2 of minimum impedance for ^1H.*

channel.

The resulting proton channel impedance was basically the same as for the coil input (figures 2.13 and 2.14, 3) since the cable length was $\frac{\lambda}{2}$. The proton impedance output was tuned (figure 2.14, 2) and matched (figure 2.14, 4)

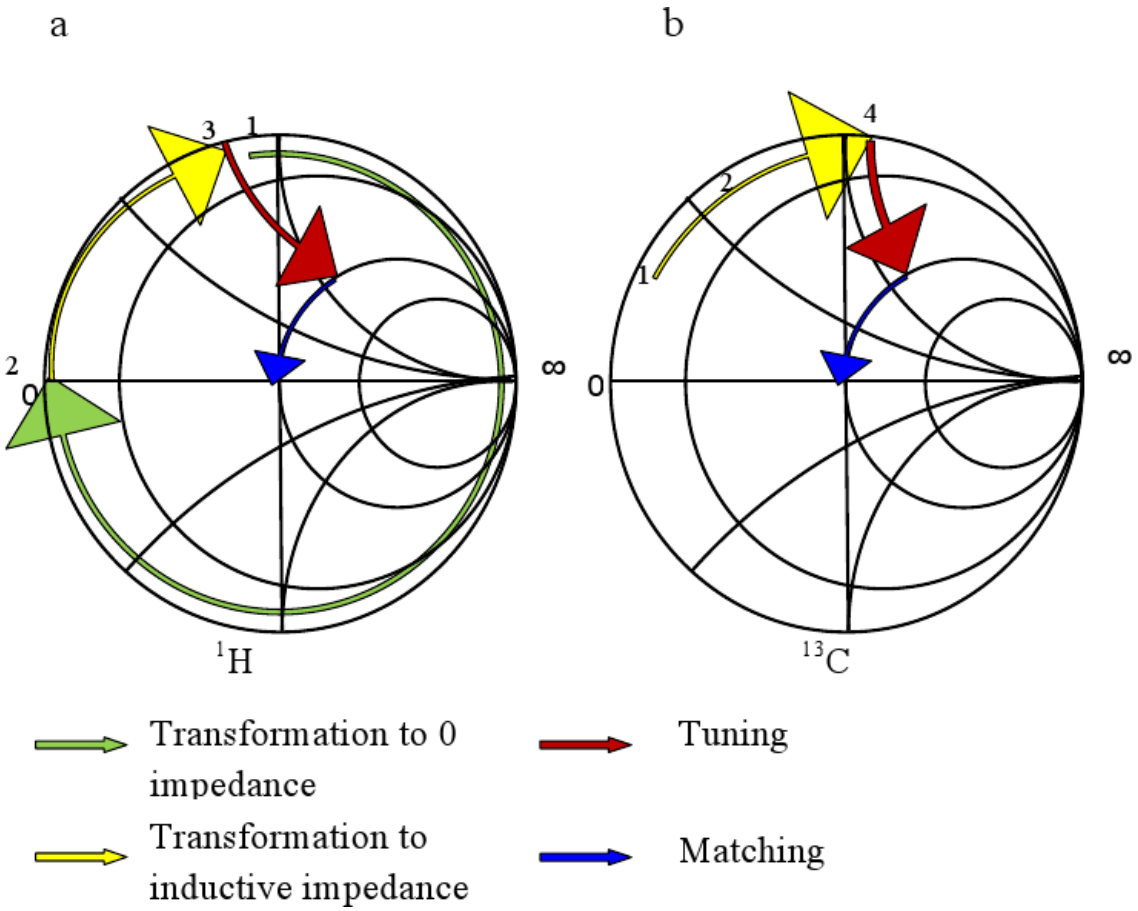

Figure 2.14: *Tuning and matching of the proton channel in a Mckay probe. The yellow arrow transforms the saddle coil impedance for protons to a point of minimum impedance, labelled 2. For this frequency this point corresponded with 0 in the Smith chart. The physically same point 2 is represented in the ^{13}C Smith chart plot on the right. Both of the two impedances corresponding to both frequencies were tuned and matched, as shown by the brown and red arrows respectively.*

with two trimmer capacitors in parallel-series arrangement. The ^{13}C channel was implemented in a similar way. Figure 2.13 illustrates the example of the McKay probe built in this project.

The probe was built from a home-made transmission line with a 6 mm steel tube (outer conductor) and a 1 mm BeCu wire (inner conductor). The conductors were separated by PTFE spacers. The resulting cable presented an impedance of 100 Ω. In the cold environment a saddle coil was connected

in series with a capacitor. The saddle coil was made using 0.6 mm silver plated wire allowing a 4 mm diameter sample. The capacitor reduced the reactive impedance of the lower frequency (35.88 MHz) and placed the point of minimum interaction outside the magnet, where the ^{13}C branch was connected. The tops were sealed with brass bushes and nuts that clamped a hermetic SMA connector for each channel. The two outputs were connected to a tuning and matching box for each frequency. The ^{13}C channel could be also tuned and matched to ^{23}Na since the tuning range also contained this frequency (37.73 MHz). Because of the presence of large standing waves, with this probe it was not possible to apply long pulses for the low frequency channel, which made it suitable to be used as a diagnostic probe. The length of the 90^o of this probe was 65 μs for ^{13}C and 10 μs for ^{1}H at 15 W for both channels. Since the ^{13}C branch was connected to the point of minimal impedance for protons, the proton channel presented an attenuation of about 30 dB from the ^{13}C channel, but the latter was isolated by only about 12 dB from the former, so the proton channel had to be tuned before the ^{13}C one.

Doty design probe

A simplified version of this design used lumped elements to tune and match locally the sample coil for two frequencies, as shown in figure 2.15, A [3], [7]. A resistor was used in series with the blocking inductor to reduce the ring-down time in the low frequency channel. Two double resonance probes were built following a modification of this design, by using remote tuning on protons instead of local tuning. The circuits in liquid helium are shown in figures 2.15, B and C (with a resistor in series with the blocking inductor). By using remote tuning the circuit was simplified in liquid helium and less space was required.

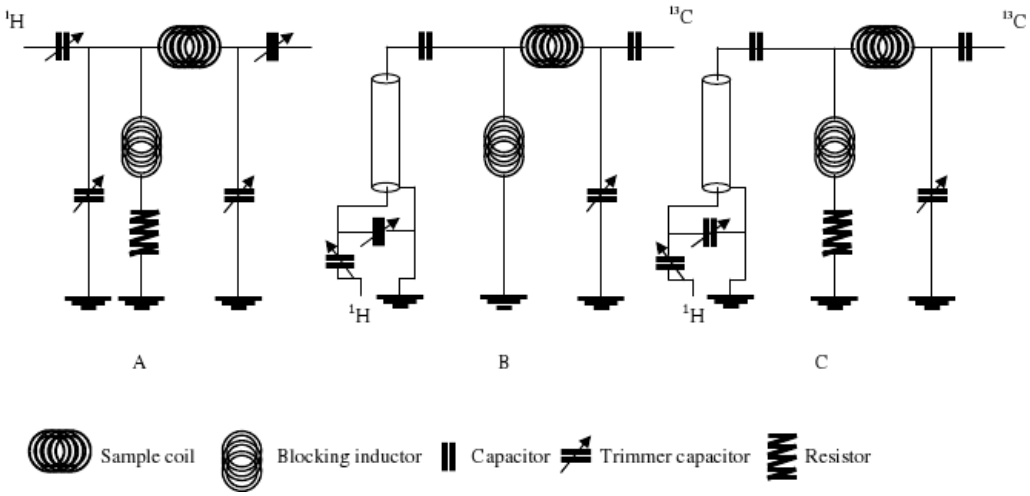

Figure 2.15: *Double resonance circuits for liquid helium environments based on a simplified circuit by Doty [7]. The circuit A by Cho et al [3] uses a resistor in series with the blocking inductor to decrease the ring-down time. The circuits B and C use remote tuning for the ^1H channel with a typical length of the cable of around 1 m. To save a trimmer in liquid helium, the match for ^{13}C channel was well approximated with a fixed capacitor. In circuit C a resistor is included to decrease the ring-down time of the ^{13}C channel.*

Description of a double resonance cryo-probe with a solenoid as sample coil

The double resonance probe itself consisted of two home-made coaxial rigid cables terminated in a circuit with a single sample coil for both resonant frequencies. Two tubes of non magnetic steel (6.5 mm external diameter with a wall thickness of 0.5 mm) 87 cm and 110 cm long were used for ^{13}C and ^{1}H respectively. For the ^{13}C cable an inner conductor of beryllium copper was used (0.6 mm BeCu wire) that was coated by PTFE (3 mm overall diameter). For the proton cable it was just a bare rod of non magnetic steel (3 mm external diameter). Inner and outer conductors in each cable were separated by PTFE spacers. The termination of the ^{1}H cable at room temperature was vacuum sealed by an SMA hermetic connector (Farnell), clamped with a home-made nut and thread to the cable. For the ^{13}C channel the connector was a hermetic

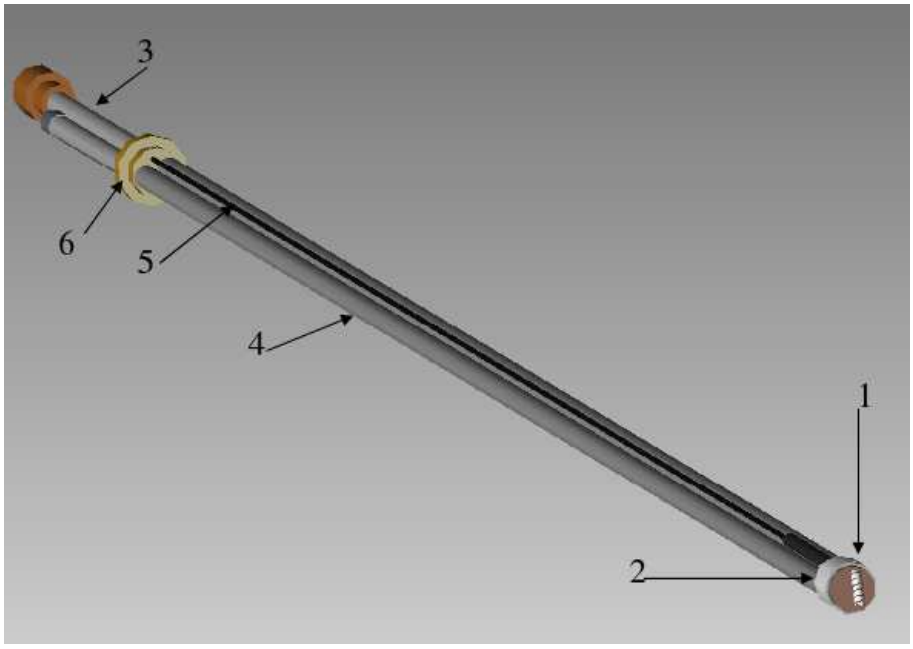

Figure 2.16: *Illustration of a cryo-probe suitable for cryogenic environments at 1.5 K. A solenoid was used as a sample coil (1). The circuit (2) used in this probe corresponded with figure 2.15, B and it was covered with PTFE tape in the probe. Two cables were used for the proton (3) and ^{13}C (4) channels. A non metallic rod (5) was used to tune the trimmer capacitor. A piece of brass (6) with a brass nut and an O ring attached the probe to the SAP and kept the system vacuum tight.*

BNC (Farnell), with the same scheme of nut and thread. The characteristic impedance measured was 45 Ω for the steel-steel cable, and 90 Ω for the ^{13}C channel. The length for the ^{1}H channel cable was 1.10 m to make it possible to tune and match it to 50 Ω outside the stand alone polariser (SAP) at room temperature. Both cables were soldered to a piece of brass that clamped on the thread at the entry of the variable transfer insert (VTI) with a brass nut, providing a vacuum seal between the exterior and the interior of the SAP.

The sample coil was a 1 cm long solenoid made of copper wire (0.300 mm) of 8 turns. For improved homogeneity of the coil, before it was inserted in the circuit, the wire was flattened to 0.150 mm for the plane side. The coil was mounted on a frame of macor and covered afterwards with glass fibre to fix the wire to the coil frame. The inner diameter for this solenoid frame was

4.1 mm, so a sample glass tube of 4.0 mm (Wilmad glassware) could be used as a sample cup. The impedance that this solenoid sample coil presented was 0.880 + 36.9i Ω for 35.88 MHz and 11.3 + 167i Ω for 142.71 MHz at room temperature. The blocking inductor was also a solenoid made of copper, 1 mm diameter thickness, 2 mm inner diameter. The impedance of this solenoid at room temperature was 0.110 + 9.8i Ω for 35.88 MHz and 1.64 + 39.6i Ω for 142.71 MHz. The tuning capacitor for ^{13}C was a 47 pF, non magnetic microchip capacitor (American Technical Ceramics, ATC) in parallel with a cryogenic trimmer capacitor of 38 pF range (Voltronics, NMTP38GEK) which was tuned from outside with a tuning rod. The matching capacitor was a fixed selected capacitor of 4.2 pF (two non magnetic microchip capacitors of 2.1 pF of Ferroperm in parallel). The ^{13}C channel was locally tuned and partially matched when the temperature became as low as 2 K. At this point, and provided that the capacitors were immersed in liquid helium, any tuning change was not significant. The local matching for the ^{13}C channel was selected beforehand, so when the temperature was 2 K, the impedance at the other side of the cable (room temperature) was 50 ± (5 + 5i) Ω. The partial matching capacitor for the ^{1}H served as a partial blocking capacitor for the lower frequency. It was a 47 pF non-magnetic microchip capacitor from ATC. The sample circuit was separated from the sample coil through a round piece of copper clad with copper only in one side. This side of copper had been divided in two to connect both legs of the sample coil and to isolate the sample coil from the blocking inductor. The sample coil was orientated 45^o with the horizontal plane and aligned with the incoming microwaves to improve the irradiation of the sample. The impedance of the ^{1}H channel in the bottom of the probe was transformed at room temperature into inductive impedance so it could be tuned and matched to the impedance of the preamplifier with standard non magnetic capacitors in parallel-series arrangement. The Q factor measured for the loaded probe was 40 for ^{1}H and 119 for ^{13}C at 1.5 K.

The performance of the probe was 5 μs for the ^{13}C channel with 8 W and

4.0 μs for the ^{1}H channel for a full power of 350 W. Pulses as long as 1.6 ms were applied for cross polarisation experiments with the proton channel at full power without experiencing arcing. For lower powers (300 W for the ^{1}H channel), longer pulses of 2 or 3 ms were used. For the power level used the channels did not present any arcing problem. With the filters placed before the preamplifier the probe presented a protection of no less than -75 dB cross talk attenuation.

For comparison purposes, the proton channel was disconnected and the blocking inductor removed, leaving a parallel-series locally tuned circuit with the same coil that presented a 4.4 μs long 90^{o} pulse at 8 W. Using equation 2.19 the overall efficiency would drop to 45% of this comparison value just because of the leakage and would increase the 90^{o} pulse length from 4.4 to 6.5 μs.

Probe with saddle and two cables

With some changes in the former probe model, it was possible to build a test probe for the dual centre magnet. The major limitation for this case was the narrow space allowed for the cables (2.2 mm). A further complication was the necessary length (2 m) of these cables. They had to be parallel to the 2 m long corrugated waveguide and be moved about 30 cm down with it for dissolution experiments.

The test probe for the stand alone polariser had shorter cables (figure 2.17). For the proton channel a US-85-B-SS semi-rigid coax cable of 87 cm was used. The outer conductor of this cable is 2.2 mm of stainless steel and the inner conductor 0.5 mm of BeCu, with PTFE as dielectric. For the ^{13}C channel the cable had the same characteristic as the first one, but with an inner conductor of steel instead of BeCu. This test probe was built following the circuit in figure 2.15, C. The sample coil had a saddle configuration supported by a macor coil former. The coil was 4 mm diameter with two turns per wing with 150 μm diameter enamelled copper wire. The coil former left an inner space of

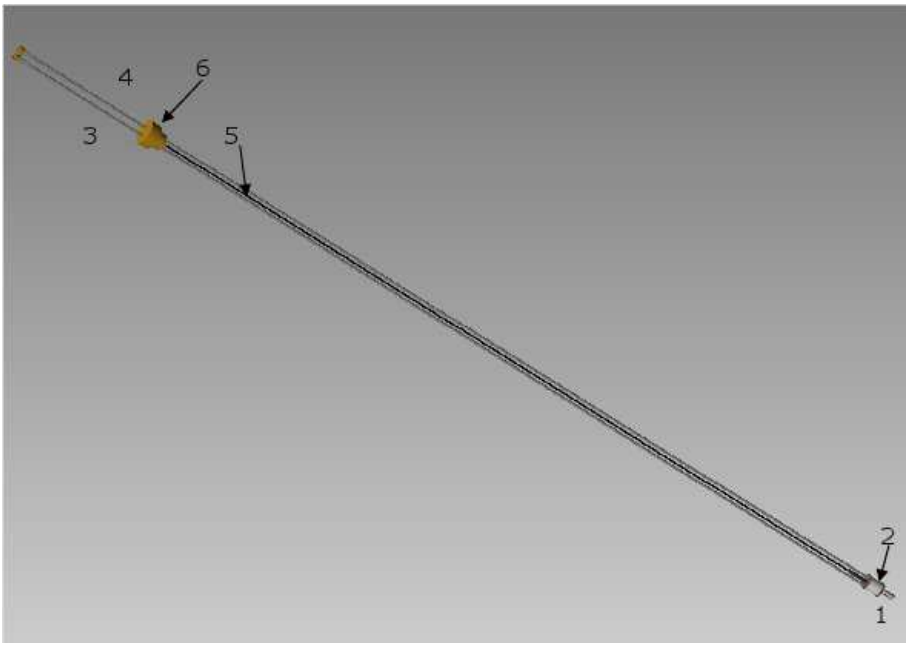

Figure 2.17: *Illustration of a cryo-probe suitable for cryogenic environments at 1.5 K. A saddle coil was used as a sample coil in this case (1). The circuit (2) used in this probe corresponded with figure 2.15, C and it also was covered with PTFE tape in the probe. Like in the previous model two cables were used for the proton (3) and ^{13}C (4) channels. A non-metallic rod (5) was used to tune the trimmer capacitor. A piece of brass (6) with a brass nut and an O ring attached the probe to the SAP and kept the system vacuum tight.*

1.5 mm diameter inside for a cylindrical probe in a capillary. The capacitors were from ATC apart from the non magnetic Voltronics trimmer capacitor used for the ^{13}C frequency tuning, which was achieved using a non-metallic tuning rod. The resistor in series with the blocking inductor was a 1 Ω thin film resistor. The performance of this probe was 6 μs for ^{13}C at 86 W and 9 μs for ^{1}H at 300 W for 90^o pulses. The ring down times were 7 μs and less than 5 μs for ^{13}C and ^{1}H respectively. The total isolation for both channels, with filters included, were 93 dB on each channel.

A similar circuit was used in the dual centre magnet using a 10 mm long saddle shaped coil of 7 mm inner diameter, made of two turns per wing with a 300 μm enamelled copper wire, and a trap of three loops with the same wire. The 90^o pulse duration was 14 μs at 300 W for ^{1}H and 6.5 μs at the same

power for ^{13}C.

Probe for dissolution

This probe offered a solution to the problem of linking both cross polarisation and dissolution. For doing so, the sample had to be accessible to the microwaves for DNP and also to a dissolution dock from above. A saddle coil was therefore preferred as a sample coil.

The probe was partially based on a McKay design: the ^{1}H impedance at the sample coil was transformed by a coaxial cable to a point of 0 Ω outside the magnet where the ^{13}C channel was connected. The cable for the ^{1}H channel was further extended to a new impedance point where it was tuned and matched to 50 Ω with two parallel-series trimmer capacitors.

The main body of the probe was composed of two non magnetic steel tubes concentrically arranged to serve as a coaxial cable. It fixed the sample in position and acted as a lead for the dissolution dock to the sample. The outer tube (figure 2.18, 1) had a steel 12.7 mm outer diameter, 0.25 mm wall thickness and 83 cm length. The inner tube was 87 cm long to allow some length above and below the outer tube. It had 8 mm OD and 0.2 mm wall thickness. Both tubes were separated by spacers of PTFE, yielding all together a coaxial cable with characteristic impedance of 25 Ω. The top of this coaxial cable formed a vacuum seal between the outer and the inner tubes. It was made of a plumber plastic adaptor (figure 2.18, 2) that compressed an O-ring between two metallic washers, each one soldered to the end of each tube. A vacuum seal for the inner tube was made using a rubber septum (figure 2.18, 3). For dissolution, this rubber septum was removed and the dissolution dock inserted in the inner tube until it reached the sample. Close to the warm end (4.5 cm away) of the main body a 8.5 cm long branch was soldered (figure 2.18, 4). This branch finished in a brass bush with a thread. A hermetic SMA bulkhead connector was attached to this end with a nut made of brass. This bulkhead was connected to the inner conductor.

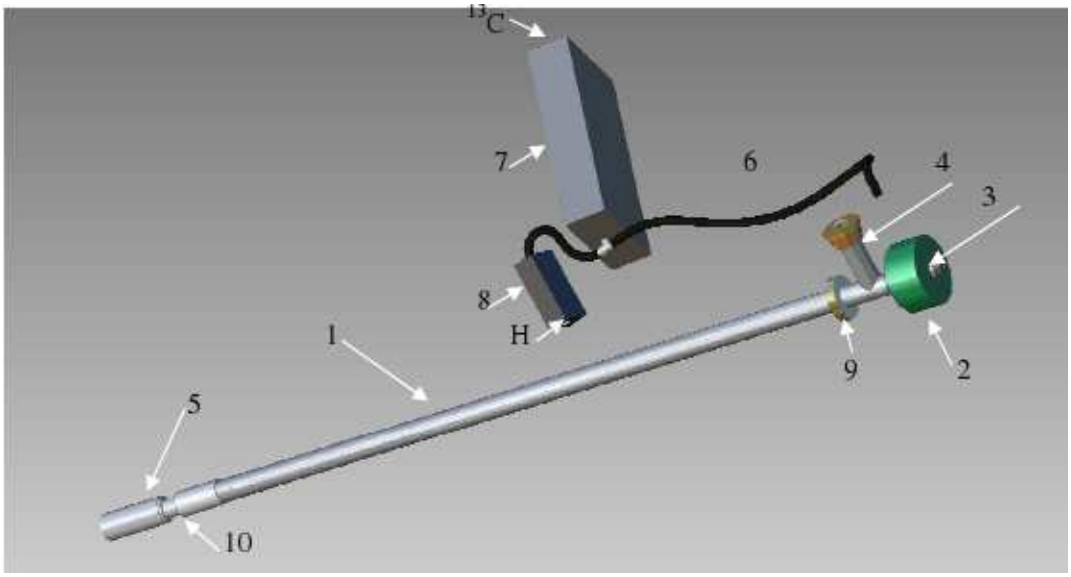

Figure 2.18: *Cryogenic probe for diagnostic, cross polarisation and sample dissolution. The main body of the probe was a 12.7 mm thick cable (1) with a stainless steel tube as inner conductor that allowed access to the sample coil (5) with a dissolution dock from (3). This entrance was vacuum sealed with a rubber septum. The probe was attached and vacuum sealed with the SAP with a nut (9). Both tubes (inner and outer conductors of the main body cable) were vacuum sealed together with a clamp (2). The probe presented a circuit (11) at liquid helium temperatures that tuned and matched the lower frequency. An extension cable (6) was plugged to the RF output (4) which led to a BNC T connector. A ^{1}H filter (7) and a further extension cable that led to a tuning and matching box for ^{1}H (8) were connected to this T BNC connentor.*

The cold end of this homemade coaxial cable was terminated in a machined PTFE part that served as a coil former, and a circuit and sample cup holder. The PTFE part (figure 2.18, 5) was partially inserted in the space between the tubes. It was attached to the home-made coaxial cable with a steel reinforcement (which was finished in a ring that clamped in a step of the PTFE part). The PTFE part had a tapered hole into which the inner stainless tube was inserted. The tapered hole allowed direct access to the sample cup.

The sample coil (L_{SAMPLE} in figure 2.19) was a saddle coil with 2 turns per wing, vertically arranged in the coil former to provide physical access

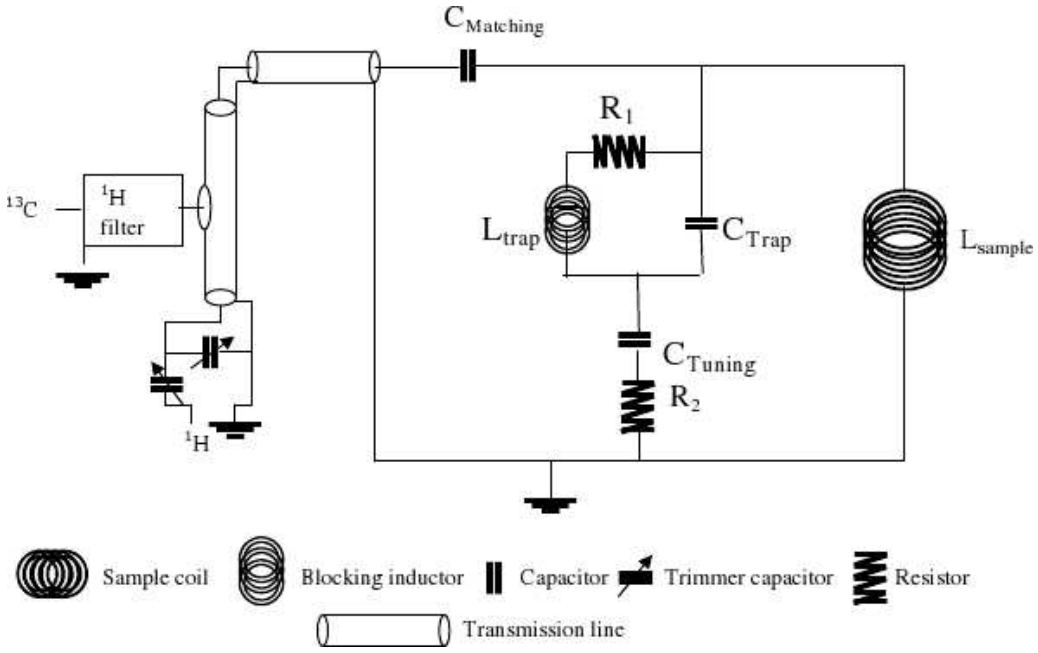

Figure 2.19: *Scheme of the probe for diagnostic, cross polarisation and dissolution experiments. It presents a sample coil which is locally tuned and matched to 50 Ω to ^{13}C and remotely tuned and matched to the proton frequency. A ^{1}H filter is connected in T before the ^{13}C output.*

to the sample cup from above, as shown in figure 2.19. A 0.150 mm thick enamelled copper wire was used. The saddle coil was 11 mm long with an internal diameter of 5.5 mm.

The circuit was basically a parallel series resonant circuit for ^{13}C with a ^{1}H trap in series with the ^{13}C parallel capacitor, as shown in figure 2.19. The tuning capacitance C_T was 2.2 pF Ferroperm, in parallel with 22 + 33 pF microchip Murata capacitors and the matching capacitance C_M was 37 pF, made by a combination of Murata and Ferroperm capacitors). Two 1 Ω thick film resistors (Farnell), R_1 and R_2, were inserted in the circuit to decrease the ^{13}C channel ring-down time to 12 μs for ^{13}C and less than 5.0 μs for ^{1}H and to make it more tolerant to impedance changes with temperature.

The trap was a three loop coil of 4 mm diameter covered with copper foil, which was resonated with a capacitance in parallel of 35.7 pF, made using ceramic chip capacitors of 2.7 pF. In series with the trap coil there was a 1 Ω

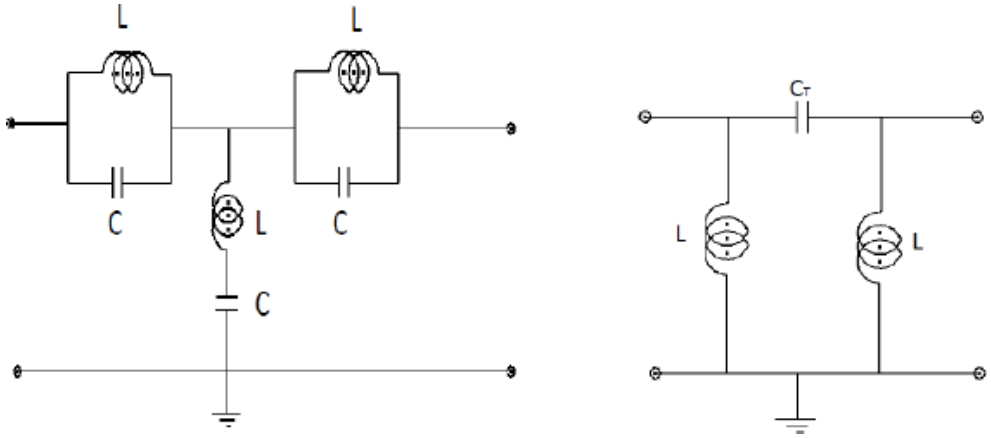

Figure 2.20: *Filters. On the left a design based on three traps for proton frequency is shown. On the right there is a high pass filter design for* ^{13}C.

resistor R_1.

In this way the ^{13}C channel was tuned and matched at low temperature. The ^{1}H channel was remotely tuned. The output of the probe was connected to a cable of $\frac{31\lambda}{144}$ (figure 2.18, 6) to get 0 Ω for the ^{1}H frequency, and $\frac{\lambda}{12}$ to tune and match it to 50 Ω with two parallel-series trimmer capacitors in a box (figure 2.18, 8). The ^{13}C channel was connected to the point of minimum interaction for ^{1}H. To avoid ^{1}H current leakage to the ^{13}C channel, a ^{1}H filter was inserted at this point (figure 2.18, 7). A ^{13}C filter was inserted just before the ^{1}H preamplifier. The length of the 90^o pulse of the probe was measured to be 13 μs for ^{13}C at 18 W and 11.5 μs for ^{1}H at 135 W.

The total frequency attenuation for cross talk protection just before the preamplifiers was no less than 70 dB for both channels.

Filters

In this project only two simple designs were implemented on copper circuit board to isolate ^{1}H and ^{13}C frequencies. The filter designs for protons and ^{13}C frequencies are shown in figure 2.20.

The performance of the proton filter was 62.5 dB attenuation for ^{1}H and 0.2 dB for ^{13}C. The coils were made of 3 turns of 1.76 mm diameter copper and high power capacitors selected to get resonance on each trap, with a typical

value of 14.7 pF. The diameter of each turn was 10 mm. The ^{13}C filter offered 43 dB attenuation for ^{13}C frequency and 0.5 dB for ^{1}H. The coils were 3 turns with 11 mm diameter solenoids, 1.75 mm diameter wire and the capacitance was 14.7 pF with 10 pF and 4.7 pF high power chip capacitors.

2.2.4 Discussion

Depending on their design the different probes had different performances. Some significant parameters are shown in tables 2.3 and 2.4.

Probes and ω	^{13}C	^{1}H	^{15}N
Sample coil type	Solenoid	Solenoid	Solenoid
No of turns	16	8	4
Remote/local	Remote	Remote	Local
Coil internal diameter (ID) (mm)	4.5	5.5	4.5
Cable Outer diameter (OD) (mm)	2.2	12.7	2.2
Z_0 (Ω)	50	41.5	50
90^o pulse (μs)	16	5	8
Power (W)	15	15	300

Table 2.3: Several parameters in single resonant cryo-probes.

In these tables it is shown that the best performance for ^{13}C was obtained with the double resonance probe using a solenoid. The inclusion of resistors in this design translated into longer pulses in the test probe for the dual centre magnet and in the probe for dissolution experiments. The shorter pulse for ^{1}H was obtained with the single resonance probe for proton frequency. A worse performance was obtained with a shorter line diameter in the Mckay probe, but in this probe a saddle coil was used, which reduced the B_1 field [11] in comparison with the solenoid. Comparing the solenoid single resonance probe with the double resonance probe for dissolution experiments it was found that a much higher power was necessary to obtain a pulse twice as long as with the single resonance probe for ^{1}H.

The inclusion of a trap with resistors translated into high power losses

Probes and ω	^{13}C-M	^{1}H-M	^{13}C-D	^{1}H-D	^{13}C-S	^{1}H-S
Coil type	saddle	saddle	Solenoid	Solenoid	saddle	saddle
No turns	1	1	8	8	2	2
Remote/Local	R	R	L	R	L	R
Coil ID	4	4	4.5	4.5	4.0	4.0
Cable OD	6.5	6.5	6.5	6.5	2.2	2.2
Z_0 (Ω)	100	100	90	45	50	50
90^o pulse (μs)	65	10	6.5	4	6.0	9
Power (W)	15	15	8	350	86	300

Table 2.4: Several parameters in double resonant cryo-probes for liquid helium temperatures. The frequencies corresponding to ^{13}C and ^{1}H were 35.88 MHz and 142.6 MHz respectively. The McKay probe is denoted by M, the simplified Doty design by D and the test probe by S. Coil inner diameters (ID) and cable outer diameters (OD) were measured in mm. The characteristic impedance of the used transmission line was denoted by Z_0 in the table.

which, on the other hand, allowed to tune and match a circuit in liquid helium temperatures without the need of a trimmer capacitor at liquid helium temperatures. The small size of the circuit left enough space to access to the sample with a dissolution dock. Using the resistors the dissolution probe with a saddle coil showed equivalent B_1 strength compared with the single resonance probe for ^{13}C with a solenoid, which was used mainly for solid state NMR experiments. The test double resonance probe showed a pulse of 6 μs at 86 W, which did not differ too much from 13 μs at 18 W, since the length of the pulse doubles when the power is reduced by a factor of 4. At the time of writing, and for these low field and operation temperatures, only the probe for DNP by Cho *et al* [3] was found comparable in performance to the double resonance probes built and used for cross polarisation experiments in this project.

Probes and ω	^{13}C-CPD	^{1}H-DPC
Coil type	saddle	saddle
Solenoid	Solenoid	saddle
saddle	saddle	saddle
No turns	2	2
Remote/Local	L	R
Coil ID	5.0	5.0
Cable OD	12.7	12.7
Z_0 (Ω)	25	25
90^o pulse (μs)	13	11.5
Power (W)	18	135

Table 2.5: Several parameters in a double resonant cryo-probe for liquid helium temperatures. The frequencies corresponding to ^{13}C and ^{1}H were 35.88 MHz and 142.6 MHz respectively. The probe is denoted with CPD (Cross Polarisation and Dissolution). Coil inner diameter (ID) and cable outer diameter (OD) were measured in mm. The characteristic impedance of the used transmission line was denoted by Z_0 in the table.

2.3 Conclusions

Several NMR cryo-probes were built for solid state NMR and DNP experiments. The single resonant cryo-probes were used for diagnostic purposes in DNP. The double resonant probes were built for DNP experiments and CP experiments. A double resonant probe made simultaneous measurements of ^{13}C and ^{1}H in NMR and DNP experiments possible which reduced the experimental time. As shown by the length of the 90^o pulse of these probes, these designs were not optimal, but they provided an idea of the effect of several parameters: a compromise was found for probes which could be used for DNP, NMR, CP and dissolution experiments. In these probes remote and local tuning were used as a compromise between strong B_1 fields and available space. The use of resistors made it possible to tune and match without trimmer capacitors at liquid helium temperatures at the expense of larger losses, an acceptable compromise for this project.

Bibliography

[1] McKay R. (A) MONSANTO (1984-05-01)Double-Tuned single coil probe for nuclear magnetic resonance spectrometer. US4,446,431 (A). Application number US19810295940 19810824 Priority number US19810295940 19810824.

[2] R. Coxon and P. Mansfield 1994 Coil circuits (1994-06-28) US5325060 (A) international: A61B5/055; G01N33/22; G01R33/36; G01R33/385; G01R33/389; A61B5/055; G01N33/22; G01R33/32; G01R33/38; (IPC1-7): G01V3/00 Priority number GB19900011757 19900525; WO1991GB00826 19910524.

[3] H. Cho, J. Baugh, C. A. Ryan, D. G. Cory, and C. Ramanthan. Low temperature probe for dynamic nuclear polarization and multiple-pulse solid state NMR. *J. Mag. Res.*, 187:242–250, 2007.

[4] Brian Cowan. *Nuclear Magnetic Resonance and Relaxation.* Cambridge University Press, 1997.

[5] V. R. Cross, R. K. Hester, and J. J. Waugh. Single coil probe with transmission-line tuning for nuclear magnetic double resonance. *Rev. Sci. Instrum.*, 47,12, 1976.

[6] F. D. Doty. Solid state probe design. *www.interscience.wiley.com*, http://www.dotynmr.com/PDF/1995 ENMR Doty %20Solids Probes.pdf, 2007.

[7] F. D. Doty, R. R. Inners, and P. D Ellis. A multinuclear double-tuned probe for applications with solids or liquids utilizing lumped tuning elements. *J. Mag Res.*, 43:399–416, 1981.

[8] F. D. Doty, G. Entzminger Jr, and C. D. Hauck. Error-tolerant RF litz coils for NMR/MRI. *J. Mag. Res.*, 140:17–31, 1999.

[9] B.C. Gerstein and C. R. Dybowski. *Transient techniques in NMR of solids-An introduction to Theory and Practice.* Academic Press, Inc, 1985.

[10] D. I. Hoult. Fast recovery, high sensitivity NMR probe and preamplifier for low frequencies. *Rev. Sci. Instrum.*, 50,2, 1979.

[11] D. I. Hoult and R. E. Richards. The signal-to-noise ratio of the nuclear magnetic resonance experiment. *J. Mag. Res.*, 24:71–85, 1976.

[12] S. Kan and J-P Ruand. Method to fabricate split coaxial line UHF probes for high-resolution NMR experiments. *Rev. Sci. Instrum.*, 58:doi:10.1063/1.1139503, 1962 (1987).

[13] Y. W. Kim, W. L. Earl, and R. E. Norberg. Cryogenic probe with low-loss transmission line for nuclear magnetic resonance. *J. Mag. Res.*, 116 A:139–144, 1995.

[14] V. D. Kodibagkar and M. S. Conradi. Remote tuning of NMR probe circuits. *J. Magn. Res.*, 144:53–57, 2000.

[15] A. F. Privalof, S. V. Dvinskikh, and H. M. Vieth. Coil design for large-volume high-B_1 homogeneity for solid state NMR applications. *J. Mag. Res.*, 123, A:157–160, 1996.

[16] F. Rachidi and S. V. Tkachenko. *Electromagnetic field interaction with transmission lines - from classical theory to HF radiation effects.* WIT Press, Athenaeum Press Ltd., 2008.

[17] C. Rienstra. *Solid state nuclear magnetic resonance methodology for biomolecular structure determination.* PhD thesis, MIT, 1999.

[18] C. E. Garrido Salmon, E. L. Gea Vidoto, M. J. Martins, and A. Tannus. Optimisation of saddle coils for magnetic resonance imaging. *Braz. J. Phys.*, 36:1A, 2006.

[19] J. A. Stringer and G. P. Drobny. Methods for the analysis and design of a solid state nuclear magnetic resonance probe. *Rev. Scient. Instrum.*, 69,9, 1998.

[20] P. A. Tipler. *Fisica.* Worth Publishers , Reverte, SA, Bilbao, 1997.

[21] Department of electrical University of Western Ontario and computer engineering. *http://www.eng.uwo.ca/electrical/information/ /courses/ece3336b/SmithChart.jpg.* October, 2009.

[22] Jr V. Perna. *The RF Capacitor Handbook.* American Technical Ceramics (NY), 1994.

Chapter 3

Relaxation and Brute Force Polarisation

Hyperpolarisation of the nuclear spin system leads to low spin temperature of the nuclear Zeeman reservoirs. The low spin temperature may be obtained by establishing thermal contact between the nuclear Zeeman reservoir and another, much colder, thermal reservoir. The most direct way to achieve this target is by lowering the lattice temperature (or sample temperature) of the spin system to levels where, in thermal equilibrium the nuclear Zeeman Boltzmann population is high enough. The main problem with this approach is the time necessary to achieve such a Boltzmann equilibrium since the longitudinal relaxation time becomes exceedingly long at very low temperatures. The experiments described in this chapter aim to achieve a solution to this problem for future dissolution experiments using ^{13}C labelled compounds after they have been highly polarised with this technique. Improved thermal contact between ^{13}C spin (Zeeman and dipolar) thermal reservoirs and the lattice (through the phonon reservoir) is obtained by doping the sample with paramagnetic impurities. Their presence in the sample will determine the main mechanism of relaxation. Several lanthanides have been tested at a temperature close to 1.5 K, in order to measure the changes in relaxation of nuclear spin species (especially ^{13}C) due to these paramagnetic agents. The sample

chosen for these experiments was ^{13}C labelled acetate (2 M approximately in all the experiments) in a glassy matrix of 1:1 glycerol-water.

3.1 Polarisation and sample temperature

At low temperature (close to 1.5 K) in a solid state sample the nuclear spins are fixed in position with respect to the paramagnetic impurities. The ^{1}H and the ^{13}C spin systems relax to thermal equilibrium.

3.1.1 The Brillouin Function

Following a microscopic model for paramagnetism in a canonical system, the unpaired electronic spins which form the electron polarisation in a sample align with the magnetic field $\vec{B}_0$, but in a proportion given by the Brillouin function given in 3.1:

$$B_J = \frac{1}{J}[(J+1)coth(\frac{\gamma B_0}{k_B T}(J+\frac{1}{2})) - coth(\frac{\gamma B_0}{2k_B T})] \tag{3.1}$$

where J is the angular momentum, γ is the gyromagnetic ratio, k_B is the Boltzmann constant and T is the temperature. For $J = \frac{1}{2}$ the Brillouin function can be simplified to:

$$B_{\frac{1}{2}} = tanh(\frac{\gamma B_0}{2k_B T}) \tag{3.2}$$

Plotting the polarisation for a magnetic field of 3.35 T reveals that the electron polarisation is almost the maximum value at temperatures close to 1.5 K while it requires very low temperatures in the order of a few millikelvin to achieve the same polarisation for ^{1}H or ^{13}C.

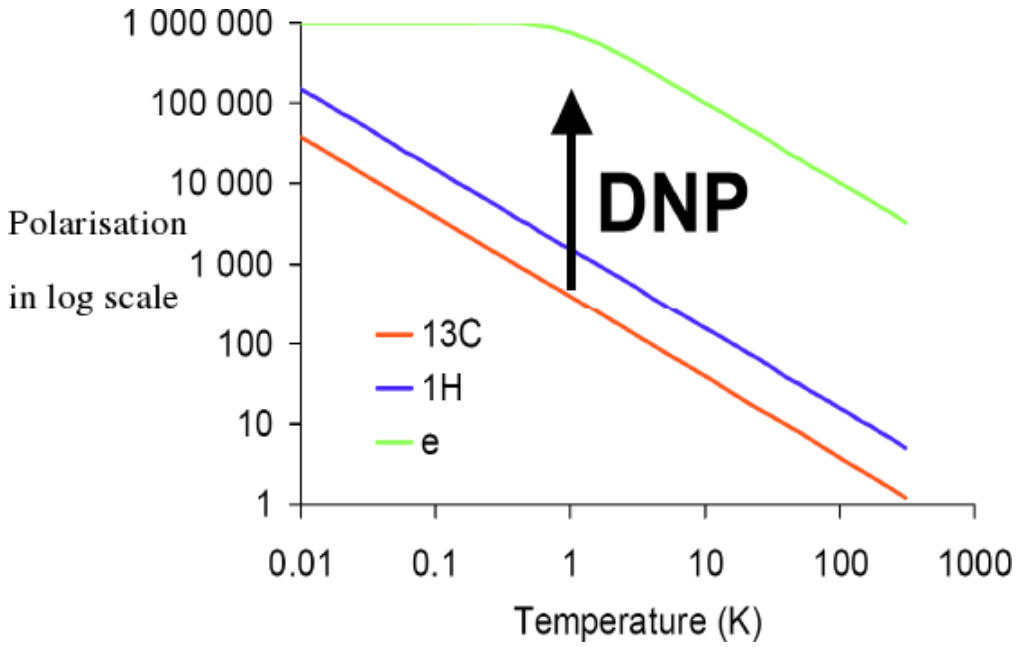

Figure 3.1: *Polarisation versus temperature (Courtesy of Walter Köckenberger). The Brillouim function is represented in the interval from 0.01 K to 1000 K in logarithmic scale.*

3.2 Glasses and crystals. Selection of glass-former

A glass-former is needed when samples are frozen, in order to prevent the presence of ice that may alter relative distances between atoms within the target molecule. Mechanical stress is caused by the 9% increase in specific volume when water passes to hexagonal ice. As commonly known ice melts at 273 K at room pressure. The crystallisation temperature is, for water, much lower (close to 230 K) [7].

In a glass, in contrast to a crystal, the constitutent molecules do not have periodic order with respect to the positions of the atoms. Some common cryoprotectants used for low temperatures (1.5 K) are glycerol, ethanol, butanol and DMSO [7]. In this project, a glass-former of 1:1 glycerol-water assured uniformity within the mixture and prevented the presence of crystaline ice. A disadvantage of this glass-forming mixture was the reduced solubility of polar chemical compounds in comparison to pure water or ethanol.

3.3 Experimental measurements

To measure the magnetisation evolution to thermal equilibrium of either ^{13}C or ^{1}H two main methods were used in the solid state, either by saturation recovery or by small flip angle excitation. The McKay probe (described in a previous chapter) was used for most of these relaxation time measurements, due to the small Q factor that it presented at the coil which yielded a short ring-down time (about 3 μs after the console dead-time). For the measurements an aliquot of 50 μl (microlitres) was loaded into a 4 mm glass tube (Wilmad) that fitted into the probe coil.

3.3.1 Saturation recovery

Saturation recovery (SR) was used for relatively short nuclear T_1 relaxation times (in comparison with the equipment temperature stability timescale, which showed a possible change of $\pm$ 0.01 K after 48 hours). The error recorded in each of the measurements within less than 10 hours was $\pm$ 0.005 K in this chapter. The magnetisation evolution was recorded by saturating the magnetisation and by measuring it with a strong pulse after a delay time that was incremented for each point until thermal equilibrium was achieved. The data points were fitted to a single exponential using Matlab programs (based on the fminsearch routine).

3.3.2 Small flip angles

In cases when the nuclear magnetisation evolved with a very long time constant (with a T_1 of several hours) the best strategy was to put as much sample as possible in the probe sample coil (to optimise signal-to-noise) and to use a train of small flip angles with a large gain. For a flip angle of 4^o an error less than 3% has been estimated [6].

Correction to small flip angle in the single exponential approximation

Experiments with some lack in sensitivity required a larger flip angle in the measurement (10^o to 15^o). It was possible to correct for larger pulses in the case of single exponential fitting. Every time a data point was collected the signal was decreased by a quantity determined by the cosine of the flip angle. This was equivalent to displacing the evolution of the magnetisation back in time. The data were fitted to a single exponential curve as a first approximation. It was possible to simulate the effect of periodical polarisation measurements on an exponential curve. By comparing the plots of the data with a simulated curve that took into account these corrections it was possible to obtain the value of the magnetisation in the approximation of a single exponential longitudinal relaxation time. By increasing the value of the flip angle the magnetisation arrived at a plateau more rapidly. The fitting was obtained with a Matlab program (fminsearch routine based) and the exponential corrections were done with Excel.

3.3.3 Nuclear relaxation in absence of paramagnetic impurities in a glassy matrix at low temperature

In the absence of paramagnetic impurities other mechanisms of relaxation that are not so efficient at 1.5 K become important in the relaxation process. Quantum tunelling in methyl groups have been demonstrated an important source of relaxation at low temperatures [8]. The presence of a quadrupolar moment and therefore the electric field gradients along with dipolar interactions between nuclear spins dominate the relaxation mechanism. Quadrupolar moments are more effective in a disordered glass than in a crystal [10]. Relaxation by quadrupolar interactions will compete with nuclear dipolar interactions depending on their relative strengths. As a reference an overall estimation of the relaxation by these factors was obtained by measuring the ^{13}C T_1 of a sample

free of paramagnetic centres.

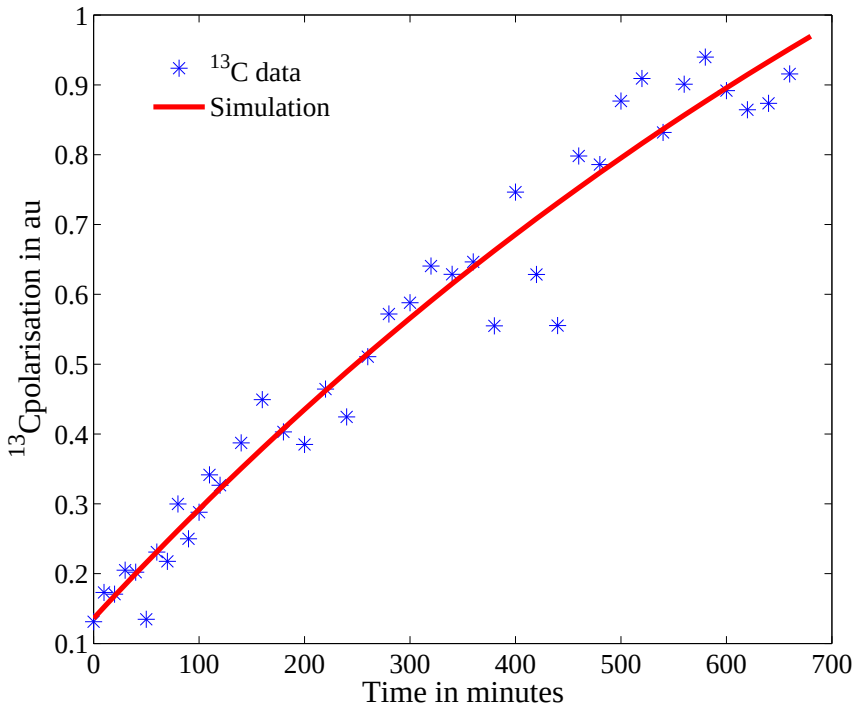

Figure 3.2: *^{13}C relaxation to thermal equilibrium in a sample of 2M labelled ^{13}C Na acetate in 1:1 glycerol-water at 1.67 K. Only the first part of the curve was measured to obtain an order of magnitude for purpose of comparison.*

As figure 3.2 shows, for a sample of 2 M [^{13}C-1] labelled Na acetate at 1.67 K, the ^{13}C T_1 relaxation time exceeded 10 hours.

3.4 Lanthanides as paramagnetic impurities

Lanthanides chelated with DTPA are good relaxing and contrast agents in magnetic resonance imaging (MRI) [5]. The selected lanthanides for tests at 1.5 K were cerium (Ce^{3+}), dysprosium (Dy^{3+}), holmium (Ho^{3+}), europium (Eu^{3+}), praseodymium (Pd^{3+}) and samarium (Sm^{3+}), all of them chelated with DTPA. Diethylene triamine pentaacetic acid (DTPA) has been used extensively in MRI as a chelating agent, especially as Gd^{3+}-DTPA [5].

Lanthanides with Kramers degeneracy in this study were Ce^{3+} (S=$\frac{1}{2}$, L=3 and J=$\frac{5}{2}$), Sm^{3+} (S=$\frac{5}{2}$, L=5 and J=$\frac{5}{2}$), and Dy^{3+} (S=2, L=6 and J=$\frac{15}{2}$). They belong to this category since their outer shell contains an odd number of electrons. The quantum number J corresponds to the ground state. The non Kramers ions used in this project were Pr^{3+} (S=$\frac{1}{2}$, L=3 and J=$\frac{5}{2}$), Eu^{3+} (S=3, L=3 and J=0) and Ho^{3+} (S=2, L=6 and J=8) [1]. Samples doped with of Ho^{3+} compounds at low temperature have presented a broad line of several GHz [4]. For Dy^{3+} it is possible to assign an overall spin of $\frac{1}{2}$ [9]. Direct processes are the main cause of electron relaxation at these temperatures, although it has been shown that Orbach relaxation contributes at temperatures of 2 K for samples with Dy^{3+} [3].

	Dy^{3+}	Ho^{3+}	Ce^{3+}	Eu^{3+}	Sm^{3+}	Pr^{3+}
Lanthanides(mM) $->$	25.3	24.0	25.0	34.0	21.0	25.0
Temperature (K)	1.67	1.66	1.67	1.55	1.57	1.68
T_1 (min)	17 $\pm$5	8 $\pm$1	85 $\pm$4	$>$ 450	$>$ 600	$>$ 425
^{13}C concentration (M) $->$	2.0	1.9	2.0	1.9	1.8	2.0

Table 3.1: ^{13}C relaxation times for samples of approximately 2 M [^{13}C-1] Na acetate in 1:1 glycerol-water. The lanthanides were chelated to DTPA. The glassy matrix was 1:1 water-glycerol.

Table 3.1 shows the T_1 relaxation times for ^{13}C spins in samples of [^{13}C-1] labelled Na acetate doped with paramagnetic chelates at low temperatures in a glassy matrix. The measuring temperature was the lowest available temperature in the stand alone polariser (SAP) in continuous helium flow mode. This measurements pointed to Ho^{3+}-DTPA and Dy^{3+}-DTPA as the most effective relaxing agents that could mediate rapid relaxation towards thermal equilibrium by the brute force polarisation strategy.

3.4.1 Dysprosium (Dy^{3+}-DTPA) as relaxation agent

Further measurements using Dy^{3+}-DTPA provided more information about the nuclear relaxation dependence on lanthanide ion concentration and tem-

perature:

	Temp.(K)				
Dy^{3+} con.		12.5 mM	17.8 mM	25.3 mM	34.2 mM
^{13}C con.(M)$->$		2.0	1.9	2.0	1.5
	1.30	—	55±6	28±4	—
	1.40	—	—	—	19 ±4
T_1 (min)	1.60	60 ±6	—	—	—
	1.62	—	30 ±5	17±5	14 ±3
	1.64	55 ±3	—	—	—
	1.68	42 ±5	—	—	—

Table 3.2: ^{13}C T_1 relaxation times (in minutes) for samples of approximately 2 M ^{13}C labelled Na acetate in 1:1 glycerol-water doped with Dy^{3+}-DTPA at different concentrations (con.). The table shows the T_1 increases as the lattice temperature decreases.

The T_1 values increased with decreasing temperature and Dy^{3+} concentration. The relaxation time almost doubled between 1.62 K and 1.30 K, within the margin of error. Proton spin T_1 relaxation times were measured on two of the samples for reference purposes.

	Temp. (K)	Dy^{3+} (12.5 mM)	Dy^{3+} (17.8 mM)
^{13}C concent.(M) $->$		2.0	1.9
	1.30	—	54 ±3
T_1 in s	1.52	—	—
	1.53	64 ±3	—
	1.62	55 ±3	33 ±2

Table 3.3: ^{1}H T_1 relaxation times (in seconds) for samples of approximately 2 M ^{13}C labelled Na acetate in 1:1 glycerol-water doped with Dy^{3+}-DTPA at different concentrations (concent.). The table shows that the T_1 (in seconds) increases as the lattice temperature decreases.

The longitudinal relaxation times for these samples were more than one order of magnitude shorter than for ^{13}C spins. This can be explained by fast spin diffusion and high gyromagnetic factor. At 1.30 K, the polarisation

achieved for ^{13}C was 0.095 % and for proton spins it was 0.26 % once in thermal equilibrium.

A diffusion barrier estimation could be obtained from the ^{13}C spectrum linewidth of the previous samples. In the limit of fast spectral spin diffusion between nuclei, and good thermal contact between electron dipolar and Zeeman nuclear baths, the ^{13}C T_1 relaxation time becomes a function of the inverse of the number of paramagnetic centres [1], [2], as shown in table 3.2. Experimentally the solubility of Dy^{3+}-DTPA did not represent a problem in 1:1 glycerol-water, but the electron nuclear dipolar interactions became a problem at certain concentrations of the lanthanide, since the linewidth was too large, or in other words, the nuclear FID decayed too quickly to be measured and distinguished from the short ring-down.

Dy^{3+} (mM)	$\Delta\omega_I$(kHz)	b(nm)	Expected T_1	Measured T_1
12.5	13	2.8	60.0	60 ±6
17.4	17	2.61	34.9	30 ±5
25.3	22	2.43	19.4	17 ±5
34.4	30	2.22	11.0	14 ±3

Table 3.4: Data for samples of [^{13}C-1] labelled Na acetate with Dy^{3+}-DTPA. The relaxation time for 12.5 mM Dy^{3+}-DTPA was taken as a reference, since the electron T_2 was necessary for the calculations. The diffusion barrier (b) and the T_1 relaxation times values were obtained with equation 1.78 in chapter 1.

Within experimental error the nuclear T_1 was shown to be a function of the inverse of the concentration of lanthanide ions.

3.4.2 Holmium (Ho^{3+}-DTPA) as a relaxation agent

T_1 relaxation times (table 3.5) were measured in three samples containing different concentrations of Ho^{3+}-DTPA, with a concentration close to 2 M of ^{13}C labelled acetate in a solvent of 1:1 glycerol-water. The data in table 3.1 showed that Ho^{3+}-DTPA could act as an excellent relaxation agent at low temperatures. With 24 mM Ho^{3+} thermal equilibrium was reached for the ^{13}C

polarisation in less than 40 minutes at 1.66 K. Further data for the nuclear longitudinal relaxation times for proton spins are summarised in table 3.6.

	Ho^{3+} (24.0 mM)	Ho^{3+} (8.6 mM)	Ho^{3+} (3.8 mM)
^{13}C concent. $->$	1.9 M	1.7 M	2.0 M
Temp. (K)			
1.34	—	—	120 ±8
1.45	—	—	92 ±4
1.66	8 ±1	—	—
1.67	—	28 ±3	—
2.00	5.0 ±0.6	—	—
4.25	0.14 ±0.09	—	1.0 ±0.1

Table 3.5: ^{13}C T_1 relaxation times (in minutes) for samples of approximately 2 M [^{13}C-1] labelled Na acetate in 1:1 glycerol-water doped with Ho^{3+}-DTPA at different concentrations (concent.). As the table shows, the nuclear T_1 increased as the lattice temperature decreased.

For the 8.6 mM concentration of Ho^{3+}-DTPA at 1.67 K a shorter T_1 (almost half) was achieved than that obtained for Dy^{3+}-DTPA at 12.5 mM and 1.68 K.

	Ho^{3+} (24.0 mM)	Ho^{3+} (8.6 mM)	Ho^{3+} (3.8 mM)
^{13}C concent. $->$	1.9 M	1.7 M	2.0 M
Temp.(K)			
1.34	—	—	150 ±15
1.66	16.0 ±0.2	—	—
1.67	—	38 ±1	—
4.25	0.5 ±0.2	1.5 ±0.2	2.8 ±0.15

Table 3.6: ^{1}H relaxation times (in seconds) for samples of approximately 2 M [^{13}C-1] labelled Na acetate in 1:1 glycerol-water doped with Ho^{3+}-DTPA at different concentrations (concent.).

The T_1 relaxation time constant for ^{1}H spins was less than one order of magnitude shorter than for ^{13}C spins, as with Dy^{3+}. Previous studies reported a large electron bandwidth for Ho^{3+} at low temperature [4].

3.4.3 Lyophilised samples of ^{13}C labelled Na acetate with Ho^{3+}-DTPA

An alternative approach to samples in a glassy state was considered in this project using lyophilisation of the [^{13}C-1] acetate with Ho^{3+}-DTPA samples. Since the solvent is removed at room temperature, the lanthanide ions are in closer contact with the targeted ^{13}C nuclei. The initial concentrations prior to lyophilisation were 20 mM, 6 mM and 2 mM Ho^{3+}-DTPA. In this case there were no (or very few) solvent proton spins to mediate between the Ho^{3+} and the ^{13}C nuclei. ^{13}C T_1 relaxation times were measured and summarised in table 3.7.

Temperature (K)	Ho (20.0 mM)	Ho (6 mM)	Ho (2 mM)
1.60	—	80 ±7	—
1.62	13 ±1	—	—
1.67	—	—	67 ±2
4.25	—	—	33 ±5

Table 3.7: ^{13}C T_1 relaxation times measurements (in minutes) for samples of lyophilised [^{13}C-1] Na acetate doped with Ho^{3+}-DTPA in different concentrations.

Table 3.7 shows that the T_1 values for the powder samples were longer than for 24 mM Ho^{3+} in a water-glycerol glass. A crude estimation of the diffusion barrier gives values between 1 and 4 nm.

3.5 Conclusions

The presence of certain paramagnetic lanthanide ions produced a substantial decrease in the nuclear longitudinal relaxation time of the nuclear ^{13}C spins in samples of acetate in a glassy matrix of glycerol-water at low temperatures (1.5 K). Of the lanthanides tested, the most effective for this purpose were Ho^{3+} and then Dy^{3+} resulting in ^{13}C T_1 values of 8 and 17 minutes respectively at concentrations of $\approx$ 20 mM in comparison to the more than 10 hours

without lanthanide doping. Some further measurements on proton spins revealed that they relaxed faster than ^{13}C spins at temperatures close to 1.5 K. The relaxation time was one to two order of magnitude shorter in ^{1}H spins than in ^{13}C spins when paramagnetic centres were added. The temperature and the concentration of Ho^{3+}-DTPA or Dy^{3+}-DTPA determined the nuclear relaxation time. At higher temperatures (4.2 K) the relaxation times for the two spin species became closer. This points to electron relaxation mechanisms other than the direct process (Orbach or Raman electron relaxation) [3].

T_1 measurements were also performed with powder samples obtained after lyophilising [^{13}C-1] labelled Na acetate with Ho^{3+}-DTPA in aquous solution. In this kind of sample the lanthanide was in closer contact with the ^{13}C spin. This strategy makes it possible to accommodate a larger amount of sample in a given volume. The relaxation generated by Ho^{3+}-DTPA was broadly similar to that with the glassy samples. These results point to the possibility of using brute force polarisation as a technique to generate highly polarised ^{13}C systems for dissolution experiments.

Bibliography

[1] A. Abragam and B. Bleaney. *Electron paramagnetic resonance of transition ions*. 1970.

[2] J. H. Ardenkjaer-Larsen, S. Macholl, and H. Johannesson. Dynamic nuclear polarisation with trityls at 1.2 K. *Appl. Magn. Reson.*, 34:509–522, 2008.

[3] R. W. Bierig, M. J. Weber, and S. I. Warshaw. Paramagnetic resonance and relaxation of trivalent rare-earth ions in calcium fluoride. II spin-lattice relaxation. *Phys. Rev.*, 134:6A, 1964.

[4] N. Bontemps and J. C. Rivoal. Ground-state spectroscopic properties of an amorphous holmium aluminosilicate exhibiting spin glass properties. *J. Phys.C: Sol. St. Phys.*, 15:1301–1318, 1982.

[5] W-J. Chu and G. A. Elgavish. Gadolinium and Dysprosium Chelates of DTPA-amide-dextran: Synthesis, ^{1}H NMR Relaxivity, and induced ^{23}Na NMR shift. *NMR in Biomed.*, 8:159–163, 1995.

[6] B. Cowan. *Nuclear Magnetic Resonance and Relaxation*. Cambridge University Press (Cambridge), 1997.

[7] E. F. Garman and T. R. Schneider. Macromolecular cryocrystrallography. *J. Appl. Cryst*, 30:211–237, 1997.

[8] A.J. Horsewill. Quantum tunnelling in the hydrogen bond. *Progr. Nuc. Mag. Res. Spect.*, 52:170196, 2008.

[9] H. Jager, A. Koch, V. Maus, H. W. Spiess, and G. Jeschke. Relaxation-based distance measurements between a nitroxide and a lanthanide spin label. *J. Mag. Res.*, 194:254–263, 2008.

[10] D. Wolf. *Spin temperature and nuclear spin relaxation in matter: basic principles and applications*. Oxford University Press (Oxford), 1979.

Chapter 4

Dynamic Nuclear Polarisation (DNP)

Dynamic Nuclear Polarisation was introduced in chapter 1 as a strategy to enhance the nuclear population differences in comparison to thermal levels. In this chapter, results of experiments using DNP at low temperatures (1.5 K) and a magnetic field of 3.35 T in a stand alone polariser (SAP) are summarised. Two different free radicals (TEMPO or 2,2,6,6 tetramethylpiperidine 1 oxyl and Ox63 [3]) (figure 4.1) were used to enhance the nuclear polarisation, either for ^{1}H or for ^{13}C spins. Theoretical explanations of several mechanisms in DNP were presented in chapter 1. In this chapter two models proposed by Goldman [8] are applied in the validity limit of high spin temperature.

4.1 Experimental

The McKay probe (chapter 2, section 2.2.3) was used in all the experiments for ^{1}H and ^{13}C spin data acquisition, unless otherwise specified. The samples were stored in a 4 mm diameter sample tube (Wilmad LabGlass, UK). This tube fitted in the 4 mm inner diameter saddle coil of the McKay probe. It was kept in position with a former made of macor that surrounded the saddle coil. This former allowed irradiation through two windows. The ^{15}N data

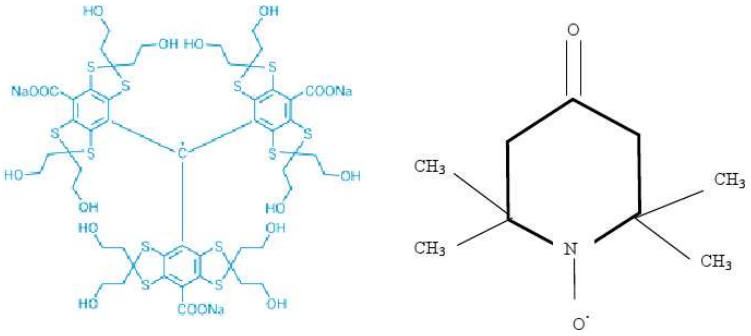

Figure 4.1: *Ox63 trityl (left) [11] and TEMPO (right) free radical structures.*

were obtained with a specially designed probe. The flip angle used for data acquisition in build-up and T_1 relaxation time measurements was less than 3^o for ^{1}H detection which provided sufficient sensitivity ($SNR > 2$). It was also less than 3^o in all the experiments involving ^{13}C and ^{15}N detection. For flip angles of less than 4^o an error of less than 3% was estimated [5]. The data were fitted with a Matlab program based on the routine fminsearch.

Glycerol as a glassformer [6] and water in 1:1 proportion was used in the experiments because of the suitability of this combination for biomedical applications [13]. Dimethyl sulfoxide (DMSO) also acts as a good cryoprotectant [6]. Acetate or urea are involved cell metabolism, and the study of these molecules in solid state DNP NMR is relevant for future in vivo applications [13].

The power levels were kept to the maximum which translated into 200 mW output from the Elva source, although the sample did not experience the same power deposition in different probes due to differences in shielding. Because of different irradiation conditions, different enhancement factors were obtained with different probes.

4.2 DNP using Ox63 Trityl at 3.35 T and low temperatures (1.5 K)

Trityl radicals for DNP at low temperature have proved to be very effective for low gyromagnetic ratio nuclear spins [2], [3] in a frozen glassy matrix. They enclose the free radical in the middle of the molecule of the triphenyl methyl type [3]. The unpaired electron presents a narrow resonance line with a typical linewidth between 15 and 60 MHz. This line can be approximated by a Gaussian lineshape [8], or a mixture of Gaussian and Lorentzian (Voight) lineshapes [3].

The trityl radical has a narrower lineshape than the ^{1}H spin Larmor frequency (142.6 MHz at 3.35 T). Therefore, for trityl the solid effect becomes the main mechanism of DNP for ^{1}H spins. A combination of the solid effect and thermal mixing was expected for lower gyromagnetic ratio nuclei like ^{13}C or ^{15}N [8]. Figure 4.2 shows the line of Ox63 trityl in a sample of 1M [1-^{13}C]-formate and 15 mM trityl in 1:1 glycerol-water (courtesy of Josef Granwehr):

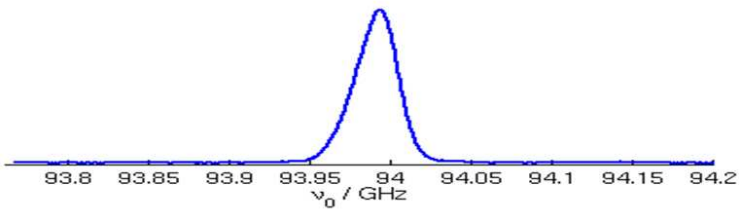

Figure 4.2: *Ox63 trityl free radical lineshape obtained with LOngitudinally DEtected Spin Resonance (LODESR) in a sample of 1M ^{13}C-formate 15 mM trityl in 1:1 glycerol-water (courtesy of Josef Granwehr).*

4.2.1 The solid effect

The solid effect (SE) is the main polarisation transfer mechanism in cases where the electron resonance linewidth $\delta\omega_e$ is much narrower than the nuclear Larmor

frequency ω_n. The ^{1}H spins in a sample of 7 M ^{15}N labelled urea doped with 15 mM Ox63 trityl in 1:1 glycerol-water showed a maximum enhancement of 8 (figure 4.3) over thermal equilibrium. The linewidth of the proton spectrum was typically in the range of 80 ±20 kHz in a fully protonated sample. The DNP enhancement spectrum (figure 4.3) was obtained by saturating the ^{1}H nuclei first followed by irradiating the sample with microwaves at a frequency close to the electron resonance Larmor frequency (which in this case was approximately 93.975 GHz) for typically 4 minutes. After this time an excitation $\frac{\pi}{2}$ pulse was applied to detect how much nuclear magnetisation was generated during the DNP period. The experiment was repeated covering a frequency range around the electron Larmor frequency (93.79 to 94.25 GHz for enhancement of protons, typically). For a microwave frequency of $\omega = |\omega_e| - |\omega_I|$ zero quantum transitions were excited without inducing double quantum transitions as explained in chapter 1. On the other hand, double quantum transitions were excited by irradiating at a microwave frequency $\omega = |\omega_e| + |\omega_I|$. In addition, secondary peaks from another pathway, possibly via the ^{15}N spin system, could be seen close to the centre of the electron resonance frequency [4]. The build-up and nuclear relaxation times were 41 and 62 minutes respectively at the enhancement frequency of 93.83 GHz. To probe the validity of the SE model outlined in chapter 1 the differential equations (chapter 1, 1.87, 1.88, 1.89) had to be solved for the steady state. For the solution, some approximations were made. The lattice inverse spin temperature β_L and also the terms which were proportional to $C_S W_+^2$ were neglected from the equations, since they were very small (smaller than 1 % compared to the other terms). The solution for the nuclear inverse spin temperature α_I was:

$$\alpha_{I\mp} = \pm\beta_L \frac{\omega_S}{\omega_I} \frac{C_S T_I W_\mp}{1 + W_\mp (C_S T_I + C_I T_S + \frac{\Gamma^2}{D^2} T_D)} \tag{4.1}$$

where $W_\mp$ represents the transition probability, C_S and C_I were defined as $C_I = \frac{N_I}{N_I + N_S}$ and $C_S = \frac{N_S}{N_I + N_S}$, $\alpha_L = \beta_L \frac{\omega_S}{\Delta}$, β_L is the lattice inverse spin temperature, T_I and T_S are the spin lattice relaxation times for nuclei and

electrons, D is the local field frequency, T_D is the spin lattice relaxation time of the dipolar bath and $\Gamma = \omega_I - \Delta = \omega_I - \omega_S + \omega$ with ω being the irradiation frequency [8].

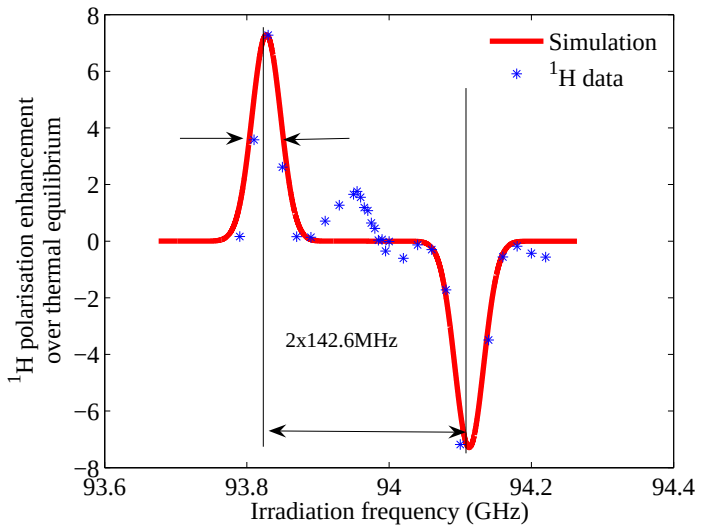

Figure 4.3: *Illustration of the solid effect in a sample of 15 mM Ox63 trityl with 7 M ^{15}N labelled urea in 1:1 glycerol-water at 1.59 K and 3.35T. The solid effect model was fitted to the data points. The red line represents the simulation using the equations of the well resolved solid effect model by Goldman.*

In the model there were some parameters that had to be estimated since no precise electron resonance data for this sample were available. The transition probability was taken as a Gaussian with a linewidth of 38 MHz and normalised height to a factor of $1.52 \cdot 10^{-2}$ (i.e. the value of the maximum of the transition probability) obtained by fitting equation 4.1 to the data.

The parameters C_I and C_S were set to 1.0 and $2\text{x}10^{-4}$ respectively (the concentration of paramagnetic centres was 15 mM and for ^{1}H was taken to be 110 M as a good estimation). The spin lattice electron and dipolar relaxation times T_S and T_D were both set to 1 s. The model was robust enough to cope with variations of these values in a range from 10 ms to 10 s resulting

in variations of enhancement of less than 5%. The relaxation time for T_S was previously reported to be approximately 1 s [3] with an error less than 50%, in a sample of trityl and pyruvic acid in similar conditions. The local field D was taken as the linewidth of the Gaussian. This model showed a larger dependence on C_S, the maximum enhancement changing with the inverse of C_S, and on the transition probability linewidth. A polarisation of 1 $\pm$ 0.5% was achieved experimentally, which is within the limit of validity of the approximation of high temperature. The agreement between theory and experimental data points was reasonable at the two frequencies $\omega_e \pm \omega_n$. The DNP curve showed two antisymmetric peaks separated by twice the nuclear Larmor frequency. The low enhancement obtained pointed to a good thermal contact with the lattice in this kind of sample, and made trityl radicals unsuitable for ^{1}H polarisation enhancement at low temperatures. The linewidth of the anti-symmetric enhanced peaks was 45 $\pm$ 10 MHz.

4.2.2 Thermal mixing

Trityl radicals have been used to obtain large polarisations (40% or more, [2]) in low gyromagnetic ratio nuclear spins at 3.35 T and temperatures close to 1.2 K [2]. In cases where the electron linewidth is comparable to the nuclear Larmor frequency, a combination of SE and thermal mixing (as the transitions which were responsible for it then became allowed) is responsible for the DNP process [8]. This was the case in samples where the trityl electron resonance linewidth was around 30 MHz and the ^{13}C and ^{15}N nuclear Larmor frequencies were 35.88 MHz and 14.5 MHz respectively. The DNP enhancement curve showed a characteristic antisymmetric lineshape. The steady state solutions for Goldman's model of the unresolved solid effect were obtained by setting the differential equations 1.90, 1.91 and 1.92 in chapter 1 equal to zero for the three inverse spin temperatures α_I, α_S and β corresponding to the nuclear bath and the electron Zeeman and dipolar baths. The solutions [8] are shown in equations 4.2, 4.3 and 4.4:

$$\alpha_I = \frac{\beta_L + C_S(\frac{\Delta}{\omega_I})(W_+ - W_-)T_I(\alpha_S - \beta) + (C_S(W_+ + W_-) + U)T_I\beta}{1 + T_I(C_S(W_+ + W_-) + U)} \quad (4.2)$$

$$\alpha_S = \beta_L \frac{\omega_S}{\Delta} \frac{1 + W_0 T_D \frac{\Delta^2}{C_I D^2}}{1 + W_0(T_S + T_D(\frac{\Delta^2}{C_I D^2}))} \quad (4.3)$$

$$\beta = \beta_L \frac{\omega_S}{\Delta} \frac{W_0 T_D \frac{\Delta^2}{C_I D^2}}{1 + W_0(T_S + T_D(\frac{\Delta^2}{C_I D^2}))} \quad (4.4)$$

where it should be noted that U is the transition probability for thermal mixing with the electron dipolar thermal bath.

Thermal mixing in a sample of [^{13}C-1] Na acetate and trityl in 1:1 glycerol-water

The ^{13}C DNP enhancement curve for a sample of 1.54 M [^{13}C-1] Na acetate doped with 13.5 mM Ox63 trityl in 1:1 glycerol-water is shown in figure 4.4.

For the fitting a Gaussian was used for the transition probability (W_+, W_- and W_0) with a width of 38 MHz. The Gaussian lineshapes were normalised to 1 and multiplied by a factor of 6.5x10^{-3}. The simulation reproduced the antisymmetric shape of the curve. The separation between the two extrema was 71 MHz, which corresponds to twice the ^{13}C Zeeman frequency. A T_1 of 270 minutes was measured and the build-up time was 141 minutes for ^{13}C spins when an irradiation frequency of maximum nuclear enhancement (close to 93.95 GHz) was used (figure 4.4). The T_S was set to 1 s [3]. The T_D was set to 1 s although this model exhibited a large tolerance of this parameter between 1 ms and 10 s. The values for C_I and C_S were taken as 1 and 0.0135 respectively. The probability U was taken as 2.0 $\cdot 10^{-3}$ s^{-1} for a maximum value of W_+ of 6.5 $\cdot 10^{-3}$ s^{-1}. There was a strong dependence of the maximum enhancement on the probabilities W_+, W_-, W_0 and U. The model, with this set of input parameters, predicted an antisymmetrical curve with two peaks (one maximum and one minimum) that fitted the data. The maximum polarisation

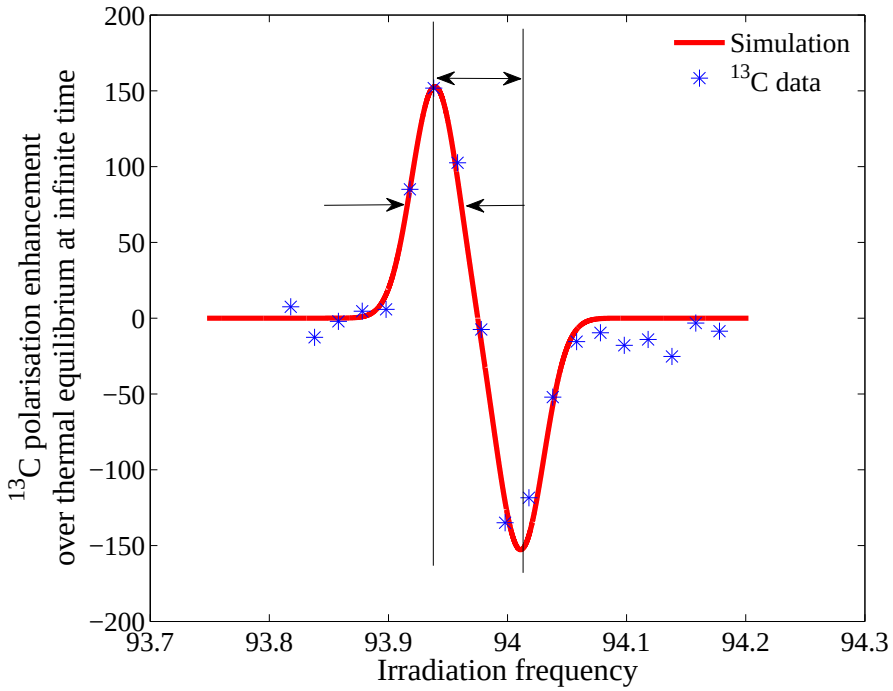

Figure 4.4: *^{13}C DNP enhancement curve for a sample of 1.54 M [$^{13}C-1$] Na acetate with 13.5 mM trityl in 1:1 glycerol-water at 1.67 K.*

achieved experimentally was at this temperature and corresponded to this enhancement of 9.0 ± 3.0 %.

Thermal mixing in a sample of ^{15}N urea and trityl

The peak to peak separation in a DNP enhancement spectrum for ^{15}N in a sample of 1.78 M ^{15}N urea in DMSO was 32 MHz (figure 4.6).

The values of T_D and T_S were taken as 1 s for figure 4.7 [3]. Again they could range from 1 ms to 10 s without altering the DNP enhancement spectrum significantly (less than 5% variation in the enhancement). The transition probabilities W_+, W_-, W_0 were also taken as Gaussian lineshapes, multiplied by a factor ($5.0{\cdot}10^{-3}$) that incorporated the contribution from the irradiation

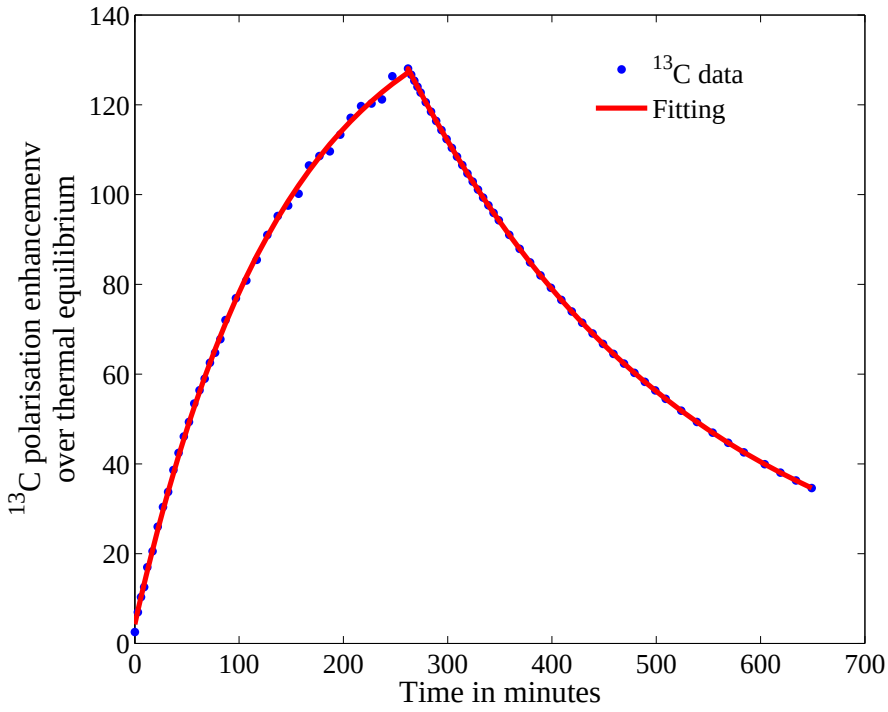

Figure 4.5: *Build-up and T_1 for a sample of 1.54 M [^{13}C-1] acetate with 13.5 mM trityl in 1:1 glycerol at 1.67 K with a DNP irradiation frequency of 93.95 GHz. After more than 200 minutes of build-up the irradiation was stopped to measure the spin lattice relaxation time T_1.*

magnetic field. The linewidth of this transition probability was set to 12 MHz. The transition probabiliy U was set to a constant value of $2.8{\cdot}10^{-3}$. The values for C_I and C_S were 1 and $7.3{\cdot}10^{-3}$. Changing the value for the transition probabilities the fitted curve could be scaled up or down, which introduced a degree of freedom. The build-up time recorded using 93.95 GHz as microwave irradiation frequency was 49 minutes and the T_1 was 171 minutes at 1.48 K (figure 4.6). The obtained enhancement of 78 yielded a polarisation of 5.6± 1.0 % of the ^{15}N spin system.

The distance between the peaks (32 MHz) pointed to a smaller transition

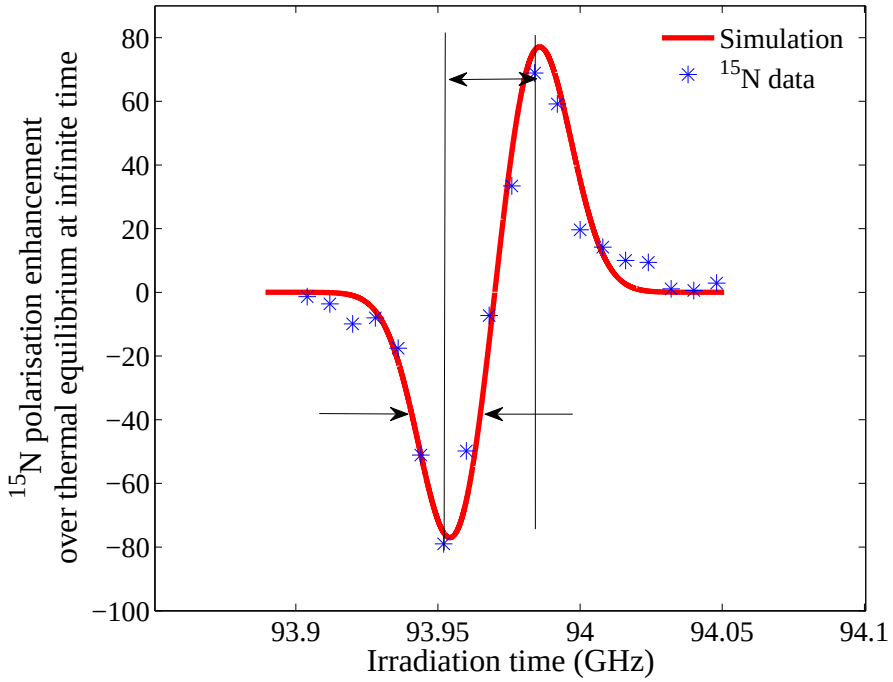

Figure 4.6: *^{15}N DNP enhancement spectrum in a sample of 1.78 M ^{15}N labelled urea doped with 13 mM Ox63 trityl in DMSO. The inverted pattern shows the different sign in the gyromagnetic ratio (negative in ^{15}N and positive in ^{13}C and proton spins).*

probability which at the same time led to a narrower electron resonance line in DMSO. In a sample of 7 M ^{15}N labelled urea in 1:1 glycerol-water this distance peak to peak was around 50 MHz.

DNP data for several compounds doped with the trityl radical are shown in tables 4.1 and 4.2. To obtain the largest enhancements the irradiation frequency for maximum enhancement was selected. The nuclear polarisation was then measured with small flip angles.

Large enhancements were obtained for ^{15}N and ^{13}C spins. The enhancements obtained for ^{13}C were lower than stated in the literature (typically 200 or 300 over thermal equilibrium) [2]. Either 1:1 glycerol-water or DMSO based

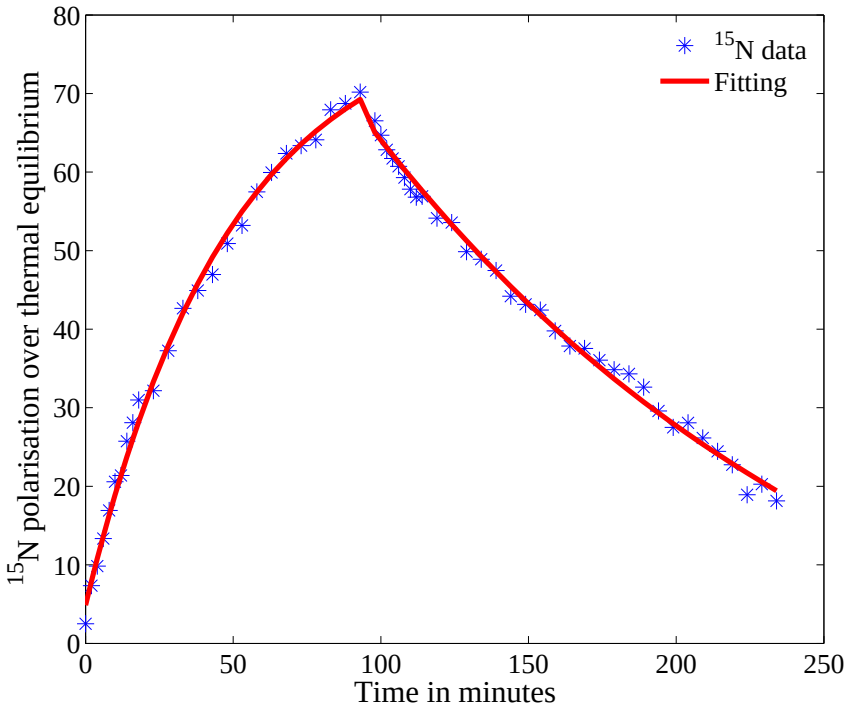

Figure 4.7: *Build-up and T_1 for a sample of 1.78 M ^{15} N urea with 13 mM trityl DMSO at 1.48 K with a DNP irradiation frequency of 93.95 GHz. After 95 minutes of build-up the irradiation was stopped to measure the spin lattice relaxation time T_1.*

glasses showed enhancements close to two orders of magnitude. A typical time of one to several hours was needed to achieve the measured enhancement (Table 4.1).

In the model of Goldman for the unresolved solid effect the thermal mixing included an interaction between the dipolar reservoir and the ^{13}C thermal bath. It was possible to illustrate the absence of thermal contact between the proton and the ^{13}C thermal baths in the laboratory frame. To prove the absence of this thermal contact the ^{13}C build-up was recorded starting from saturation of both ^{1}H and ^{13}C spins. In one set of experiments the ^{1}H were periodically

Sample	Trityl conc.	τ_{DNP}	T_1	Temp (K)
^{1}H in 7 M ^{15}N urea in 1:1 glycerol-water	15 mM	41±2	62± 2	1.59
^{1}H in 1.9 M ^{13} Na formate in 1:1 glycerol-water	18 mM	81± 3	177± 4	1.54
^{13}C in 1.9 M ^{13} Na formate in 1:1 glycerol-water	18 mM	80± 3	198± 4	1.54
^{13}C in 1 M ^{13} Na Acetate in 1:1 glycerol-water	18 mM	62± 3	160± 5	1.58
^{13}C in 1.54 M ^{13} Na Acetate in 1:1 glycerol-water	13.5 mM	141± 4	270± 8	1.67
^{15}N in 7 M ^{15}N urea in 1:1 glycerol-water	15 mM	35± 1	108± 4	1.59
^{15}N in 1.78 M ^{15}N urea in DMSO	13 mM	49± 2	171± 4	1.48

Table 4.1: Polarisation build-up times τ and T_1 relaxation times in minutes in samples doped with trityl with several concentrations (trityl conc.) in 1:1 glycerol-water.

saturated (a 90^o pulse of 10 μs was applied every 333 ms). Hence, the ^{13}C polarisation build-up was measured either in the presence or in the absence of proton polarisation. Since the T_2 of proton spins was typically less than 20 μs, it was assumed that the proton magnetisation was completely saturated during the experiment with saturating pulses. The experimental results are shown in figure 4.8.

The two curves show an identical time course from which it is possible to conclude that cross relaxation between proton and ^{13}C spins is not a relevant mechanism. However, some thermal mixing was observed in figure 4.3.

4.3 Thermal mixing with TEMPO

Samples doped with TEMPO free radical have presented electron linewidths of about 600 MHz, far more than the proton Larmor frequency at 3.35 T (142.6 MHz). The principal values of the g-tensor are (2.0094, 2.0065, 2.0017) [12].

Sample	ϵ
^{1}H in 7 M ^{15}N urea in 1:1 glycerol-water	8 ± 4
^{1}H in 1.9 M ^{13} Na formate in 1:1 glycerol-water	5 ± 2
^{13}C in 1.9 M ^{13} Na formate in 1:1 glycerol-water	100 ± 50
^{13}C in 1 M ^{13} Na Acetate in 1:1 glycerol-water	80 ± 20
^{13}C in 1.54 M ^{13} Na Acetate in 1:1 glycerol-water	150 ± 50
^{15}N in 7 M ^{15}N urea in 1:1 glycerol-water	110± 25
^{15}N in 1.78 M ^{15}N urea in DMSO	80 ± 20

Table 4.2: Enhancements in samples doped with trityl with several concentrations (continuation of table 4.1) in 1:1 glycerol-water.

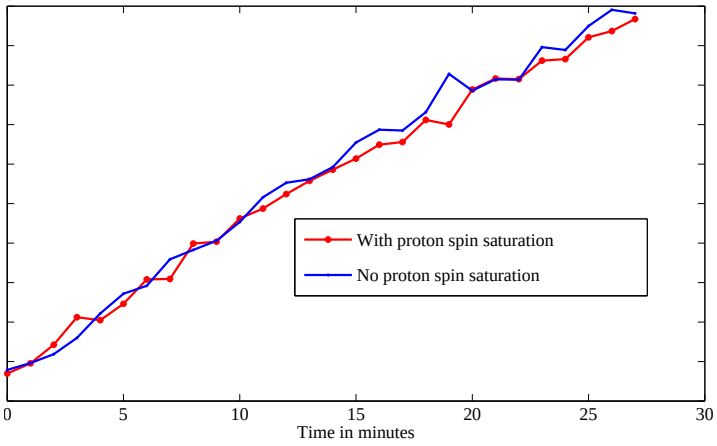

Figure 4.8: *^{13}C build-up curves in a sample of [1-^{13}C] Na acetate 1.54 M with 13.5 mM trityl in 1:1 glycerol-water at 1.67 K and with 93.95 GHz irradiation frequency. Diamonds show the ^{13}C build-up data with periodic 90º pulses on the ^{1}H channel every 333 ms (the proton magnetisation was saturated during all this build-up curve). The star data shows the same experiment but without proton saturation. Only the first part of the curve was recorded to obtain an order of magnitude for comparison reasons.*

In contrast to trityl, TEMPO is inexpensive and easy to obtain commercially (Sigma Aldrich, UK). In this kind of sample the enhancement versus EPR irradiation frequency showed a pronounced tolerance (about 100 MHz in the DNP enhancement spectrum) in the irradiation frequency for the maximum enhancement. A typical lineshape of TEMPO was measured by Josef Granwehr using LODESR (figure 4.9).

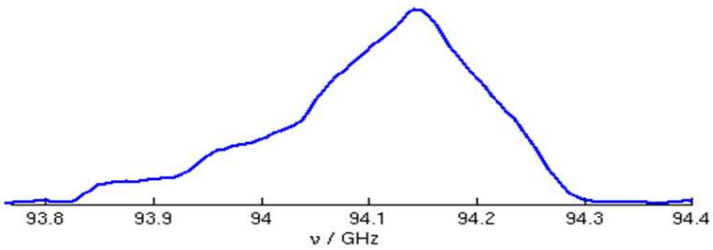

Figure 4.9: *TEMPO electron lineshape obtained in a sample of 20 mM TEMPO at 1.5 K (courtesy of Josef Granwehr).*

A DNP enhancement spectrum of a sample with 60 mM TEMPO in 1:1 glycerol-water is shown in figure 4.10.

From this spectrum the microwave irradiation frequency for maximum enhancement was chosen to be 93.95 GHz. Build-up and T_1 times and DNP enhancements ϵ were measured for different concentrations of TEMPO using the same solvent (1:1 glycerol-water) and are summarised in table 4.3.

TEMPO Concentration	100 mM	60 mM	20 mM	10 mM
τ_{DNP} (s)	60 ±10	120 ± 20	120 ±20	1380 ±60
T_1 (min)	13±1	21±1	37±2	50±2
Enhancement ε	30 ± 10	21 ±5	19 ±5	5 ±1.0
Polarisation %	7.2 ± 2	4.5 ± 1.1	4.1 ±1.1	1.1±0.3

Table 4.3: *Proton spin build-up τ, relaxation T_1 times, enhancements and polarisation data for samples of TEMPO in 1:1 glycerol-water measured at 1.53 K.*

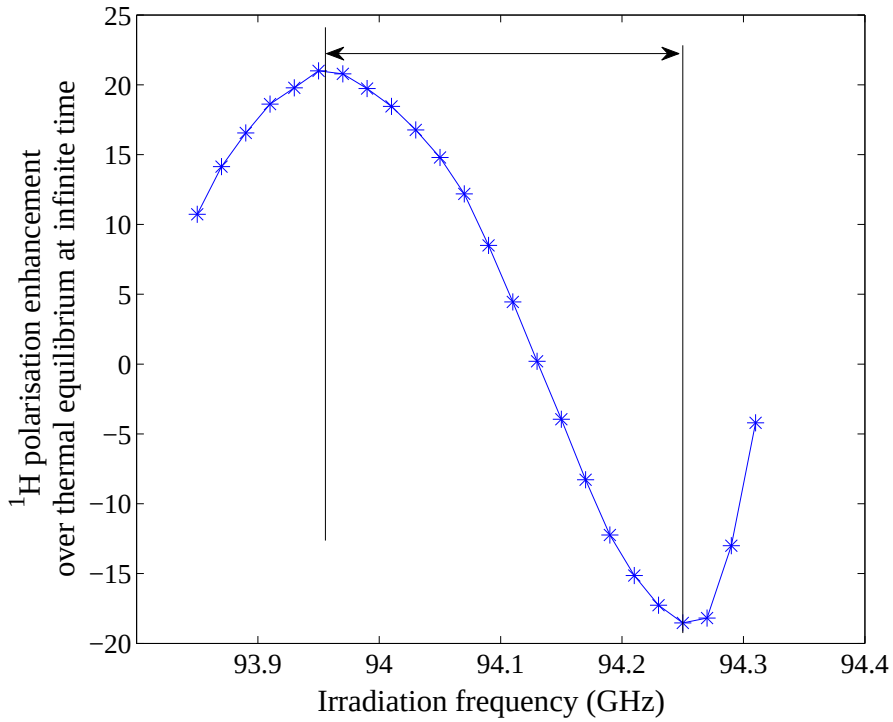

Figure 4.10: *Proton spin DNP enhancement spectrum for a sample of 60 mM TEMPO in 1:1 glycerol-water at 1.53 K (no simulation is included in this figure). The difference between frequencies for maximum and minimum was 150 MHz approximately.*

Experimentally it was difficult to disolve TEMPO in 1:1 glycerol-water with a concentration of 100 mM. The sample temperature was therefore increased to 30^o C . The sample was shaken periodically until homogeneity of colour was achieved. Table 4.3 shows that the shortest build-up time corresponded to the sample with highest concentration (100 mM). This sample had also the highest enhancement ϵ. From the data it was concluded that the [^{13}C-1] Na acetate in 1:1 glycerol-water needed to be dissolved with the highest concentration of TEMPO to achieve the shortest build-up time and highest enhancement.

4.3.1 Samples with TEMPO and [^{13}C-1] Na acetate

The interaction between different Zeeman reservoirs was studied using a sample containing a concentration close to 1 M [^{13}C-1] Na acetate, 100 mM TEMPO in 1:1 glycerol-water. Atsarkin et al [4] defined the heat capacities as:

$$c_I = \frac{d}{d\alpha_I} < \hat{H}_I >= \frac{\hbar^2 n_I I(I+1)\omega_I^2}{3k_B} \tag{4.5}$$

$$\tilde{c}_S = \frac{d}{d\beta} < \tilde{H}_S >= \frac{\hbar^2 n_S I(S+1)\Delta_p^2 I^2}{3k_B} \tag{4.6}$$

where n_I and n_S are in this case the density of I and S spins. I and S are the spin number of each spin species and k_B is the Boltzmann constant. The electron heat capacity in the rotating frame $\tilde{c}_S$ depends on the irradiation frequency $\Delta_p = \pm\omega_I$.

This concept of heat capacity involves the Larmor frequency and the number of spins, or in other words, the strength of the dipolar interaction for this type of spin. $\hat{H}_I$ corresponds to the Hamiltonian of the proton spins in the laboratory frame and $\tilde{H}_S$ is the Hamiltonian for the electron dipolar reservoir in the rotating frame. In the description of DNP using the spin temperature model, the nuclear spins are assumed to form several thermal baths which may be in thermal contact. One thermal bath with a larger heat capacity in good thermal contact with the other reservoirs may dominate the evolution towards the final nuclear spin temperature. The good thermal contact between ^{1}H and ^{13}C nuclear Zeeman reservoirs and the electron dipolar reservoir can be demonstrated by the DNP enhancement spectra of ^{1}H and ^{13}C polarisations (figure 4.11). The 100 mM TEMPO concentration results in an average distance of 6 nm between two electrons. The strong hyperfine field of the electrons leads to the strong magnetic field gradients in the sample which could lead to thermal mixing between ^{13}C and ^{1}H spins.

The irradiation spectrum for both ^{13}C and proton spins for a sample of 1.58 M [^{13}C-1] labelled acetate doped with 84.4 mM TEMPO in 1:1 glycerol-water is given in figure 4.11.

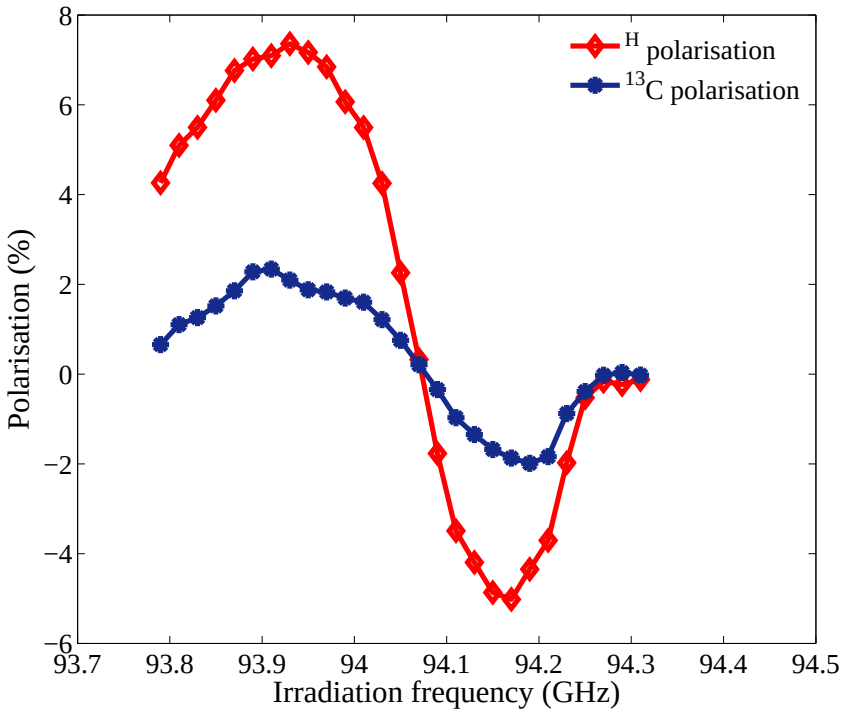

Figure 4.11: *DNP enhancement spectra of a sample of 84.4 mM TEMPO with 1.58 M [^{13}C-1] labelled acetate in 1:1 glycerol-water. The maximum enhancement for both types of spins was 38 over the Boltzmann population at 1.77 K.*

The DNP enhancement spectra of both ^{1}H and ^{13}C polarisations have the same characteristic shape and distance between maximum and minimum at the same microwave frequencies. This is due to a large electron resonance bandwidth [10] and the strong g-anisotropy and hyperfine interactions. Thermal mixing is the main mechanism of polarisation enhancement [7], [9], [12].

By decreasing the heat contact between the lattice and the ^{1}H Zeeman reservoir it is possible to obtain larger enhancements. This could be done by using deuterated water and glycerol instead of fully protonated water and glycerol [1], [12]. For the measurement of polarisation enhancement a microwave

frequency of 93.95 GHz was selected. Two solvents were used: 1:1 glycerol-water and the same proportion with fully deuterated glycerol and D_2O. With sample deuteration or with a solute increase a smaller heat capacity for the proton spin reservoir could be achieved. For the ^1H polarisation the build-up time could be fitted well by a single exponential, but the ^{13}C polarisation time constant showed multiexponential behaviour when both the ^1H and the ^{13}C spin systems were polarised both from the state of saturation. The ^{13}C build-up and relaxation times were fitted to a single exponential for reference purposes.

Temperature (K)	1.71	1.57	1.77	1.72
TEMPO (mM)	91	96	84.4	93
^{13}C Na acetate (M)	1.54	2.3	1.58	0.236
Matrix deuteration (%)	100	100	0	0
τ_H (min)	1.5 ± 0.2	2.3 ± 0.2	6.3± 0.3	4.6± 0.3
τ_{13C} (min)	15± 3	15± 3	19± 3	18± 3
T_{1H} (min)	15± 1	22± 1	18± 1	13± 1
T_{13C} (min)	50± 4	63± 5	32± 4	45± 4
Enhancement (^1H)	100± 20	60± 30	38± 10	20± 4
Enhancement (^{13}C)	100± 20	60± 10	38± 6	20 ± 5
Used Probe	McKay	DD	solenoid	McKay

Table 4.4: ^1H and ^{13}C polarisation build-up times τ, relaxation T_1 times, enhancements ϵ for samples of TEMPO in 1:1 glycerol-water. The probes used for these experiments are: McKay, double resonance probe with a solenoid as sample coil (solenoid) and the double resonance probe used in diagnostic and dissolution (DD). It was assumed that the proton and the ^{13}C spin temperatures achieved the same value at equilibrium.

Table 4.4 summarises how much polarisation enhancement could be expected for different sample compositions. In fully protonated samples the thermal contact between Zeeman reservoirs and the lattice was higher and a lower polarisation enhancement was obtained. Longer polarisation build-up and relaxation times were measured at lower temperatures. The irradiation conditions were also important, since they changed significantly from one probe to another. The enhancements obtained with the McKay probe and the double

resonance probe with a solenoid as sample coil were very similar, but higher than those usually obtained with the dissolution probe. Maximal microwave irradiation power was used in these experiments, and [12] better enhancements for deuterated glycerol-D_2O were obtained, with two to three times more polarisation enhancement compared to the fully protonated samples. Within the margin of error it was concluded that both Zeeman reservoirs acquired the same inverse temperature.

To obtain a high ^{1}H polarisation in a short time the best strategy was to substitute protons by deuterium in the sample and to increase the TEMPO concentration. With the first procedure the number of proton spins in the sample was reduced and therefore the thermal contact with the lattice was decreased, and a higher enhancement was obtained. With the second one the ^{1}H polarisation build-up was made shorter.

4.3.2 Thermal mixing via the electron dipolar reservoir.

In samples doped with TEMPO it is possible to study the interactions between nuclear thermal reservoirs of different spin species. An example of the time course for the polarisation build-up for ^{1}H, ^{13}C and ^{23}Na spins in a sample of 0.236 M [^{13}C-1] Na acetate and 87 mM TEMPO in 1:1 glycerol-water is shown in figure 4.12. In this example the build-up times for ^{1}H, ^{13}C and ^{23}Na polarisations were 4.6 $\pm$ 0.3, 18$\pm$ 3 and 13$\pm$ 1 minutes respectively and the T_1 values were 13 $\pm$ 1, 45 $\pm$ 3, and 24 $\pm$ 1 minutes respectively. The enhancements were 20 for ^{1}H, ^{13}C and ^{23}Na within the limit of error. The similar DNP enhancements at 1.72 K suggests that the different spin species reach the same spin temperature within the margin of error. Different build-up times and T_1 values could be explained by different heat capacities of the reservoirs and thermal contacts, which depend on the dipolar interactions between nuclei and the free radical.

The results in figure 4.12 therefore provided evidence of thermal mixing between three Zeeman reservoirs. Further experimental evidence of thermal

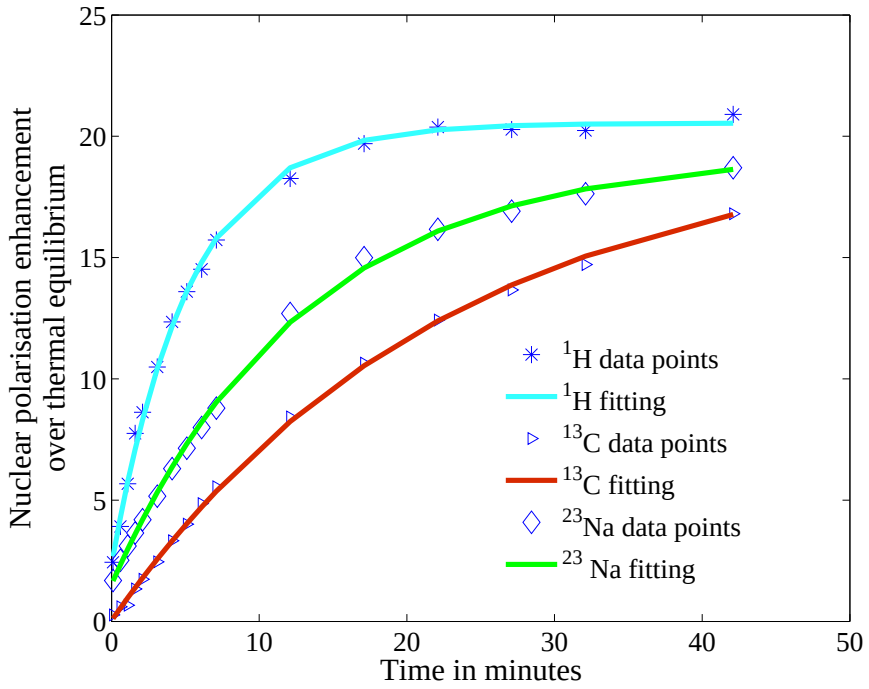

Figure 4.12: *Example of thermal mixing in a sample of TEMPO 87 mM with [^{13}C-1] labelled acetate 0.236 M in 1:1 glycerol-water at 1.72 K.*

mixing was provided by the experiment shown in figure 4.13. In this experiment the polarisation of the same sample as used for the experiment shown in figure 4.12 was probed while it increased from initially zero after saturation to the maximum value. From a certain point in time the ^{1}H magnetisation was saturated with 90^{o} pulses every 333 ms while the ^{13}C magnetisation was being acquired with small flip angle pulses. The rate of the evolution of the ^{13}C polarisation towards the new quasiequilibrium state close to saturation was 6.4 minutes.

Provided there was good thermal contact between the electron dipolar reservoir and the proton Zeeman reservoir, the ^{13}C magnetisation evolved to the new spin temperature of the electron dipolar thermal reservoir. The much

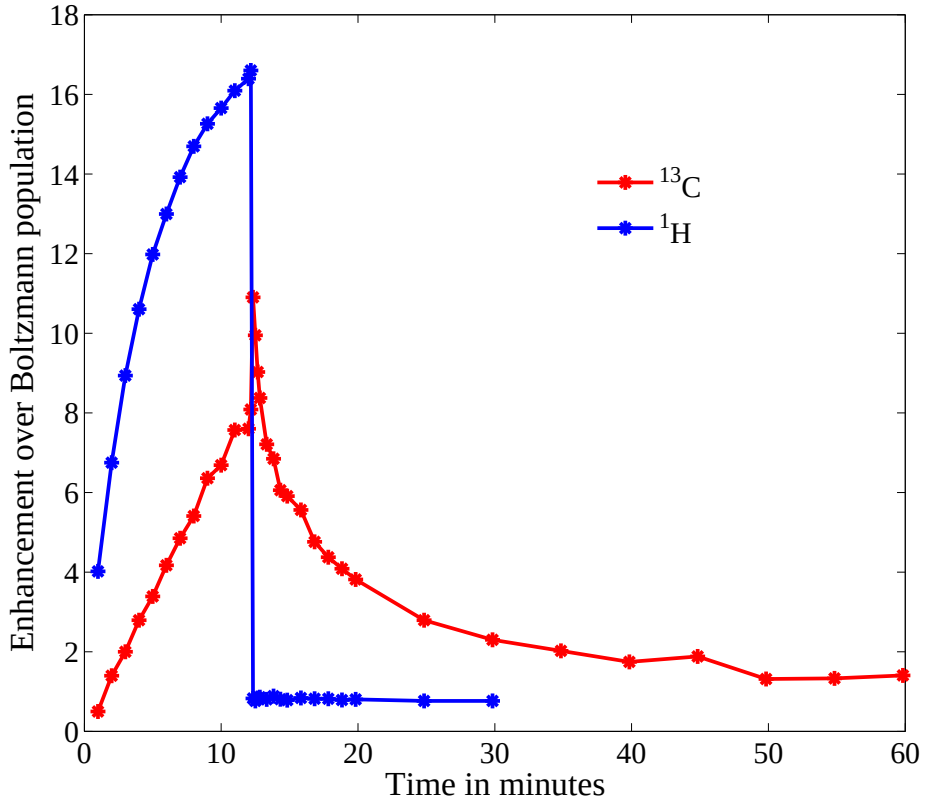

Figure 4.13: *Example of thermal mixing in a sample of 87 mM TEMPO with [^{13}C-1] labelled Na acetate 0.236 M in 1:1 glycerol-water at 1.72 K. The ^{1}H magnetisation was saturated by applying $\frac{\pi}{2}$ pulses starting at t=12 min. Some nuclear spin polarisation transfer when the proton polarisation is saturated was observed.*

larger heat capacity of the proton Zeeman bath was responsible for this since $\frac{c_{1_H}}{c_{13_C}} = \frac{n_{1_H}\omega_{1_H}^2}{n_{13_C}\omega_{13_C}^2} \simeq 6000$, with c_{13_C} and c_{1_H} the heat capacities for the ^{13}C the ^{1}H Zeeman reservoirs.

The experiment shown in figure 4.8, in which the build-up of ^{13}C polarisation was observed in a sample containing trityl while saturating the ^{1}H polarisation was repeated with TEMPO as radical.

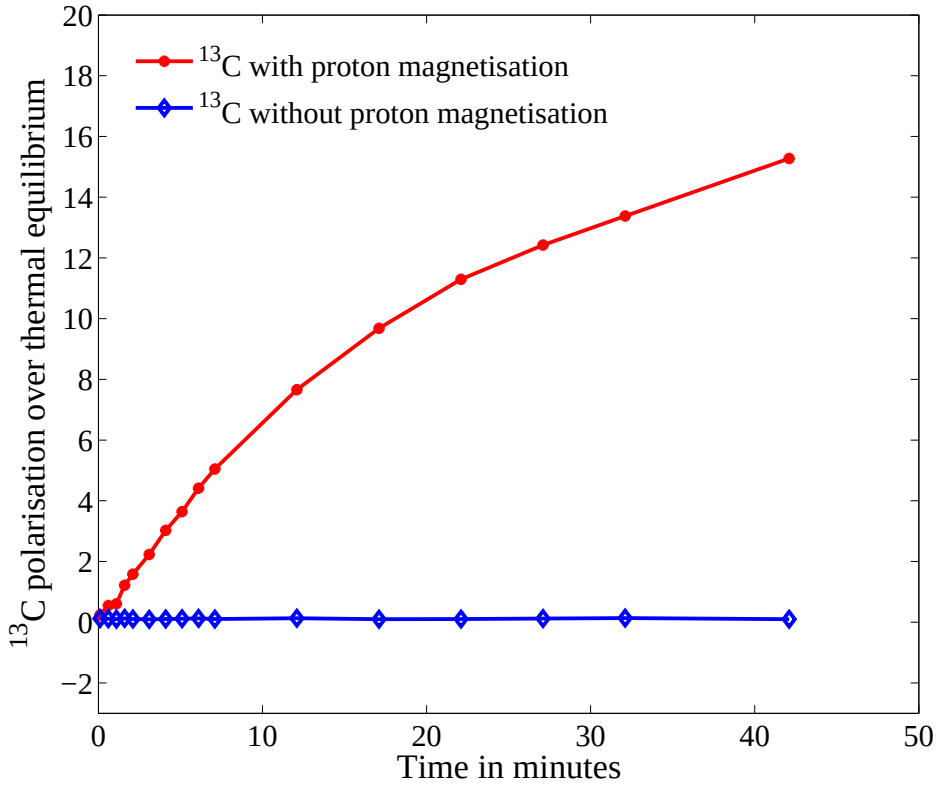

Figure 4.14: *Example of thermal mixing in a sample of 87 mM TEMPO with 0.236 M [^{13}C-1] Na acetate in 1:1 glycerol-water at 1.72 K. The DNP irradiation was left to 93.95 GHz all the experiment.*

The results are shown in figure 4.14. The difference is striking. In the case where both ^{1}H and ^{13}C polarisations were left to evolve freely under DNP irradiation, the two build-ups were similar as shown in figure 4.12. When the ^{1}H polarisation was saturated periodically (a 10 μs 90 degree pulse applied every 333 ms, the T_2 for ^{1}H magnetisation was less than 30 microseconds) the ^{1}H NMR signal was in the noise baseline and the ^{13}C polarisation did not increase noticeably. This experiment could be considered as a way of pumping heat from the proton Zeeman reservoir to the ^{13}C Zeeman reservoir

via the electron dipolar bath, which is in contact with the electron Zeeman reservoir in the rotating frame. Taking into account the interactions with the electron dipolar reservoir which was affected by the nuclear Zeeman baths, it is possible to describe the system. The thermal mixing mechanism in this case was dynamic cooling [4].

4.4 Discussion and conclusions

Depending on the nuclear spin species and on the free radical used, the Solid Effect (SE) or Thermal Mixing TM could take place as the main DNP mechanism (or a mixture of them). It was demonstrated that for an electron resonance line with a linewidth narrower than the ^{1}H Larmor frequency (142.6 MHz)[3], [10] the main DNP pathway was the SE in a sample of 7 M ^{15}N urea doped with 15 mM Ox63 trityl in 1:1 glycerol-water. The small enhancement of the ^{1}H polarisation was attributed to a relatively short proton spin lattice relaxation time T_1 (or in other words, an excess of leakage).

The peak to peak distance in the ^{1}H DNP enhancement spectrum was predicted to be twice the ^{1}H Larmor frequency ω_n, resulting in an anti-symmetric lineshape of the enhancement curve, with a linewidth of 45 $\pm$ 10 MHz for the enhanced peaks.

The peak to peak distance in the DNP enhancement spectrum for the ^{15}N polarisation was measured in 32 MHz in the sample with DMSO (which in this case correlated with twice the ^{15}N Larmor frequency($\approx$ 30 MHz)). In the case for 7 M ^{15}N urea the distance peak to peak in the DNP enhancement spectrum was about 50 MHz, which correlated with the linewidth of the proton DNP enhancement spectrum for the same sample (7 M ^{15}N labelled urea in 1:1 glycerol-water). This suggested that the electron resonance linewidth was shorter in the case of DMSO.

The SE model could be well fitted to the data of the sample of 7 M ^{15}N labelled urea in 1:1 glycerol-water. The enhancement and temperature

were close to the limit of validity of the spin temperature approximation ($\tanh(0.5)=0.46\sim0.5$). For qualitative purposes this effect was discussed since the poor enhancement obtained made it possible to use the spin temperature approximation. Trityl does not provide a high enhancement of the ^{1}H polarisation. Higher polarisation enhancements were obtained in ^{15}N spins in ^{15}N labelled urea samples and in ^{13}C spins in samples of ^{13}C labelled formate and [^{13}C-1] acetate. In this case Goldman's model of the unresolved solid effect [8] was used to describe the DNP mechanism in qualitative terms. The simulation was able to reproduce the DNP enhancement over thermal equilibrium, the antisymmetric behaviour of the enhancement curve and the distance between the two peaks showing maximal enhancement. In the case of [^{13}C-1] labelled acetate the distance between these peaks was around 70 MHz (which corresponded to twice the ^{13}C Larmor frequency) and the electron linewidth measured with LODESR was around 30 MHz [10], which suggested a combination of solid effect and thermal mixing. The enhancements obtained with trityl radicals were, in general terms high, but lower than in the literature [2], [3]. This could be due to differences in microwave irradiation, since in this project the sample was shielded by the radiofrequency coil that acted partially as a microwave shield.

Despite the agreement with the data, it should be noted that this model derived by Goldman is based on the Provotorov equations which are not necessarily valid at low temperatures for polarisation enhancements of typically 2 orders of magnitude. On the other hand there were too many free parameters to be fitted, which were known only in order of magnitude. In any case, at least qualitatively, it was demonstrated how the unresolved solid effect model by Goldman could describe the DNP mechanism in these spin systems.

For the case of TEMPO doped samples only a few results were shown to illustrate the main DNP mechanism. The DNP enhancement spectra for ^{1}H and ^{13}C spins presented a similar shape. This provided evidence that thermal mixing was the dominant mechanism. This is a consequence of a large linewidth

of the electron resonance line due to g-anisotropy and hyperfine interaction. Within the margin of error it was shown that the nuclear Zeeman reservoirs reached the same spin temperature. The different nuclear Zeeman reservoirs had different build-up and T_1 times possibly due to different heat capacities, since for the concentrations of free radical used it was supposed that the role of spin diffusion was not as important as the direct contact (there was only 2-6 ^{1}H nuclei on average between two free radicals for an approximate concentration of 110 M and 0.1 M for ^{1}H and free radicals, respectively). A demonstration of thermal mixing was shown in figure 4.13 where the evolution of Zeeman magnetisations reflected the behaviour of the two thermal baths in contact. The saturation of the ^{1}H polarisation heated up the electron dipolar bath which in turn heated up the ^{13}C Zeeman reservoir. The possibility of reaching the electron dipolar reservoir through the proton Zeeman bath strongly suggested dynamic cooling as the main DNP mechanism. It was possible to obtain high and rapid enhancements of nuclear magnetisation by using a deuterated glassy matrix and adding large amount of free radicals. By increasing the TEMPO concentration the time required to obtain maximal enhancements was in general shorter with TEMPO than with trityl radicals.

Bibliography

[1] A. Abragam and M. Goldman. Principles of dynamic nuclear polarisation. *Rep. Prog. Phys.*, 41, 1978.

[2] J. H. Ardenkjaer-Larsen, B. Fridlund, A. Gram, G. Hansson, L. Hansson, M. H. Lerche, R. Servin, M. Thaning, and K. Golman. Increase in signal-to-noise ratio of $>$ 10000 times in liquid-state NMR. *Proc. Nat. Acad. Scienc.*, 100:18, 2003.

[3] J. H. Ardenkjaer-Larsen, S. Macholl, and H. Johannesson. Dynamic nuclear polarisation with trityls at 1.2 K. *Appl. Magn. Reson.*, 34:509–522, 2008.

[4] V. A. Atsarkin. Dynamic polarization of nuclei in solid dielectrics. *Usp. Fiz. Nauk*, 126:3–39, 1978.

[5] B. Cowan. *Nuclear Magnetic Resonance and Relaxation.* Cambridge University Press, 1997.

[6] E. F. Garman and T. R. Schneider. Macromolecular cryocrystrallography. *J. Appl. Cryst*, 30:211–237, 1997.

[7] S. T. Goertz. The dynamic nuclear polarization process. *Nuc. Instr. Meth. Phys. Res.*, 526:28–42, 2004.

[8] M. Goldman. *Spin Temperature and nuclear magnetic resonance in solids.* Oxford at the Clarendon Press (London), 1970.

[9] M. Goldman. Overview of spin temperature, thermal mixing and dynamic nuclear polarisation. *Appl. Magn. Reson.*, 34:219–226, 2008.

[10] Josef Granwehr. Private communications.

[11] J. Kemsley. Dynamic nuclear polarization opens up new ways to illuminate biochemical processes. *C.& E. N.*, 86:12–15, 2008.

[12] F. Kurdzsau, B. van den Brant, A. Comment, P. Hautle, S. Jannin, J. J. van der Klink, and J. A. Konter. Dynamic nuclear polarization of small labelled molecules in frozen water-alcohol solutions. *J. Phys. D: Appl Phys*, 41:155506, 2008.

[13] D. M. Spielman, D. Mayer, Y-F. Yen, J. Tropp, R. E. Hurd, and A. Pfefferbaum. In vivo Measurement of Ethanol Metabolism in the Rat Liver Using Magnetic Resonance Spectroscopy of Hyperpolarized [1-^{13}C] Pyruvate. *Mag. Res. Med*, 62:307–313, 2009.

Chapter 5

Nuclear polarisation transfer

Polarisation transfer sequences may be used in solid state NMR to transfer spin order from the ^{1}H to the ^{13}C thermal reservoirs. Provided DNP is used, the efficiency of the process may be increased either in the final ^{13}C magnetisation or in the time required to achieve it [9]. The aim of this chapter is to illustrate how some sequences for polarisation transfer perform at temperatures around 1.5 K and how some of these can be used for dissolution experiments.

5.1 Cross Polarisation theory

Cross Polarisation (CP) is an NMR technique used to transfer polarisation between two spin species [4]. The case applied in this thesis is the polarisation transfer between ^{1}H and ^{13}C spins which could lead to an enhancement up to $\frac{\gamma_{^1H}}{\gamma_{^{13}C}}$ of the ^{13}C polarisation. The basics of the experiment are briefly detailed below.

CP in a static solid sample

The spin systems studied were kept at temperatures around 1.5 K in static conditions. In a typical CP experiment between protons and ^{13}C the ^{1}H spins are polarised, either by waiting until Boltzmann equilibrium is reached or to a

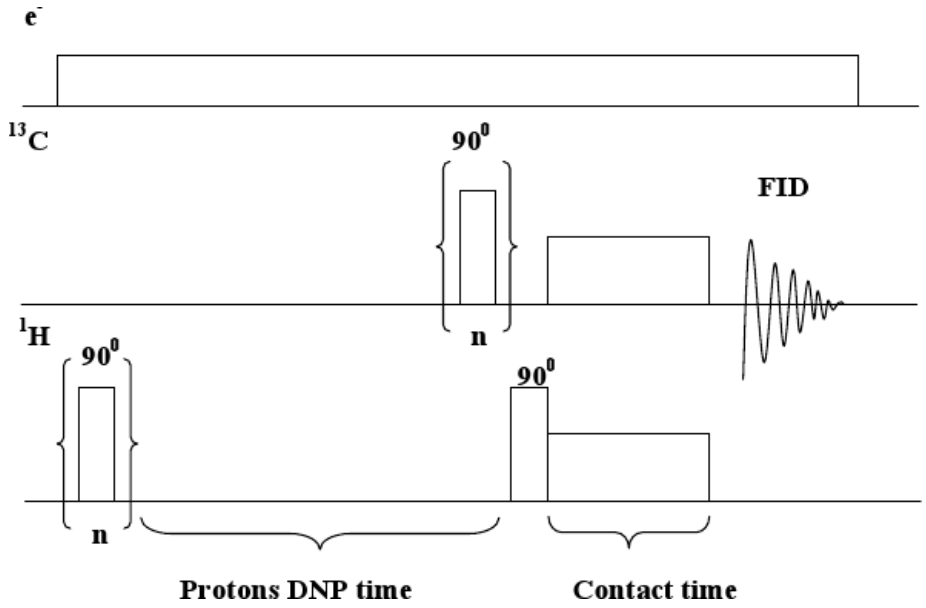

Figure 5.1: *Cross polarisation sequence. For repeatability of the experiment the proton magnetisation is first saturated, and a selected time left for the proton magnetisation to build up, via either DNP or just spin lattice relaxation. Before the CP sequence is applied, the* ^{13}C *magnetisation is saturated with a train of pulses prior to the* ^{1}H $\frac{\pi}{2}$ *pulse leaving a known initial state for both magnetisations.*

much higher polarisation using DNP. The ^{1}H magnetisation is rotated by 90^o, and spin locked during a contact time τ along with the ^{13}C spins, or, in other words, irradiated with a 90^o pulse shifted in phase from the previous pulse. For an effective polarisation transfer, both spin systems must be irradiated with the same effective field strength fulfilling the Hartman-Hahn condition [4]. The basic sequence is illustrated in figure 5.1.

For a system comprising one proton spin I and one carbon spin S in the laboratory frame, the Hamiltonian of the two spins coupled by dipolar interactions under two respective RF B_1 magnetic fields [5]:

$$\begin{aligned}\hat{H} = &- \hbar\gamma_I B_0 \hat{I}_z - \hbar\gamma_S B_0 \hat{S}_z \\ &- 2\hbar\gamma_I B_{1I} \hat{I}_y cos(\omega_I t) - 2\hbar\gamma_S B_{1S} \hat{S}_y cos(\omega_S t) \\ &+ \frac{\hbar^2 \mu_0 \gamma_I \gamma_S}{4\pi r^3}(1 - 3cos^2\vartheta)\hat{I}_z \hat{S}_z \end{aligned} \tag{5.1}$$

where B_{1I} and B_{1S} represent the strengths of the RF magnetic fields and ω_I and ω_S represent the carrier frequencies. The dipolar term in equation 5.1 is the truncated secular part since this is the unique term that is not averaged out. Following figure 5.1, the proton and ^{13}C magnetisations are tilted and spin-locked. The transformations for the Hamiltonian and the density matrix are [5]:

$$\begin{aligned}\hat{H}_{TR} &= \hat{T}\hat{R}\hat{H}\hat{R}^{-1}\hat{T}^{-1} + i[\dot{\hat{T}}R][\hat{T}\hat{R}]^{-1} + i\dot{\hat{T}}\hat{T}^{-1} \\ \hat{\rho}_{TR} &= \hat{T}\hat{R}\hat{\rho}\hat{R}^{-1}\hat{T}^{-1} \end{aligned} \tag{5.2}$$

where

$$\begin{aligned}\hat{R} &= e^{-(i\omega_I \hat{I}_z t + i\omega_S \hat{S}_z t)} \\ \hat{T} &= e^{i(\Phi_I \hat{I}_y + \Phi_S \hat{S}_y)} \end{aligned} \tag{5.3}$$

and

$$\Phi_I = arctan(\frac{\omega_{1,I}}{\omega_{0I} - \omega_I}) \qquad \Phi_S = arctan(\frac{\omega_{1,S}}{\omega_{0S} - \omega_S}) \tag{5.4}$$

In equation 5.4, $\omega_{0I} - \omega_I$ and $\omega_{0S} - \omega_S$ define how far off resonance the carrier frequency of protons (ω_{0I}) and ^{13}C (ω_{0S}) are, respectively. Neglecting non-secular terms and naming $d = \frac{\mu_0 \gamma_I \gamma_S \hbar}{8\pi^2 r^3}(1 - 3\cos^2(\vartheta))$ the Hamiltonian becomes is:

$$\begin{aligned}\hat{H}_{TR} = &-\hbar\omega_{eI}\hat{I}_z - \hbar\omega_{eS}\hat{S}_z + hdcos(\Phi_I)\cos(\Phi_S)\hat{I}_z\hat{S}_z + \\ &+\frac{hd}{4}\sin(\Phi_I)\sin(\Phi_S)(\hat{I}^+\hat{S}^- + \hat{I}^-\hat{S}^+) \end{aligned} \tag{5.5}$$

Once the Hamiltonian is in the tilted rotating frame it can be expressed within the zero- and the double-quantum Liouville subspace. In this manner,

it is possible to diagonalise the resulting Hamiltonian by tilting it by an angle:

$$\varphi = arctan(\frac{d\pi sin(\Phi_I)sin(\Phi_S)}{\omega_{eff,I} - \omega_{eff,S}}) \tag{5.6}$$

where $\omega_{eff,I} = \sqrt{\omega_{1,I}^2 + \Delta\omega_I^2}$ and $\omega_{eff,S} = \sqrt{\omega_{1,S}^2 + \Delta\omega_S^2}$. The Hartmann-Hahn condition is fulfilled when $\omega_{eff,I} = \omega_{eff,S}$. With such a diagonal Hamiltonian it is possible to solve the Liouville von Neumann equation to find the time evolution of the density matrix. The density matrix is tilted and transformed to the double rotating frame with the previous transformation in equation 5.2. Using the Hamiltonian in equation 5.5 the density operator is propagated. The density matrix must be back transformed before calculating the magnetisation at the end of the sequence [5], [11].

The magnetisation

The density matrix is used in the calculation of observables such as the ^{13}C magnetisation. If the resonance condition is fulfilled, the expressions for the transverse magnetisations are sinusoidal functions that reflect the oscillating behaviour of the magnetisation between the two spins I and S.

Coherence and incoherence: spin temperature in the doubly rotating frame

In a system where a ^{13}C atom is surrounded by many hydrogen atoms, the polarisation transfer process is not coherent. In theoretical approaches the dipolar interaction between proton spins must be taken into account. A system composed of many Zeeman packets has been suggested [10]. The system can also be considered with a spin temperature model for two different spins in the doubly rotating frame. The spin temperature concept can be obtained in analogy with the spin temperature in the laboratory frame. The density matrix is considered with the linear approximation. The temperature that divides the Hamiltonian used for this density matrix becomes the spin temperature in the

rotating frame. This model considers two Zeeman reservoirs $\hat{H}_I$ and $\hat{H}_S$ with dipolar reservoirs $\hat{H}_{II}$, $\hat{H}_{IS}$, $\hat{H}_{SS}$ [4]. They all have different heat capacities and are in contact with each other with different contact rates. The condition for maximum thermal contact with the secular $\hat{H}_{IS}$ thermal reservoir would be the Hartmann-Hahn condition in which the energy levels for the protons and the ^{13}C nuclei are equated.

5.2 Experimental: spectral bandwidth and B_1 requirements

To achieve a full 90^o rotation on the proton magnetisation at the beginning of the CP sequence, the excitation bandwidth must be larger than the dipolar bandwidth present in the spectrum. If power delivery to the coil is limited, then only a part of the spectrum will be effectively excited, with a concomitant reduction of the efficiency in the polarisation transfer process. There are several causes of line broadening in the ^{1}H spectra. The main one is proton dipolar broadening. This contribution becomes apparent when the proton spectrum bandwidths from a fully protonated solvent and a fully deuterated solvent are compared. Another dipolar broadening source is due to the presence of paramagnetic impurities. The shimming of the system also needs to be taken into account since a polariser is not designed as rigourously as a spectrometer and the B_0 inhomogeneities can be around 100 ppm within the sample space. This would amount to less than 1 kHz approximately in the sample. A typical proton line in solid state NMR of a sample of 1:1 water-glycerol presents a bandwidth of about 90 kHz. A typical linewidth of ^{13}C in a sample of ^{13}C labelled Na acetate in 1:1 water-glycerol is 8 kHz.

In order to achieve sufficiently large B_1 field in ^{1}H experiments, problems with power limitation at the sample coil may result as a consequence of the required bandwidth.

Excitation of the full proton resonance line would require a radiofrequency

pulse with a duration of 2.77 μs. However, in the experimental set-up such short pulses could not be achieved with the power available. A further limitation was also set by the presence of arcing during high power pulses with a duration on the order of milliseconds.

An effective way to considerably diminish this linewidth is by dissolving the sample in a deuterated solvent, instead of a fully protonated sample (typically in a sample of 100 mM TEMPO with 2 M [^{13}C-1] Na acetate in 1:1 deuterated glycerol-D_2O the linewidth is close to 20 kHz), as shown in figures 5.2 and 5.3.

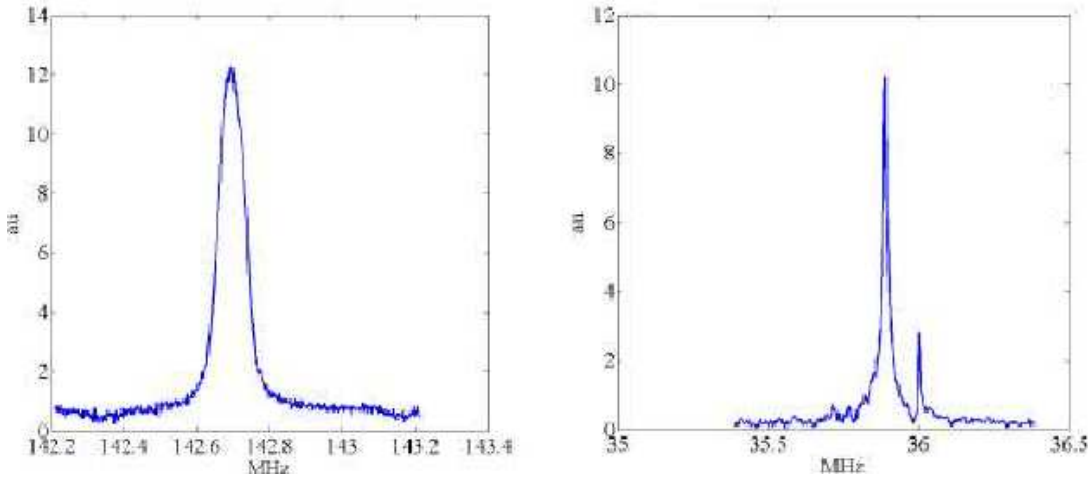

Figure 5.2: *Two solid state NMR spectra for a sample of 93 mM TEMPO with 2.4 M [^{13}C-1] Na acetate in 1:1 glycerol-water. The figure on the left corresponds to ^{1}H (90 kHz bandwidth) and that on the right is for ^{13}C (9 kHz bandwidth), both at a temperature of 1.66 K.*

This may reduce the ^{1}H bandwidth to about 20 kHz, which makes the necessary B_1 field less power demanding for CP experiments.

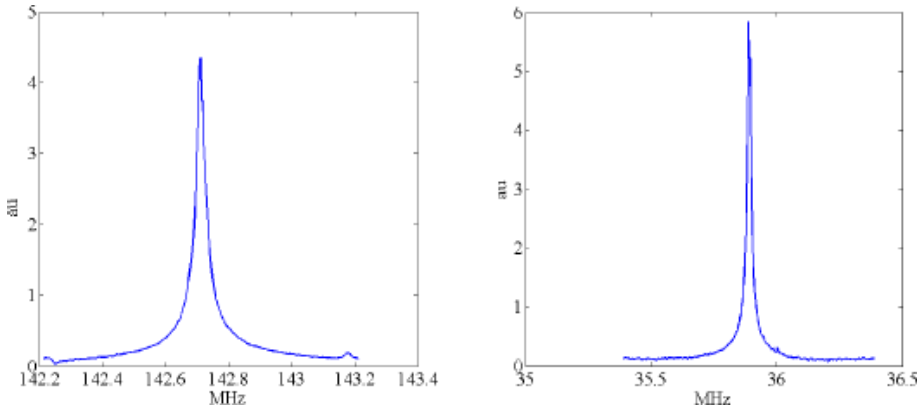

Figure 5.3: *Two spectra in solid state NMR for a sample of TEMPO 91 mM with 1.54 M [^{13}C-1] Na acetate in 1:1 deuterated glycerol-D_2O. The figure on the left corresponds to ^{1}H (16 kHz bandwidth) and that on the right is for ^{13}C (7 kHz bandwidth)both at a temperature of 1.71 K*

5.3 Cross Polarisation and Dynamic Nuclear Polarisation

In this work DNP has been applied to samples doped with TEMPO to enhance the ^{1}H magnetisation before a CP sequence transferred the polarisation to the ^{13}C nuclei [9]. The samples were irradiated at the frequency of maximum polarisation enhancement which was 93.95 GHz, using a 200 mW microwave source.

They were prepared with concentrations of TEMPO free radical close to 100 mM , in order to obtain the shortest enhancement time possible.

Typical build-up times for ^{1}H in these conditions and for this kind of matrix at 1.5 K range from 2 to 10 minutes, whereas for ^{13}C they range from 15 to 60 minutes (chapter 4, tables 4.3 and 4.4).

Pulse sequences for calibration experiments

To optimise the CP sequence, the Hartmann-Hahn (H-H) condition was established first by setting the ^{1}H B_1 field to 40 kHz and varying the ^{13}C B_1

strength with a contact time of a 500 μs. An example in figure 5.4 shows that this condition presents a relatively wide tolerance at 1.5 K. Once the ^{13}C B_1 frequency was selected for the H-H condition, the contact time was optimised by changing its duration in small steps. Figure 5.5 shows dependence of the CP build-up on the contact time.

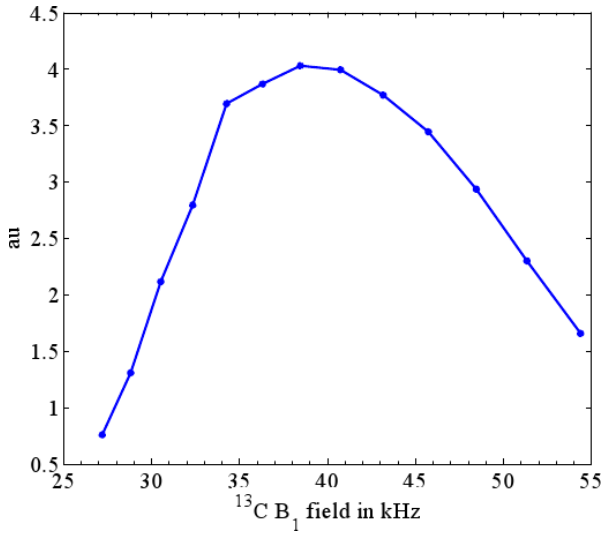

Figure 5.4: *The polarisation transfer dependence on the ^{13}C B_1 field strength shows the Hartmann-Hahn condition in a sample of 86 mM TEMPO with 2M [^{13}C-1] Na acetate in 1:1 glycerol-water after 90 s of DNP irradiation. The ^{1}H B_1 field was set to 40 kHz, in a sample of 90 mM TEMPO with 2 M [^{13}C-1] acetate in 1:1 glycerol-water at 1.57 K.*

In figure 5.6, a comparison between different strategies to generate ^{13}C polarisation in a sample with [^{13}C-1] labelled Na acetate shows the effectiveness of this method at temperatures of around 1.5 K for achieving a high polarisation of the ^{13}C spin system. The efficacy of this process was measured to be at least 39%. The magnetisation in the $x-y$ plane could be increased to almost twice the value that would be obtained by just applying DNP in a time of the order of the ^{1}H DNP build-up instead of the much longer ^{13}C DNP build-up [9].

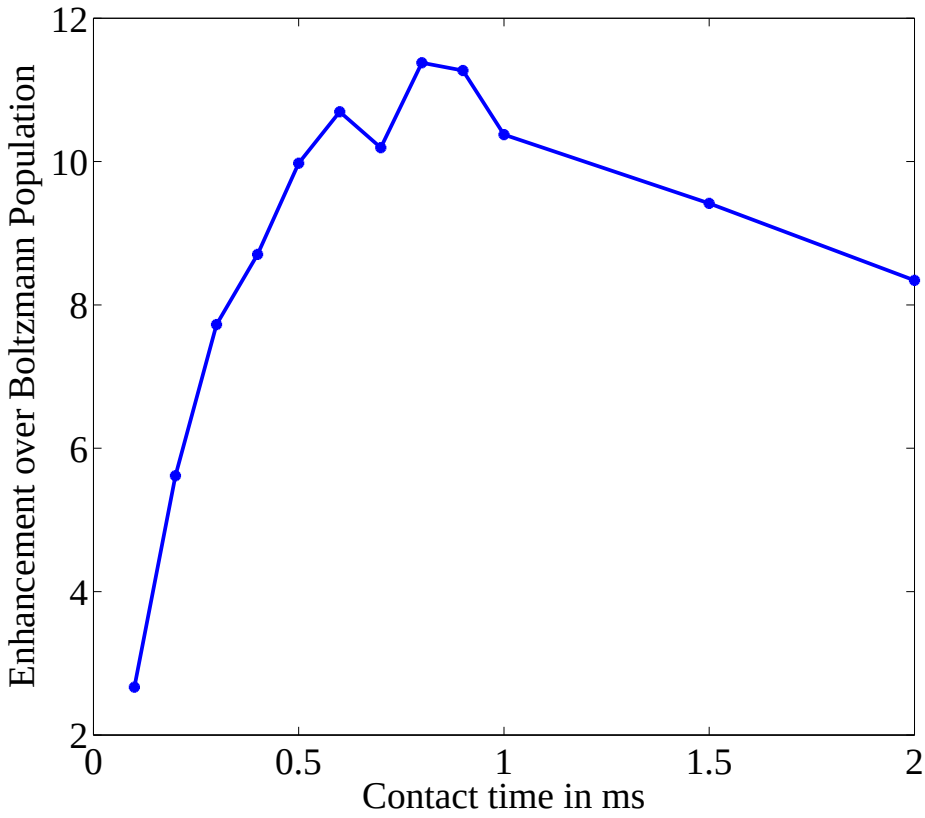

Figure 5.5: *Contact time in a CP experiment. Evolution of the ^{13}C magnetisation with the CP contact time in a sample of 1.58 M [^{13}C-1] Na acetate with 84 mM TEMPO in 1:1 glycerol-water after 60 s of DNP irradiation. In this case the B_1 of both channels was set to 41 kHz.*

5.4 Low power polarisation transfer sequences using TEMPO and DNP

The presence of an electronic dipolar bath that communicates with the Zeeman and dipolar thermal reservoirs may be used to cool the ^{13}C Zeeman reservoir with alternative sequences that do not require high power. A spin locked sequence presented by Dementyev [2] uses the presence of the dipolar reservoir to enhance the proton signal 50% above the already enhanced magnetisation using the Strombotne-Hahn oscillations. This oscillating thermal mixing [12] is

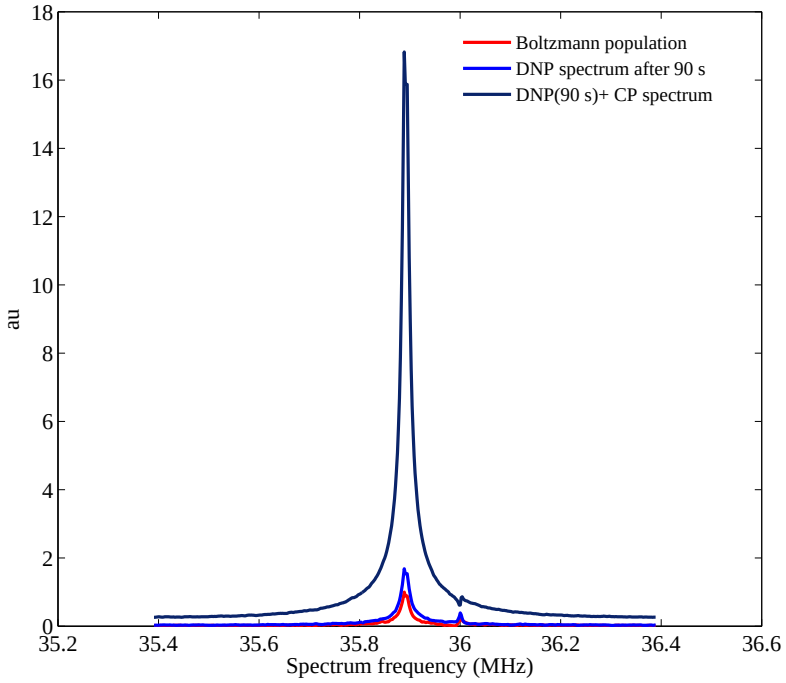

Figure 5.6: *Comparison between the ^{13}C polarisation reached after 90 s of DNP, and applying CP afterwards. The Boltzmann population is also presented. The sample was the same as in figure 5.5. The B_1 fields were optimised to 50 kHz. This was obtained using the double resonance probe with a solenoidal sample coil.*

transferred to the ^{13}C polarisation if another thermal contact pulse is applied. Some of these sequences for non-Zeeman CP, presented by Yannoni and Vieth et al [12], that store the magnetisation in a thermal dipolar reservoir were tested in liquid helium environments.

5.4.1 Non-Zeeman Cross Polarisation (NZCP)

Some sequences for polarisation transfer other than CP, that do not require the Hartmann-Hahn condition to be met, have been suggested [12]. In one of the non-Zeeman CP sequences [12], a hard pulse is applied off-resonance on the wing of the ^{1}H spectrum. This pulse lasts for a few μs with B_1 strength comparable to the spectral linewidth. Immediately after this pulse another hard pulse is applied on the ^{13}C channel. This second pulse is chosen to be a few milliseconds with much lower power, as shown in figure 5.7. This sequence demonstrates that irradiation on the wing of the proton spectrum mixes Zeeman order with dipolar order. The polarisation is transferred to ^{13}C with a long low power pulse on this latest channel. Changing the duration of the pulse on the proton channel reflects the oscillatory behaviour of the transferred polarisation. The oscillation frequency shown in the ^{13}C polarisation decreases on reduction of the ^{1}H B_1 field, which reflects the dependence of this mixing on the Rabi frequency. This sequence showed wide tolerance to variations of the ^{13}C pulse length (less than 10% variation achieved in ^{13}C magnetisation on changing the ^{13}C contact pulse by more than 5 ms) and B_1 (less than 20% change in achieved ^{13}C magnetisation over a range of $\pm$7 kHz).

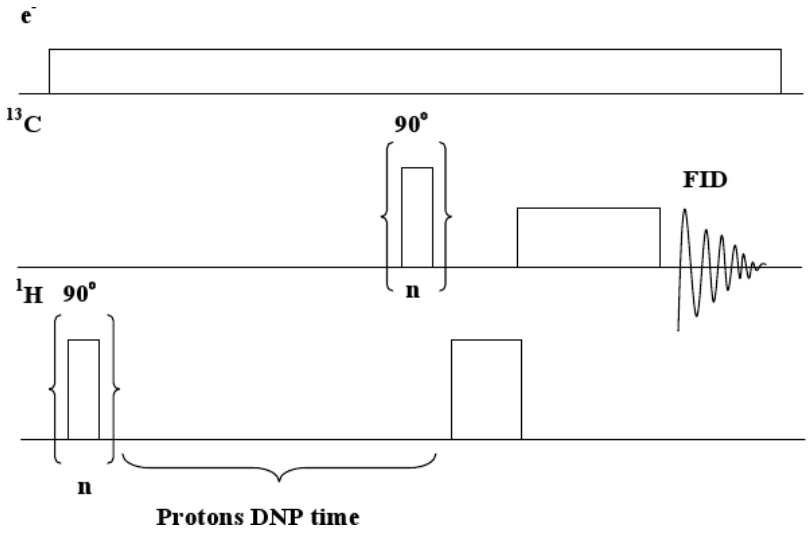

Figure 5.7: *First NZCP sequence presented by Yannoni and Vieth et al [12]. The magnetisation is saturated before thermal mixing in the rotating frame takes place. As with the CP sequence, the proton magnetisation is built up. The tilt angle on the proton channel establishes contact between the Zeeman and dipolar thermal reservoirs. The* ^{1}H B_1 *nutation frequency is reflected on the* ^{13}C *transferred magnetisation.*

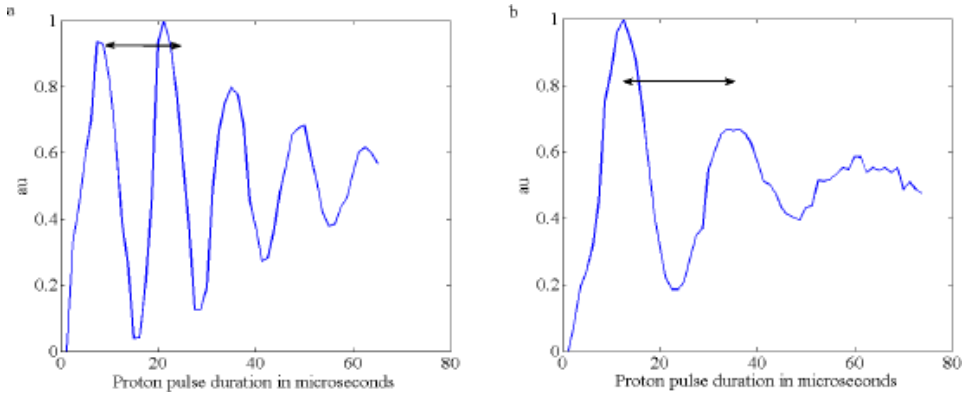

Figure 5.8: ^{13}C *results from the first NZCP sequence presented by Yannoni and Vieth et al [12]. The sample chosen was 86 mM TEMPO with 2 M [*^{13}C*-1] Na acetate in 1:1 glycerol-water. The* B_1 *field in this case was 20 kHz for* ^{13}C *and the pulse length was 9 ms.* B_1 *for* ^{1}H *was approximately 55 and 40 kHz in figures (a) and (b) respectively, at 1.62 K.*

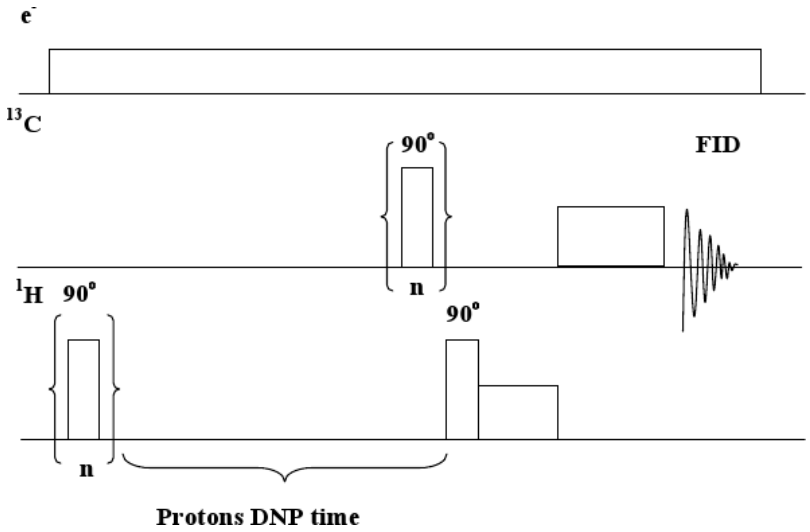

Figure 5.9: *Second sequence for non-Zeeman polarisation transfer presented by Yannoni and Vieth et al [12]. In this case, the proton polarisation is tilted 90º and spin-locked. During this time, the proton spin Zeeman reservoir cools the dipolar reservoir. The ^{13}C Zeeman reservoir is then cooled by the latter, with a long, low power pulse.*

5.4.2 Non-Zeeman Cross Polarisation with spin locking on proton spins

This sequence (shown in figure 5.9), published by Yannoni and Vieth et al [12], uses spin locking to establish thermal contact between the ^{1}H Zeeman and the dipolar thermal baths instead of a single pulse. Afterwards, the ^{13}C is cooled by a long, low power pulse. In this sequence the pulses were applied on-resonance.

This technique required a strong $\frac{\pi}{2}$ pulse and then a spin lock of low power to achieve thermal mixing between the dipolar reservoir and the proton Zeeman reservoir in the single rotating frame. The B_1 strength for the ^{13}C channel during the mixing pulse was also low (of the order of 10 kHz). As shown in figure 5.10, this sequence showed tolerance in the selection of the B_1 fields and on the duration of the ^{13}C pulse.

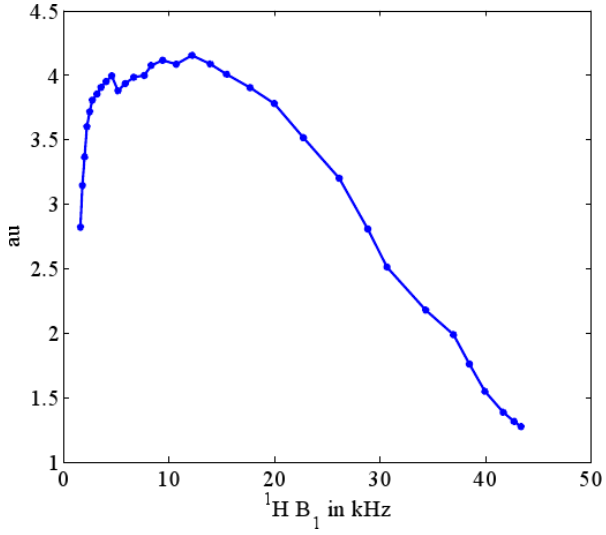

Figure 5.10: *Spin-locked NZCP result of varying the 2 ms* ^{1}H B_1 *field for a selected* ^{13}C *pulse of 9 ms at 19 kHz for the same sample as in figure 5.8.*

Comparison between sequences

These three techniques tested at temperatures close to 1.5 K, have achieved successful polarisation transfer. Of these techniques, the CP and NZCP with spin lock were the most efficient (CP being no less than 39% efficient). In figure 5.4.2 the results of these two are compared with the DNP ^{13}C spectrum obtained after 90 s of DNP irradiation in a sample of TEMPO and [^{13}C-1] Na acetate in 1:1 glycerol-water. It is shown that using NZCP with spin lock on the proton channel yields only 60% that which can be achieved with CP, which translated to a minimum efficiency of 23%. However, with NZCP the matching conditions are not as strict as with CP, and the power restrictions are less severe. This translates to a lower probability of arcing and corona discharge problems when working at very low temperature.

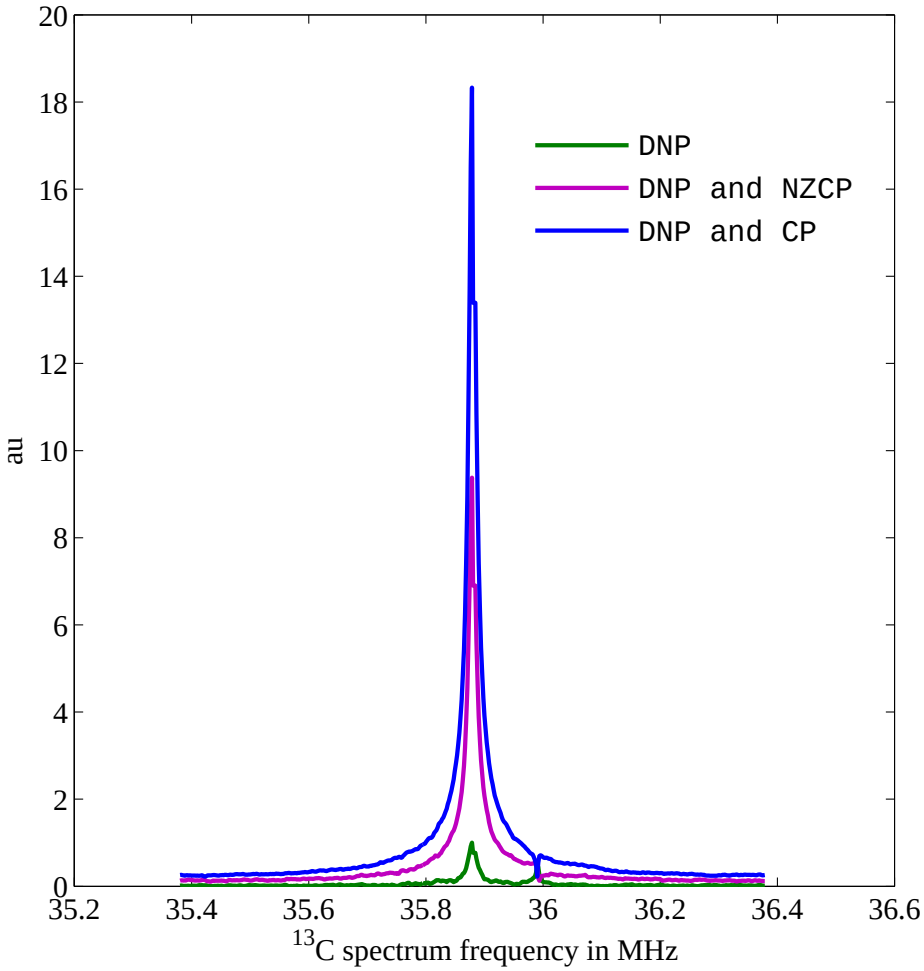

Figure 5.11: *Spectra of ^{13}C obtained after 90 s of irradiation and applying a 90º pulse, a CP sequence and a spin-locked NZCP. The sample was the same as used for figure 5.8. Both CP and NZCP were optimised before the spectra shown in this figure were taken. For NZCP the ^{1}H pulse was 2 ms (14 kHz) and the ^{13}C was 9 ms (19 kHz).*

5.5 Pulse sequences $\hat{I}_z \Longrightarrow \hat{S}_z$

For dissolution experiments the final ^{13}C magnetisation must remain aligned with the magnetic field for a sufficient time during dissolution of the sample (about 2 minutes). With the previous CP techniques the final ^{13}C magnetisation was obtained in the $x-y$ plane. When the ^{13}C magnetisation was rotated using a $\frac{\pi}{2}$ pulse only part of it achieved this final state because of radio frequency inhomogeneities, and then diminished quickly in a similar manner to the thermal mixing experiment in figure 4.12 (chapter 4). The target of a dissolution experiment after a nuclear-nuclear polarisation transfer pointed to a sequence of $\hat{I}_z \Longrightarrow \hat{S}_z$ as the best choice instead of $\hat{I}_z \Longrightarrow \hat{S}_{xy} \Longrightarrow \hat{S}_z$.

Adiabatic pulse sequences offer another alternative to hard pulse CP sequences, since they require less power to achieve polarisation transfer [8].

Hard pulse $\hat{I}_z \Longrightarrow \hat{S}_z$ CP sequences

A 0^o pulse sequence named composite zero cross polarisation (COMPOZER-CP) that achieves $\hat{I}_z \Rightarrow \hat{S}_z$ polarisation transfer has been proposed by Fukuchi *et al.* [3]. It is based on changes in phase every time a 360^o is applied to both channels simultaneously.

A Hamiltonian involving two Zeeman spin terms ($\hat{H}_I + \hat{H}_S$), two radiofrequency terms ($\hat{H}_{RFI} + \hat{H}_{RFS}$) and the only heteronuclear dipolar term that remains in the rotating frame ($d\hat{I}_Z\hat{S}_Z$) is $\hat{H} = \hat{H}_I + \hat{H}_S + \hat{H}_{RFI} + \hat{H}_{RFS} + \hat{H}_{DIS}$ (I denotes ^{1}H spin and S, ^{13}C). This Hamiltonian is propagated with an operator $\hat{U}$ defined with the aid of the Dyson time ordering operator $\hat{T}$ ($\hat{U} = \hat{T}e^{-i\int_0^t dt'\hat{H}}$). The evolution of the spin system can be separated according to the RF and the dipolar interactions [3]. After selecting the zeroth order average Hamiltonian, $\hat{H}_d^0$, using the Magnus expansion the heteronuclear dipolar Hamiltonian term is $\hat{H}_d^0 = \frac{d}{2}(\hat{I}_Z\hat{S}_Z + \hat{I}_Y\hat{S}_Y)$ for a time τ, where τ satisfies $(\omega_I + \omega_S)\tau = 2n\pi$ (n=0,1,2,...). If instead of a single 360^o angle, two pulses are chosen with different phase, x and y, the dipolar term obtained presents the form of a dipolar

flip-flop expression $2\hat{I}_z\hat{S}_z + \hat{I}_x\hat{S}_x + \hat{I}_y\hat{S}_y$ which commutes with $\hat{I}_z + \hat{S}_z$ but not with $\hat{I}_z - \hat{S}_z$. In this way the polarisation transfer $\hat{I}_z \Rightarrow \hat{S}_z$ is demonstrated quantum-mechanically.

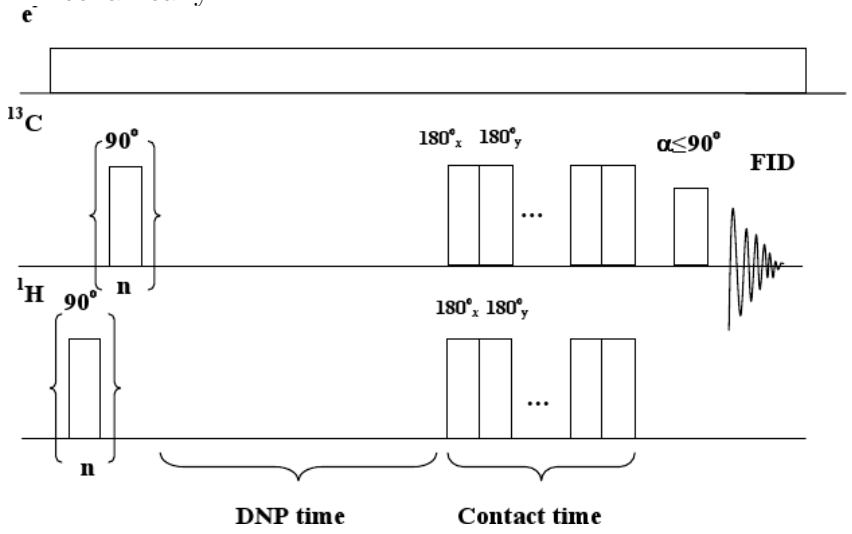

Figure 5.12: *Tested sequence based on the COMPOZER-CP from Fukuchi. The proton polarisation is first built up as in the other sequences, and then a train of 180º pulses is applied. Each pulse alternates the frequency phase x-y-x-y.*

The COMPOZER-CP sequence was tested in our system at 1.5 K. Although it worked, the achieved efficiency was hampered by hardware limitations, since it required a number of 2π pulses using high power to achieve the polarisation transfer. The probe used showed a limitation in the B_1 field, with a maximum close to 60 kHz on the ^{1}H channel. To achieve the COMPOZER-CP, a B_1 field of at least 80 kHz was necessary in order to excite the whole ^{1}H spectrum.

Another sequence based on the COMPOZER-CP but using only 180^o with alternating 90^o phase shifts was implemented and tested with better results. In this case, the effect could be described with large thermal mixing in the doubly rotating frame, which was characteristic for samples doped with a high concentration of TEMPO radical. The B_1 field was 37 kHz on both channels.

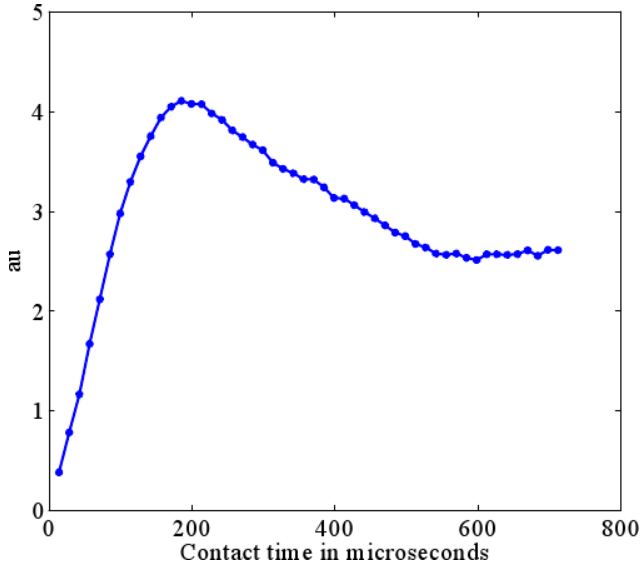

Figure 5.13: *Adapted COMPOZER-CP with π pulses. Optimisation was performed by increasing the number of π pulses. The sample used was 90 mM TEMPO with 1.54 M [^{13}C-1] Na acetate in 1:1 deuterated glycerol-D_2O.*

Adiabatic $\hat{I}_z \Longrightarrow \hat{S}_z$ CP sequence: DOIN-CP

Cross Polarisation has been achieved with adiabatic demagnetisation and remagnetisation in the rotating frame [4] and described thermodynamically with a model where thermal reservoirs communicate in the rotating frame [4], [8]. The use of adiabatic pulses well known in polarisation transfer [1] and the use of adiabatic inversion pulses for polarisation transfer has been suggested in a number of publications [1], [7], [13]. In this section an enhanced performance of adiabatic inversion pulses for polarisation transfer is presented.

WURST inversion pulses

This adiabatic inversion pulse was suggested by Kupce *et al* [6]. Fast adiabatic passage was posited as an excellent way to invert the magnetisation. The suggested pulse provides for inversion Wideband excitation, Uniform Rate and Smooth Truncation (WURST). It achieves a large inversion bandwidth which implies robustness against B_0 inhomogeneities for a given peak power. The WURST pulse involves a smooth increase and decrease in RF intensity ac-

cording to $\omega_1 = |\omega_1(max) * (1 - sin(\zeta t))|$, where $-\frac{\pi}{2} < \zeta t < \frac{\pi}{2}$. The phase is selected as $\phi(\mathrm{t}) = \phi_0 + \frac{1}{2}\mathrm{k}t^2$ where k is a constant [6].

The sequence that achieves polarisation transfer is formed by two WURST inversion pulses on each channel: two for ^{13}C and two for protons as shown in figure 5.14. Because it depends on two inversion pulses for each channel this sequence is called DOuble INversion Cross Polarisation (DOIN-CP).

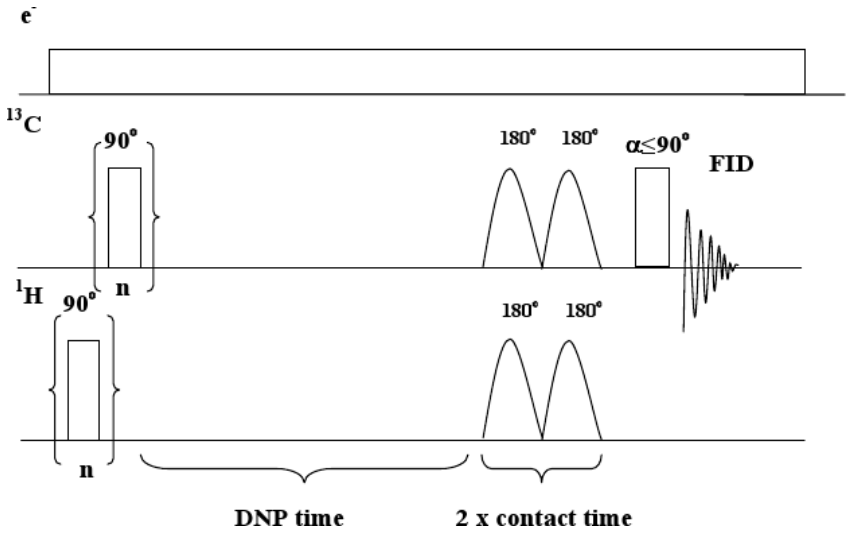

Figure 5.14: *DOIN-CP sequence. The ^{13}C signal is first saturated along with the proton magnetisation. After a DNP build-up time, the DOIN-CP transfers the ^{1}H polarisation to the ^{13}C nuclei. After the adiabatic polarisation transfer, a further pulse is used to measure the amount of magnetisation transferred to the ^{13}C. The pulse was applied 0.1 s after the last adiabatic pulse. The final ^{13}C magnetisation is aligned with the main magnetic field.*

In this case the B_1 fields were matched to 20 kHz for both channels with an error of 2 kHz (figure 5.15). The pulse duration was optimised as shown in figure 5.16. The basic WURST pulse was selected with a 40 kHz inversion bandwidth and with a duration of 1 ms. The same basic WURST pulse was used on both channels. These inversion pulses were applied to samples with deuterated solvent so the bandwidth of the protons was narrower ($\leq$ 20 kHz) than the inversion bandwidth of the WURST pulse.

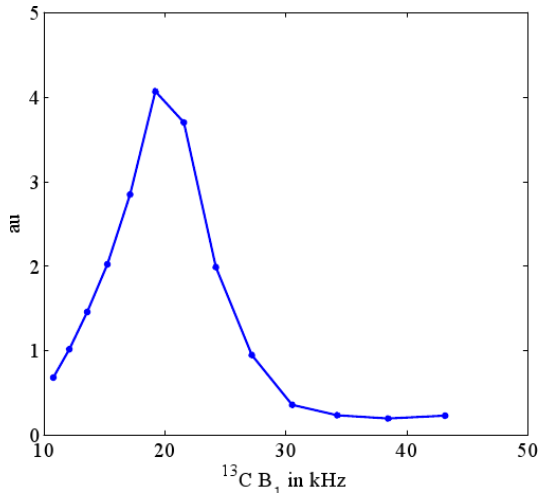

Figure 5.15: *Dependence of DOIN-CP efficacy on Hartmann-Hahn matching condition after 10 s of DNP microwave irradiation. The* ^{13}C B_1 *field strength was varied from 10 to 45 kHz. The sample used for this experiment was 90 mM TEMPO with [*^{13}C*-1] labelled Na acetate in 1:1 deuterated glycerol-*D_2O*. In these experiment the* B_1 *fields were matched to 20 kHz.*

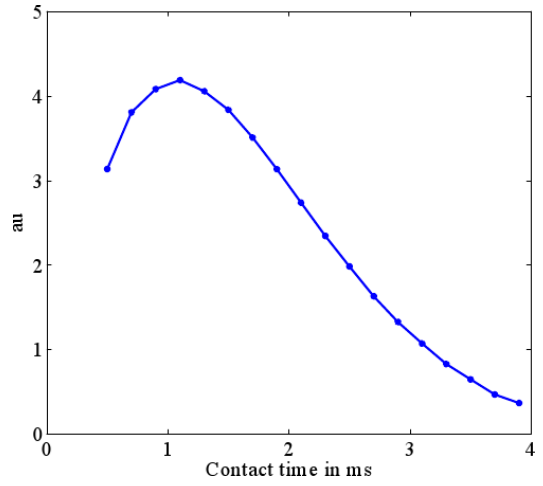

Figure 5.16: *DOIN-CP contact time optimisation. For a maximum of polarisation transfer after 10 s of DNP microwave irradiation, the contact time is close to 1 ms. The pulse was designed to be 1 ms with an inversion linewidth of 40 kHz.*

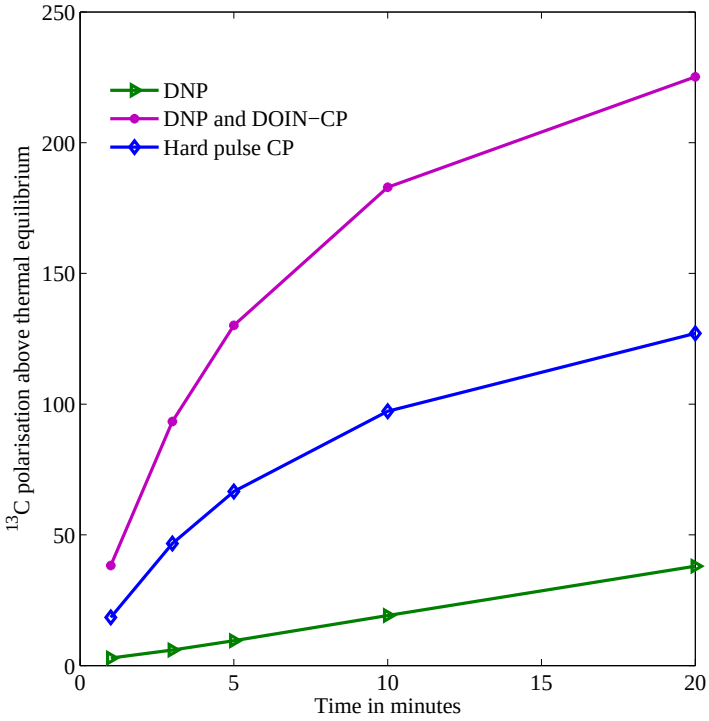

Figure 5.17: *Comparison between DOIN-CP, an adapted sequence from COMPOZER-CP with 180º (hard pulse CP) and DNP curves for ^{13}C. The final magnetisation is aligned with the B_0 magnetic field in each of the three curves. The sample temperature was 1.74 K.*

Discussion of $\hat{I}_z \Longrightarrow \hat{S}_z$ sequences

Two new techniques for polarisation transfer were tested at the lowest temperature that the polariser allowed at that time (1.74 K): DOIN-CP, and a hard inversion pulse CP. The COMPOZER-CP sequence was tested but with inferior results, as a consequence of RF B_1 limitations. The DOIN-CP and the hard pulse CP sequence based on the COMPOZER-CP sequence of Fukuchi are compared in figure 5.17, with the DNP enhancement presented by the build-up curves. A tilt angle of 3 ± 1^o was used to measure the ^{13}C magnetisation. With lower power, the DOIN-CP yielded better transfer efficacy and thus larger final polarisation than the hard pulse CP sequence. The COMPOZER-CP sequence may provide superior performance if stronger B_1 fields can be

employed.

Thermal mixing in the doubly rotating frame.

Following the concept of spin temperature and the thermal contact between two bodies, the colder the ^{13}C Zeeman reservoir is before the contact with the proton Zeeman reservoir via the dipolar reservoir, the closer it will be to the maximum achievable polarisation. This may be obtained by repeating the DOIN-CP sequence without saturating the magnetisation as shown in figure 5.18 in an improved DOIN-CP. An experiment was done with TEMPO with [^{13}C-1] Na acetate and several build-up curves were compared for ^{13}C in figure 5.19. DNP build-up data for ^{1}H and ^{13}C were measured and yielded characteristic build-up times of 2.8 and 15.0 minutes respectively. In comparison the improved DOIN-CP build-up data was fitted to a monoexponential curve with a time constant of 4 minutes. These results were taken with the double resonance probe suitable for dissolution with a saddle coil as a sample coil, and again showed how the final ^{13}C polarisation could be enhanced in a shorter time. The DOIN-CP build-up data could not be fitted properly with a monoexponential curve, but only to estimate the ^{13}C build-up in this experiment. The consequence of the dependence of DOIN-CP on polarisation levels of both spin species was evidenced by applying the improved DOIN-CP sequence and comparing the results with normal DOIN-CP and DNP in figure 5.19.
Once the final ^{13}C magnetisation has been obtained it is necessary to maintain the polarisation levels for sufficient time as to perform a dissolution experiment.

Two possible curves for the ^{13}C polarisation levels following the final pulse in the DOIN-CP sequence are shown in figure 5.20. If the sample is kept under EPR irradiation then the curve will tend to the DNP equilibrium state, at a rate very similar to the ^{1}H build-up, although not necessarily the same. On the other hand, if the microwaves are switched off, the ^{13}C polarisation will tend to the Boltzmann equilibrium at the T_1 rate.

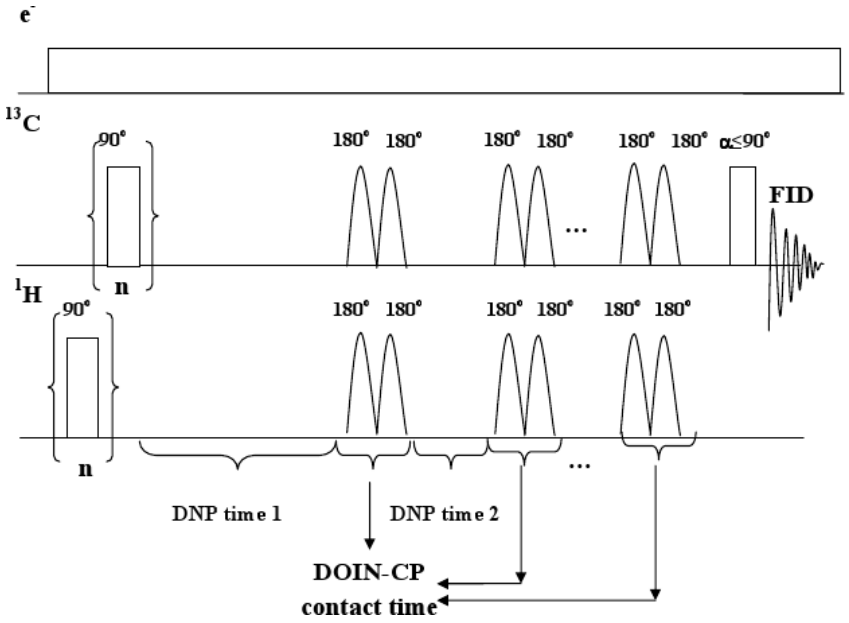

Figure 5.18: *Repeated DOIN-CP sequence. The polarisation transfer is more effective when there is already a significant amount of* ^{13}C *polarisation before the thermal contact.*

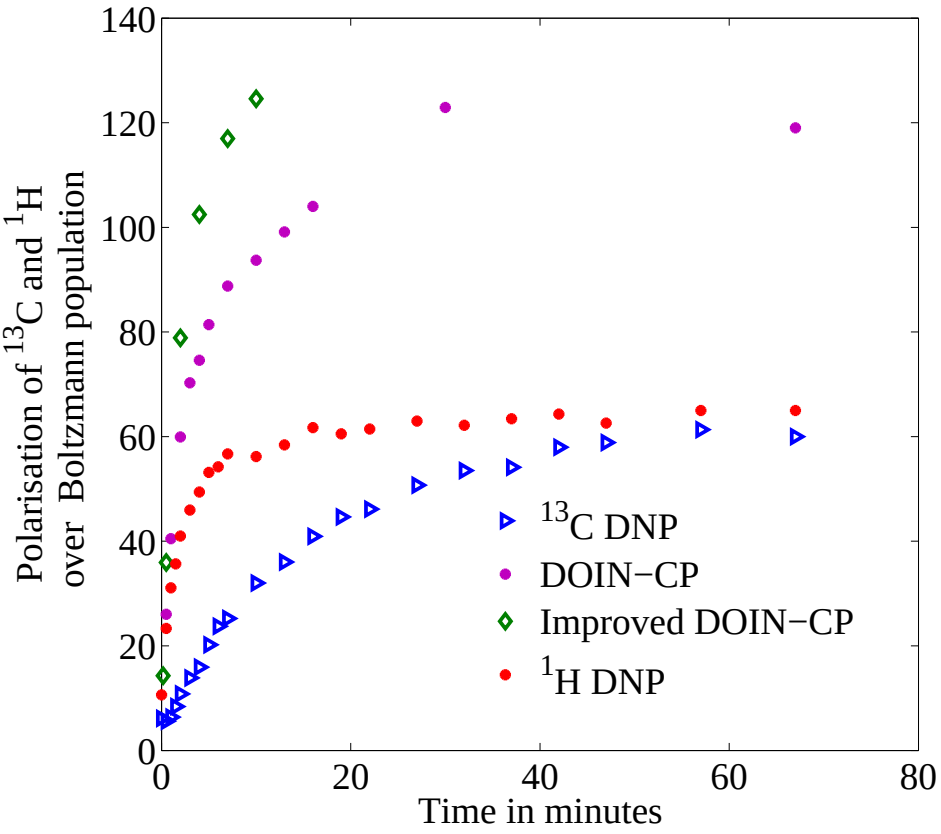

Figure 5.19: *^{13}C and ^{1}H DNP and DOIN-CP build-up data. In this figure, data are compared for: DNP build-up data, and DNP + DOIN-CP and an improved version of the latter based on repetition of the DOIN-CP basic pulses (presented in figure 5.18). The sample is 96 mM TEMPO with 1 M [^{13}C-1] Na acetate in 1:1 D_2O-deuterated glycerol at 1.58 K. The base WURST pulse was the same for ^{1}H and ^{13}C in both sequences. It was designed with 40 kHz excitation bandwidth and 1500 µs duration, although in the optimisation it was found that 1200 µs was superior. The B_1 fields were matched to 20 kHz.*

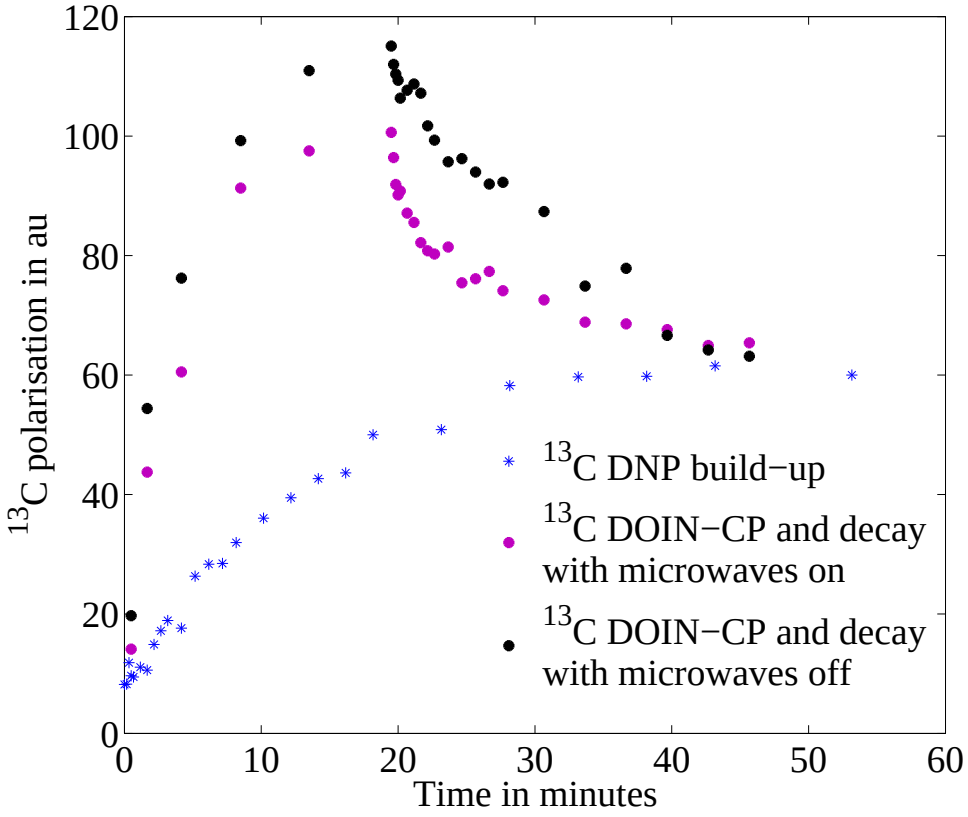

Figure 5.20: *Build-up curves. In this figure a DNP curve, a DNP+DOIN-CP and an improved version of the latter are compared for a sample of 96 mM TEMPO with 1 M [^{13}C-1] Na acetate in 1:1 D_2O-deuterated glycerol at 1.57 K. The discrepancies between the build-up data correspond to slight changes in temperature during the experiment (<0.1 K).*

The final ^{13}C polarisation after repeating the basic adiabatic pulses of DOIN-CP was much greater than by applying only one single DOIN-CP pulse, as shown in figure 5.19.

5.6 Conclusions

Several polarisation transfer sequences for CP experiments were tested and evaluated at temperatures around 1.5 K. The traditional CP sequence shows superior performance in comparison to NZCP sequences, although the latter represent a more convenient option for situations in which the power that could be tolerated by the probe was limited. Each sequence was used in combination with DNP to improve ^{13}C SNR at temperatures of 1.5 K. Furthermore the experimental time was reduced since build-up times for proton spins are shorter than for ^{13}C spins. For dissolution experiments where a large ^{13}C polarisation was required before the sample was dissolved the sequences provided no advantage over DNP alone, since a considerable percentage (typically 30 % at least) of the ^{13}C polarisation was lost when it was rotated onto the z-axis, and much further until it was under that magnetisation obtained with just DNP. The COMPOZER-CP [3] sequence offered, in our case, poor polarisation transfer efficiency due to its high power requirements. A modification of the COMPOZER-CP sequence using 180^o pulses instead of 360^o pulses provided good results for obtaining $\hat{S}_z$ as the final state for ^{13}C. Better results were obtained with the DOuble INversion CP sequence with much less power required. At the same time, it was shown that the efficiency of the DOIN-CP improved in samples with a fast ^{1}H build-up (of the order of 1 to 5 minutes) by repeating the basic sequence but with an intermediate time to allow the ^{1}H polarisation to build up.

With these experiments it was shown that the efficiency of the CP process improved the larger both magnetisations were before the contact.

As a final conclusion of this chapter, it was demonstrated experimentally

that efficient cross polarisation sequences can be applied at temperatures as low as 1.5 K. The new sequences applied (the modified COMPOZER-CP, DOIN-CP and the improved DOIN-CP) proved to be effective at transfering $\hat{I}_z$ to $\hat{S}_z$ magnetisation.

Bibliography

[1] S. Capuani, F. De Luca, L. Marinelli, and B. Maraviglia. Coherence-transfer processes by adiabatic pulses. *J. Mag. Res.*, 121:1–7, 1996.

[2] A. E. Dementyev, D. G. Cory, and C. Ramanathan. Rapid diffusion of dipolar order enhances dynamic nuclear polarization. *Amer. Phys. Soc.*, 77:024413, 2008.

[3] M. Fukuchi, A. Ramamoorthy, and K. Takegoshi. Efficient cross polarization using a composite 0^o pulse for NMR studies on static solids. *J. Mag. Res.*, 196:105–109, 2009.

[4] S. R. Hartmann and E. L. Hahn. Nuclear double resonance in the rotating frame. *Phys. Rev.*, 128:5, 1962.

[5] R. Kimmich. *NMR Tomography Diffusometry Relaxometry.* Springer-Verlag Berlin Heidelberg, 1997.

[6] E. Kupce and R. Freeman. Adiabatic pulses for wideband inversion and broadband decoupling. *J. Mag. Res.*, 115:273–276, 1995.

[7] N. D. Kurur and G. Bodenhausen. Adiabatic coherence transfer in magnetic resonance of homonuclear scalar-coupled systems. *J. Mag. Res.*, 114:163–173, 1995.

[8] J. S. Lee and A.K. Khitrin. Thermodynamics of adiabatic cross polarization. *J. Chem. Phys.*, 128:114504, 2008.

[9] J. R. Lewandowski, G. D. Paepe, and R. G. Griffin. Proton assisted insensitive nuclei cross polarisation. *J. Amer. Chem. Soc.*, 129:728–729, 2007.

[10] D. Marks and S. Vega. A theory for cross-polarization NMR of nonspinning and spinning samples. *J. Mag. Res.*, 118:157–172, 1996.

[11] David Rovnyak. Tutorial on Analytic Theory for Cross-Polarization in Solid State NMR. *Conc. Mag. Res.*, 32A(4):254–276, 2008.

[12] H. M. Vieth and C. S. Yannoni. Cross polarization in solid state NMR spectroscopy. Efficient polarization transfer via the non-Zeeman spin reservoir. *Chem. Phys.Lett.*, 205:153–156, 1993.

[13] C. Zwahlen, S. J. F. Vincent, and L. E. Kay. Analytical Description of the Effect of Adiabatic Pulses on IS, I_2S and I_3S Spin Systems. *J. Mag. Res.*, 130:169–175, 1998.

Chapter 6

Dissolution experiments

6.1 Introduction to dissolution experiments

A large number of experiments has been undertaken since Anderkjaer Larsen [2] demonstrated the Zeeman order is preserved in a dissolution experiment. In this experiment the nuclear spins are hyperpolarised at low temperatures with dynamic nuclear polarisation (DNP). After the dissolution, the sample is moved from a Stand Alone Polariser (SAP) in a few seconds to another magnet (9.4 T) gaining a signal to noise ratio enhancement greater than 10000 times the thermal equilibrium at room temperature. This technique has been applied for 2-D spectroscopy [6], [7].

In the present chapter some practical details about this dissolution experiment are presented and discussed. In the end of this chapter it is demonstrated that it is possible to use nuclear polarisation transfer from proton to ^{13}C spins in solid state in order to improve the efficiency and experimental time in dissolution experiments.

6.2 Hyperpolarisation

In the previous chapters two main strategies to enhance the nuclear magnetisations were used at 1.5 K. With brute force polarisation the nuclear order

was increased with a low temperature. With DNP it is possible to enhance the nuclear polarisation by typically two orders of magnitude at temperatures as low as 1.5 K by applying microwave irradiation to a sample doped with free radicals. Each one of these strategies presents advantages and disadvantages. DNP seems to be the fastest option for in vitro and in vivo applications at the moment of writing. However, for in vivo experiments most of free radical used for the DNP hyperpolarisation must be removed from the sample before injecting it into the living organism because of the potential toxicity of the free radical in large concentrations in the living organism [4] and [3]. A solution for this issue is provided by passing the sample (once dissolved) through a filter for free radicals, but the process adds some more complications to the already complex dissolution experiment.

The other approach by brute force polarisation consists of lowering the lattice temperature to millikelvin in a moderate or high magnetic field so the nuclear polarisation once in thermal equilibrium becomes comparable to the polarisation achieved with DNP before dissolution. This method does not require toxic free radicals or any microwave irradiation. The problem with this technique is two fold. On one side the T_1 becomes so long that it appears impractical unless another strategy is taken by doping the sample with non toxic paramagnetic materials like some lanthanides as Dy^{3+} or Ho^{3+}. The technological problem of achieving a very low temperature is no longer a major issue since the technology available offers a range of fridges capable of achieving a few millikelvin above absolute zero [1]. The sample cooling down time can be compensated by the use of many samples simultaneously. It is not necessary to filter the lanthanide chelate since for reasonable concentrations it is not toxic in analogy to the case of gadolinium Ga-DTPA.

6.3 The dissolution experiment

In the dissolution process, the sample was raised a few cm above the helium bath from the bottom of the SAP, to prevent important pressure gradients inside the polariser when the dissolution dock established contact with the sample cup. The OI SAP magnetic field was 3.35 T. For each experiment, the polariser was pressurised to room pressure (it took 8-30 s), which increased the liquid helium temperature from 1.5 K to 4.2 K. According to the data available from OI, at this height the magnetic field was still greater than 3 T. It had to be in this position the required time to introduce the warm dissolution dock straight to the sample (3-5 seconds). As shown in figure 6.1, the ^{1}H and ^{13}C magnetisations relaxed to thermal equilibrium for the temperature of 4.2 K, once the system was pressurised. However, this relaxation process was not immediate, since it took some time for the sample to first reach this higher temperature and second for the nuclear magnetisations to relax at 4.2 K (see figure 6.1). For the dissolution, a typical amount of 3.5 ml of solvent was overheated to 170^{o} C (6 bar) in a pressure cooker at top of the dissolution rod, in the same fashion as [2]. In all experiments D_2O was used as a solvent. Immediately after the dissolution the sample was passed to another magnet through 4-5 m long PTFE tubes in a few seconds, although a settling time of 0.5 s had to be added to avoid the presence of bubbles. A typical time of 3 to 4 s was used from the moment of dissolution until the start of signal acquisition in the 9.4 T Brucker magnet. For DNP experiments, a typical spin temperature θ was 20 mK so the expected enhancement was of the order of thousands of times higher than the Boltzmann population at room temperature (roughly $\frac{3.35T}{9.4T}\frac{300K}{\theta}$), meanwhile for brute force polarisation it was only about 2 orders of magnitude higher for this population, since the minimum spin temperature corresponded to the lattice temperature, typically 1.5 K. During the time the sample was being transferred, it was expected that the magnetisation decayed with the T_1 of the magnetic field where the sample was being exposed.

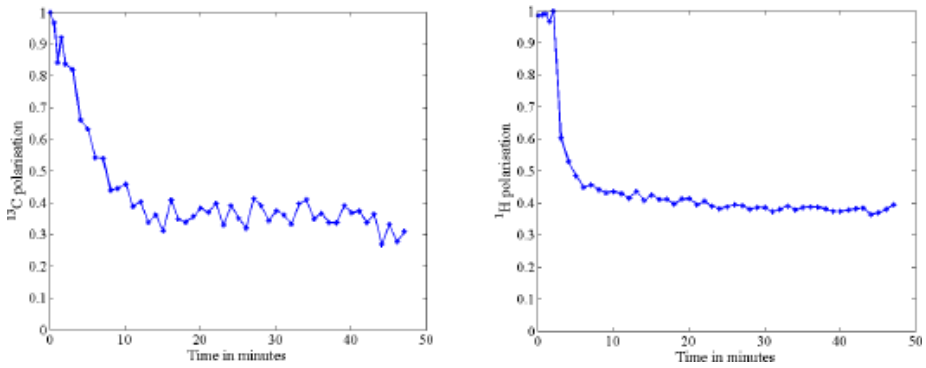

Figure 6.1: *^{13}C (left) and proton (right) magnetisation decay from the Boltzmann population at 1.51 K to the new population at 4.27 K for a sample of 8.6 mM Ho^{3+}-DTPA with 1.7 [^{13}C-1] labelled Na acetate in 1:1 glycerol-water. The sample was pressurised between the second and third minute. The pressurisation took 15-20 s, with gas helium at room temperature. The dissolution would take place several seconds at most afterwards, and in this graphs the proton polarisation stayed steady for about two more minutes before it decayed. The T_1 of protons for this sample was 97 s and 1.2 s at 1.51 K and 4.2 K respectively. The ^{13}C polarisation relaxed slower since the T_1 were longer.*

Dissolution with the new dissolution dock

The homemade dissolution dock replaced the former one by OI but kept the same pressure heater. It was designed to fit into the double resonance probe suitable for dissolution experiments (chapter 2). The PTFE tubes used to transport the solvent in and out of the SAP were smaller than for the OI dissolution dock used in some of the experiments, which translated into a longer dissolution time. For the OI dissolution dock, a minimum time of 3-4 seconds was necessary to send the sample to the 9.4 T magnet. For the homemade one the required time was 8 s.

The sample cup was made in PEEK (figure 6.2, 3). It was loaded from underneath the probe before introducing it into the SAP, leaving the 15 μl sample in the centre of the saddle coil. It presented a step at the bottom that stopped the sample cup entering any further into the coil former. The sample cup was clamped afterwards by a PTFE nut on the coil former (figure 6.2, 6).

The dissolution dock was basically a non magnetic steel tube of 6 mm OD

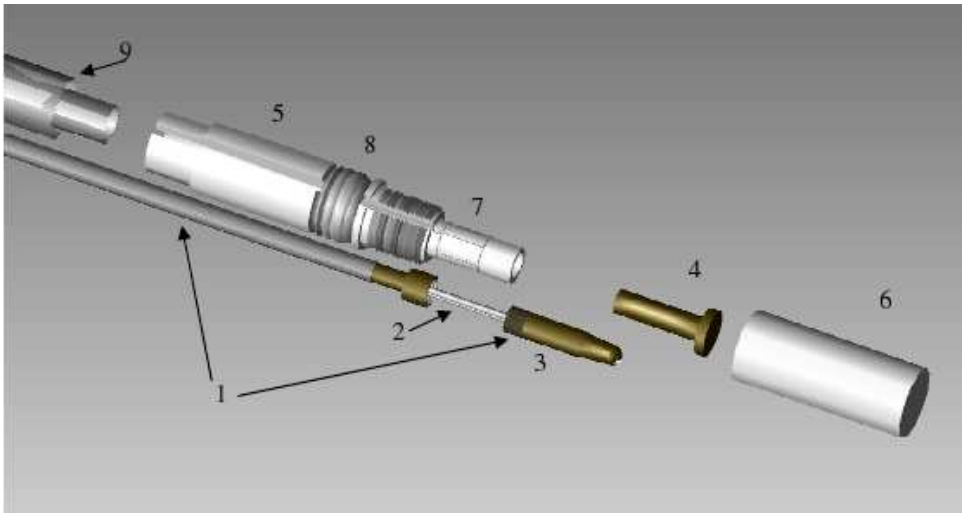

Figure 6.2: *Plot of the dissolution dock and the double resonance probe for dissolution experiments in parts. The dissolution dock (1) is formed by a stainless steel tube with two PTFE tubes inside (2) and finished in a PEEK tip (3) that enters into the sample cup (4). This sample cup is placed in position inside the PTFE coil former (5) and clamped by a PTFE nut (6), so the sample is in the centre of the saddle coil (7). The circuit for this coil is attached to this PTFE former with PTFE tape in (8). The coil former enters into the home-made cable (9) of the double resonance probe, which presents a tube as inner conductor that leads the dissolution dock to the sample cup.*

and 1 mm wall thickness that allowed two PTFE tubes of 1.6 mm OD and 1.0 mm ID, one to bring the solvent outside into the SAP, the other to send the dissolved sample outside the SAP. One of the tubes led to the solvent heater and the other to the 9.4 T magnet. The two tubes finished in a thread that fixed in position both tubes inside a PEEK tip (figure 6.2, 3). The outer shape of this tip coupled with the sample cup in the dissolution process.

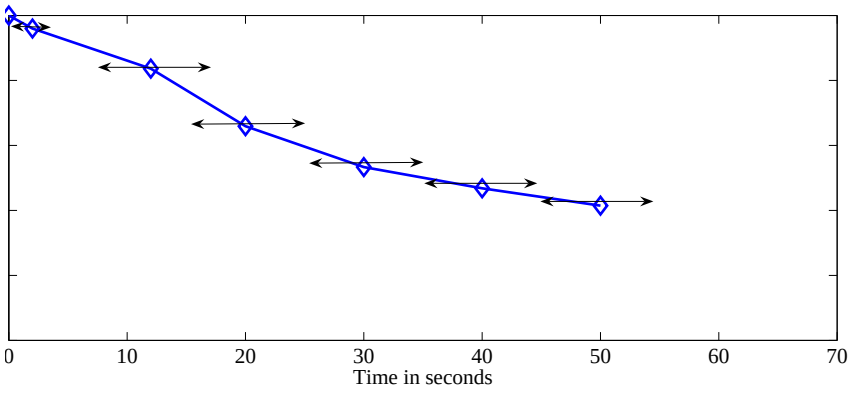

Figure 6.3: *^{13}C measured magnetisation after exposure of the sample outside the magnet. The sample was taken from the magnet and exposed to a lower magnetic field (80 mT) for the time shown in the x-axis minus 10 s.*

6.4 Estimation of ^{13}C polarisation losses between the 3.35 T SAP and the 9.4 T Bruker magnet

Typical relaxation times for ^{13}C were measured in about a minute in samples of ^{13}C acetate dissolved in D_2O at 9.4 T at room temperature. A good estimation of the ^{13}C polarisation losses in the trip from the 3.35 T magnet and the 9.4 T magnet was obtained by leaving a sample with abundant ^{13}C signal in the Bruker magnet. After thermal equilibrium was obtained, the sample was extracted from the magnet and exposed outside to a lower magnetic field (80 mT $\pm$ 20 mT) (1 m away from the Bruker magnet and between this and the SAP) for some time before returning it back to the 9.4 T scanner. The SAP was 2 meters away from the Bruker magnet. As shown in figure 6.3, the first point corresponds to the ^{13}C polarisation in equilibrium at 9.4 T. The second point in the same graph corresponds to the polarisation once it has spent 1 s at the top of the magnet plus traveling time. The rest of the points are measured after the sample has been exposed to 80 mT outside the magnet for some seconds plus traveling time (10 s).

During the time the sample was outside the magnet, the ^{13}C magnetisation

relaxed at the much lower magnetic field. This experiment yielded valuable information about the possible magnetisation losses in the dissolved sample in the trip from the OI SAP to the 9.4 T Bruker magnet. The T_1 of the sample in low field played an important role since a very short relaxation time could invalidate the whole experiment. This was not the case for when the sample was dissolved in the SAP and transferred to the 9.4 T magnet.

However this was precisely the case for ^{13}C acetate in powder. The T_1 was estimated to be 5 minutes at room temperature and at 9.4 T. However, for a brief time of 1 s 20 cm away from the magnet centre (within the magnet), most of the polarisation was lost. Large dipolar interactions were responsible for this quick relaxation, which automatically invalidated the possibility of hyperpolarising the powder sample at low temperature and transporting it to another magnet without dissolving it first.

6.5 SNR after dissolving sample

Dissolution experiments [2] experiments aim to achieve a high SNR in liquid state. It was calculated with the maximum value of the spectrum peak divided by the standard deviation of baseline noise in a region of 200 Hz [2].

One strategy to improve in SNR is obtained by lowering the dilution factor using a more concentrated sample in liquid helium. A rough estimation for a typical sample of 7 μl 2 M acetate dissolved with 3.5 ml of D_2O resulted in a final concentration of 4 mM acetate.

Lyophilisation of the sample.

In this project [^{13}C-1] Na acetate was used for dissolution experiments in a prepared sample of 1:1 glycerol-water doped with paramagnetic material centres. In brute force polarisation the ^{13}C polarisation relaxes towards thermal equilibrium. Spin diffusion plays an important role in nuclear relaxation when the paramagnetic centre is not close to the nucleus to be polarised. When

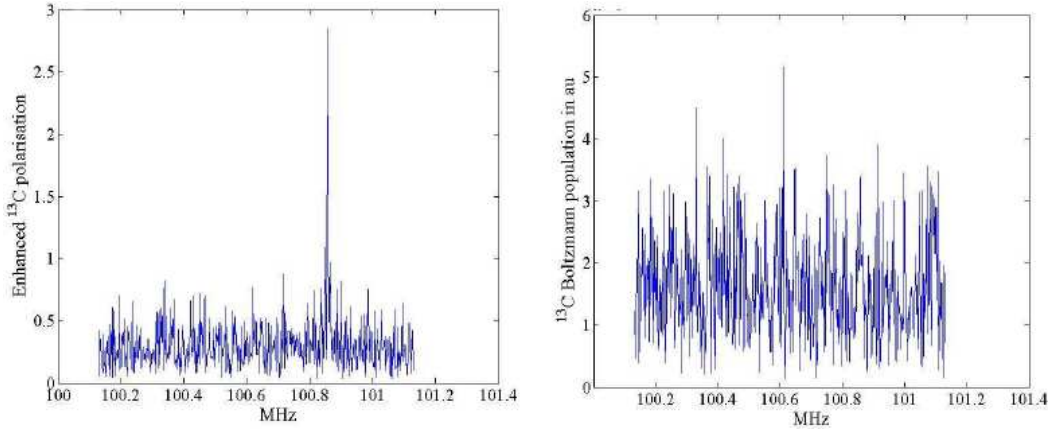

Figure 6.4: *Spectra for enhanced ^{13}C in 1.8 M [^{13}C-1] labelled Na acetate Ho^{3+} DTPA 24 mM after dissolution (left) and once in thermal equilibrium (right) at room temperature and 9.4 T. A 2 Hz filter was used. The sample had achieved 90% of the equilibrium magnetisation at 1.55 K before dissolution with 3.5 ml of D_2O. For the Boltzmann population once at room temperature 30 averages taken with the same flip angle corresponding to 90º. The gain used was 10240.*

it is close enough to the unpaired electron, nuclear relaxation is achieved by direct processes. With spin diffusion the polarisation is carried away from the paramagnetic centre.

Then one strategy to increase the concentration of nuclear spins and to give more importance to relaxation through direct processes is by lyophilisation of the sample, which leaves the paramagnetic centre very close to the targeted nuclear spin since there is no solvent left. In this chapter nuclear relaxation with paramagnetic impurities for lyophilised samples proved effective.

The results of dissolution experiments for two kind of samples are compared. One of them corresponded to a sample of close to 2 M [^{13}C-1] labelled Na acetate dissolved in 1:1 water-glycerol and doped with a few mM Ho^{3+}-DTPA, 7 μl volume. The other one to lyophilised 2M [^{13}C-1] labelled Na acetate with some concentration of mM Ho^{3+}-DTPA prepared before lyophilisation. The amount of sample for the dissolution experiment was 20 mg weight. Both samples were dissolved with D_2O before being transferred to the 9.4 T magnet.

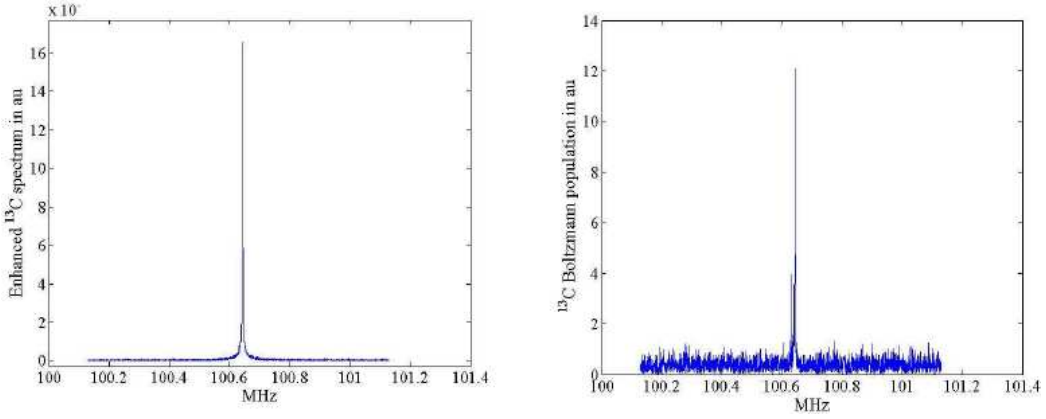

Figure 6.5: *Spectra for enhanced ^{13}C in [^{13}C-1] Na acetate in powder with Ho^{3+}-DTPA 6 mM after dissolution (left) and once in thermal equilibrium (right). A 2 Hz filter was used. The sample reached over 90 % of thermal equilibrium at 1.58 K before dissolution with 3.5 ml of D_2O. In this case averaging was not necessary since a single acquisition yielded enough signal.*

Three dissolution experiments were performed with 3.5 ml of D_2O on samples of the first kind that were kept at temperatures close to 1.5 K and with ^{13}C polarisations in thermal equilibrium. The samples had a concentration of approximately 2 M of ^{13}C Na acetate and a concentration of 3.8, 8.6 and 24 mM of Ho^{3+}-DTPA dissolved in 1:1 glycerol-water. The enhancement for the three of them was inside the margin of 11 ± 4. An example of one of these dissolutions is given in figure 6.4.

Other three dissolutions took place with the same conditions but with the lyophilised samples of [^{13}C-1] labelled Na acetate in powder. The concentrations of Ho^{3+}-DTPA were 2, 6 and 20 mM before lyophilisation. The enhancement for the three of them was inside the margin of 13 ± 5, but the SNR was significantly higher in this case (over 100 in the dissolution experiment), because of the larger amount of ^{13}C in the dissolved sample, as shown in figure 6.5.

6.6 Measurement of T_1 at room temperature

For reference purposes, the T_1 for three samples of dissolved [^{13}C-1] labelled acetate after a dissolution experiment, once in thermal equilibrium at room temperature were measured with saturation recovery experiments. The measured samples were those prepared from lyophilisation of 2 M [^{13}C-1] with 2, 6 and 20 mM Ho^{3+}-DTPA in 1:1 glycerol-water. After the dissolution with D_2O the final solution was 0.1 $\pm$ 0.2 M. With this concentration the SNR at 9.4 T was sufficient to measure the T_1 for ^{13}C at room temperature without averaging. These times were 67, 67 and 54 s for 2, 6 and 20 mM Ho^{3+} respectively, far longer than the time spent in moving the sample between the magnets.

6.7 DNP and DOIN-CP for dissolution experiments

An improvement in time efficiency and free radical cost may be obtained by using DOIN-CP before a dissolution experiment. A suitable probe for DNP and CP that allows dissolution, along with a new dissolution dock were described previously.

The sample selected for this experiment was 2.3 M [^{13}C-1] labelled Na acetate with 96 mM TEMPO in 1:1 D_2O-deuterated glycerol. The irradiation frequency was 93.95 GHz. The data for DNP and DOuble INversion cross polarisation(DOIN-CP) were obtained using the same flip angle (less than 3^o). The ^{13}C T_1 was measured in 68 minutes respectively. The ^{1}H and ^{13}C build-up times τ were 5.5 minutes and 49 minutes respectively, and was considered to reach the same spin temperature as the ^{13}C [5]. The DOIN-CP build-up time was measured in 10.6 minutes. The ^{13}C polarisation decay from minute 175 to the DNP asymptotic value of the DNP plateau in figure 6.6 resulted in a 7.1 minutes relaxation time, which gave a reasonable margin of time to dissolve the sample. The measured enhancement over Boltzmann population

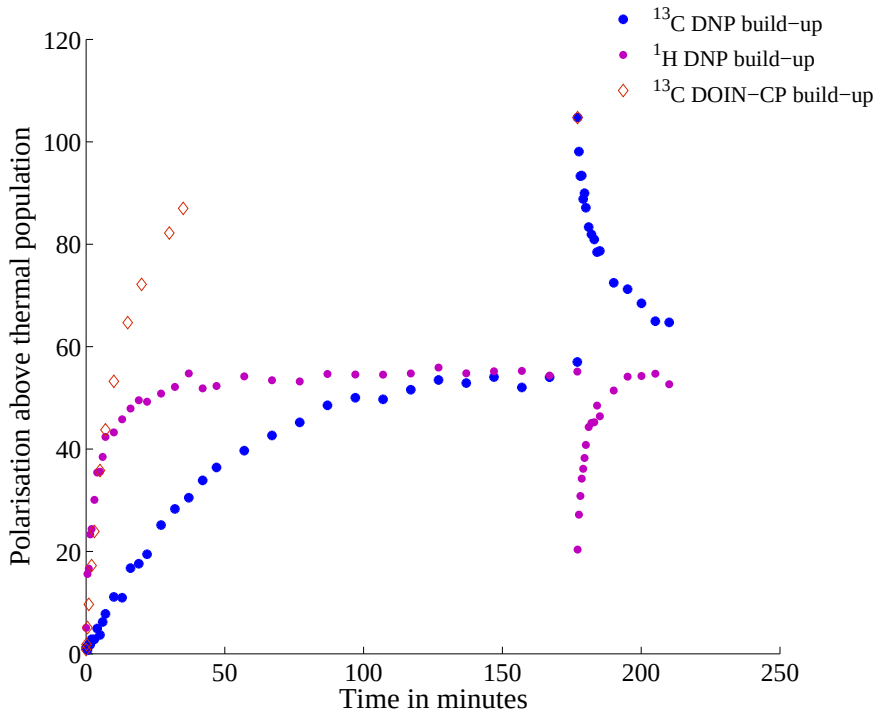

Figure 6.6: *DNP buid-up data for proton and ^{13}C spins, along with the build-up curve for DOIN-CP in this system in a sample of 2.3 M [^{13}C-1] labelled Na acetate with 96 mM TEMPO in 1:1 deuterated glycerol-D_2O at 1.58 K.*

for ^{13}C was 65, which for an experimental temperature of 1.58 K amounted to 5.1 % of total polarisation. Applying DOIN-CP an enhancement of 100 could be achieved which represented a percentage of 7.8 %. In this case the improved sequence for DOIN-CP did not show much better results with respect to the normal DOIN-CP. The DOIN-CP build-up data is included in figure 6.6. The basic pulse used for DOIN-CP was a WURST inversion pulse of 40 kHz excitation bandwidth and 1500 μs of duration, although in the optimisation only 1200 μs were used.

The improved DOIN-CP sequence showed barely the same efficiency as doing just DOIN-CP. The last sequence of improved DOIN-CP was applied after 17.5 minutes, achieving an enhancement of 80 above thermal population (6.2%) or 20 mK in spin temperature. After this last pulse, the cables for the probes in solid state and liquid state for ^{13}C had to be changed since

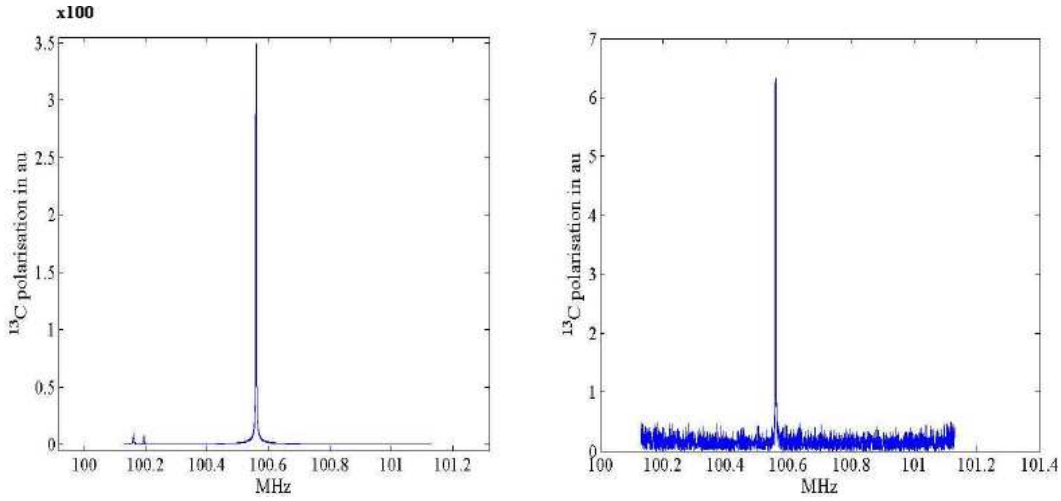

Figure 6.7: *Spectra for enhanced ^{13}C in [^{13}C-1] labelled Na acetate after dissolution (left) and once in thermal equilibrium (right) after 100 averages.*

they shared the same preamplifier. The solvent (3.5 ml of D_2O) in the boiler reached 170^o or a pressure of 6 bar, and the SAP was pressurised. The whole process took 2 minutes and 10 seconds from the last DOIN-CP pulse to the signal acquisition at 9.4 T. The time to pressurise the SAP and docking was 35 s approximately. Then, from this point until signal acquisition at room temperature with the 9.4 T magnet was 8.5 seconds. In liquid state the sample was collected in a 5 mm glass tube. The spectra were obtained using a 90^o pulse in a high resolution Bruker probe. The signal-to-noise (SNR) values were measured dividing the maximum of the absolute value of the spectrum by the standard deviation of the noise in a range of 200 Hz. A line broadening of 2 Hz was applied to both spectra. The measured enhancement was 5000 attending to the real value of the spectrum, but for the absolute value it was lower (3000). For the experimental temperature and the enhancement obtained before dissolution a maximum enhancement of 5400 was expected.

6.8 Conclusions

Several dissolution experiments were undertaken with polarisation temperatures as low as 1.5 K. At this temperature DNP methods rendered greater SNR

for NMR experiments after a dissolution experiment on a polarised sample by brute force polarisation, mainly due to limitations at minimum temperature achievable in the SAP. It was possible to lyophilise the samples so the paramagnetic dopant was closer to the ^{13}C target and a larger concentration of sample could be prepared for after dissolution, with an improvement in SNR. This was tested with brute force polarisation.

DOIN-CP sequences demonstrated an important improvement in the amount of polarisation in solid state and also in the time required to achieve it in the previous and present chapters. The data shown in this chapter demonstrates the efficiency of DOIN-CP with DNP for dissolution experiments.

6.9 Discussion

Especially good and also promising results were obtained by DOIN-CP based sequences and dissolution afterwards on samples doped with TEMPO radicals. This amount of polarisation has been improved by using a deuterated matrix instead of a fully protonated one [5]. The advantage of using TEMPO is the availability and price over trityl radicals, and on the relative quick build-up of proton polarisation using TEMPO over the slow ^{13}C polarisation using trityls. Some improvements may be possible by lowering the temperature of the system to 1.2 K or less in another system. Some improvements could be done on the hardware, for instance the dissolution dock. Using thicker PTFE tubes in the dissolution device the time required to transfer the sample to the 9.4 T magnet could be made shorter. A good point to be analysed carefuly is the irradiation conditions since they are responsible for reaching such a low enhancement with the dissolution probe (about 60 over Boltzmann population) when for the diagnostic probe with a solenoid as the sample coil this enhancement was about 80 or 90.

Bibliography

[1] http://www.dryogenic.com/.

[2] J. H. Ardenkjær-Larsen, B. Fridlund, A. Gram, G. Hansson, L. Hansson, M. H. Lerche, R. Servin, M. Thaning, and K. Golman. Increase in signal-to-noise ratio of $>$ 10000 times in liquid-state NMR. *Proc. Nat. Acad. Scienc.*, 100:10158–10163, 2003.

[3] A. Comment, J. Rentsch, F. Kurdzesau, S. Jannin, K. Uffmann, R. B. van Heeswijk, P. Hautle, J. A. Konter, B. van den Brandt, and J. J. Van der Klink. Producing over 100 ml of highly concentrated hyperpolarized solution by means of dissolution DNP. *J. Mag. Res.*, 194:152, 2008.

[4] A. Comment, B. van den Brandt, K. Uffmann, F. Kurdzesau, S. Jannin, J. A. Konter, P. Hautle, W. Th. Wenckebach, R. Gruetter, and J. J. van der Klink. Design and performance of a dnp prepolarizer coupled to a rodent mri scanner. *Conc. Mag. Res. B: Mag. Res. Eng.*, 2007.

[5] F. Kurdzesau, B van den Brandt, A Comment, P. Hautle, S. Jannin, J.J. van der Klink, and J. A. Konter. Dynamic nuclear polarization of small labelled molecules in frozen water-alcohol solutions. *J. Phys. D: Appl. Phys.*, 41:155506, 2008.

[6] M. Mishkovsky and L. Frydman. Principles and progress in ultrafast multidimensional nuclear magnetic resonance. *Ann. Rev. Phys. Chem.*, 60:429–448, 2009.

[7] H. Zeng, S. Bowen, and C. Hilty. Sequencitally acquired two-dimensional NMR spectra from hyperpolarized sample. *J. Mag. Res.*, 199:159–165, 2009.

Chapter 7

Final discussion

Dynamic nuclear polarisation (DNP) has been used to enhance nuclear polarisations above thermal levels at temperatures as low as 1.5 K. The use of Ox63 trityl radical with DNP yielded enhancements of about 100 for ^{13}C and ^{15}N in samples of [^{13}C-1] labelled Na acetate and ^{15}N urea. These enhancements translated into polarisations of 9.0% for ^{13}C and 5.6% for ^{15}N, although in the literature larger polarisations have been obtained in similar experiments (around 40%).

DNP using samples doped with TEMPO in 1:1 glycerol-water solvents, enhances the nuclear polarisation by a factor of around 30 over thermal equilibrium for ^{1}H and ^{13}C. By decreasing the number of protons in the solvent (i.e., by using D_2O and deuterated glycerol instead of 1:1 glycerol-water) the measured enhancement was higher (about 100). At temperatures around 1.5 K the final spin temperature for ^{1}H and ^{13}C became the same within the margin of error .

It has been demonstrated that cross polarisation techniques can be used to transfer the polarisation from ^{1}H to ^{13}C spins. In this work, it was possible to use published CP based sequences for polarisation transfer from ^{1}H to ^{13}C spins. Additionally new sequences were implemented (modified COMPOZER-CP, DOIN-CP and improved DOIN-CP). With these sequences, it was possible to achieve efficiently DNP and CP for dissolution experiments with TEMPO

doped samples.

The typical efficiency of the DOIN-CP was over 50% (in the limit where proton spins and ^{13}C spins achieve the same spin temperature at the DNP plateau). This made it possible to achieve twice the ^{13}C polarisation that would be reached by using only DNP and in a much faster time (of the order of the ^{1}H DNP build-up time). Less than 10 minutes was sufficient to achieve a ^{13}C polarisation of more than 14% in a sample of [^{13}C-1] acetate with 90 mM TEMPO in 1:1 glycerol-water at 1.74 K, using only DOIN-CP. Higher enhancements could have been achieved at lower temperatures, close to 1 K and using the improved DOIN-CP sequence.

To achieve the necessary probe performance, a large number of experiments on the bench and in the polariser were undertaken with different models of radiofrequency NMR probes. With space limitations, vacuum seal restrictions and high power tolerance, the choice of NMR probe was crucial for a successful CP experiments. The selected probe also affected the maximum polarisation achieved with DNP. The sample surroundings were different for each probe, and therefore, the irradiation conditions.

The experiment of dissolution after CP was challenging. In order to obtain a large and stable ^{13}C polarisation at low temperature after a high power pulse, a dissolution dock had to reach the sample with a strong impact and form a tight seal while the sample was being dissolved. The design of a sample cup that received the dissolution dock was the result of a number of compromises taken in this project, which translated in successful dissolution experiments.

Another alternative to obtain high polarisation levels without using DNP has been studied in this project with brute force polarisation. The hardware limitations restricted the operating temperature to not less than 1.3 K. At these temperatures, a sample of [^{13}C-1] labelled Na acetate in 1:1 glycerol-water exhibited a T_1 relaxation time of not less than 10 hours. By adding some concentration (around 20 mM) of lanthanide ions (either Ho^{3+}-DTPA or Dy^{3+}-DTPA, it was possible to reduce this relaxation time to less than 1

hour for the same. The polarisation achieved by acquiring thermal equilibrium could be used for dissolution experiments.